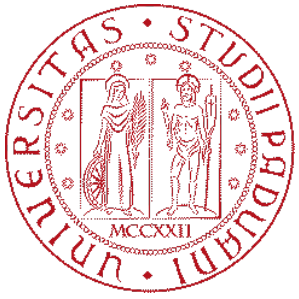

UNIVERSITÀ DEGLI STUDI DI PADOVA

Dipartimento di Fisica e Astronomia "Galileo Galilei"

Master Degree in Physics

Final Dissertation

Modelling of the propagation of a large negative hydrogen beam

Thesis supervisor

Dr. Gianluigi Serianni

Thesis co-supervisor

Dr. Emanuele Sartori

Dr. Valeria Candeloro

Candidate

Daniele Mussini

Academic Year 2021/2021

Abstract

Negative ion-based Neutral Beam Injectors (N-NBI) are one of the plasma heating methods envisaged for the ITER tokamak. The heating power is deposited by a highly energetic neutral beam, which is obtained by neutralising a precursor negative ion beam. The propagation of the latter is guaranteed by positive charges produced by the interaction between the beam and the background neutral gas: positive ions allow to compensate for the negative space charge of the beam ions to prevent the beam from diverging due to mutual charge repulsion. The aim of this thesis is the numerical investigation of the negative ion beam propagation, with a view to provide a deeper understanding of the involved physical processes. The results of these analyses will be exploited to reproduce synthetic measurements of beam diagnostics such as beam tomography and beam emission spectroscopy, in such a way as to benchmark the results against the experimental findings obtained during the 2021 SPIDER experimental campaign and also to better identify the phenomena underlying specific features of the experimental results. Ultimately, this work aims at providing additional knowledge about the beam propagation in view of the future experimental campaigns.

Contents

Chapter 1

Introduction

1.1 The energy problem

In the few past decades, as shown in figure 1.1, the demand for energy has significantly increased leading to the exploration of new energy sources.

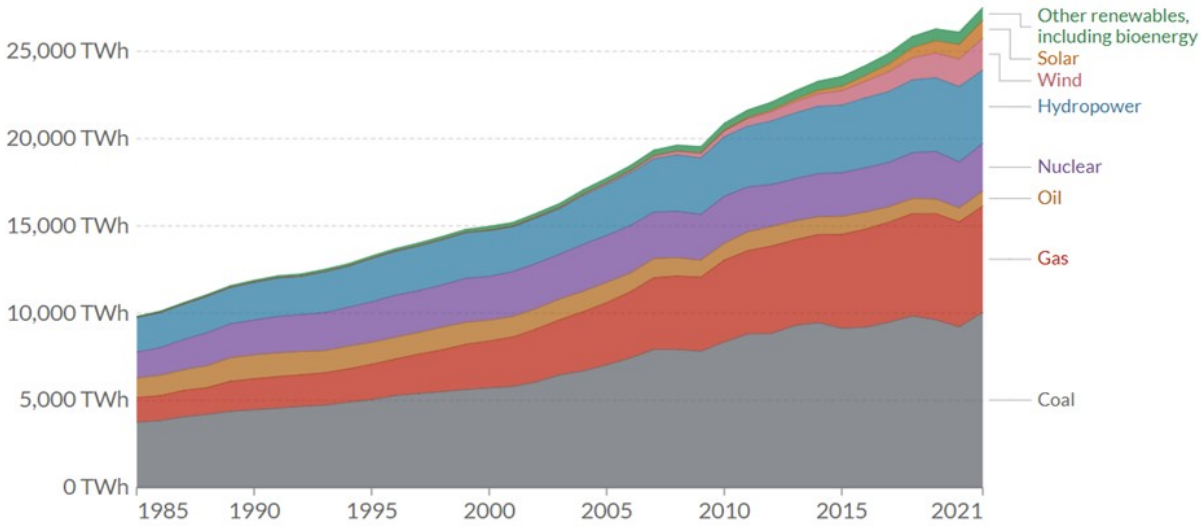

Figure 1.1: World's energy consumption [1]

Nowadays, power plants rely either on fossil fuels, nuclear fission, or renewable sources like wind, water or radiation from the Sun. However, each of them brings some drawbacks: energy produced from fossil fuels releases in the atmosphere a large amount of greenhouse gases responsible for the global warming, nuclear fission produces a large amount of long-lived nuclear radioactive waste that need to be safely stored and, finally, the efficiency of renewable sources are discontinuous depends on the year seasons and still they account for a very small fraction of the entire amount of needed energy. A possible alternative is provided by nuclear fusion that produces no greenhouse gases and only very small amounts of short-lived radioactive waste.

1.2 Energy production by nuclear fusion

The production of energy by nuclear fusion can be achieved by way of the following reactions:

$$^2D + {}^2D \longrightarrow {}^3He + n + 3.27\,MeV \tag{1.1}$$

$$^2D + {}^2D \longrightarrow {}^3T + {}^1H + 4.03\,MeV \tag{1.2}$$

$$^2D + {}^3T \longrightarrow {}^4He + n + 17.6\,MeV \tag{1.3}$$

$$^2D + {}^3He \longrightarrow {}^4He + {}^1H + 18.3\,MeV \tag{1.4}$$

The most efficient was found to be the one between deuterium and tritium, having the advantage of providing the highest energy gain at the lowest temperatures [2] [4]. Deuterium-Tritium (DT) reactions produce an α particle (^{4}He), a neutron and release 17.6 MeV energy; 4/5 of which (14.1 MeV) is carried away by the neutron, the remaining fifth (3.5 MeV) by the α particle.

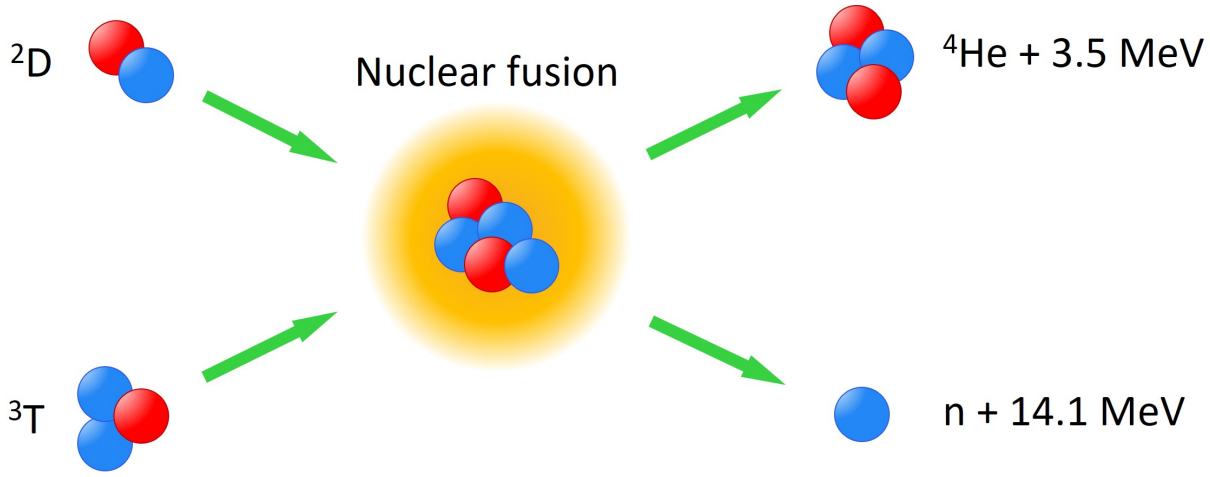

Figure 1.2: Deuterium-tritium fusion reaction

However, three conditions must be fulfilled to achieve fusion in a laboratory: very high temperatures (on the order of 150 million °C); sufficient plasma particle density (to increase the likelihood that collisions do occur); and sufficient confinement time (to hold the plasma within a defined volume) [2]. These tasks can be accomplished in devices called tokamaks. Tokamak is a Russian acronym that stands for toroidal chamber with magnetic coils. The heart of a tokamak is a doughnut-shaped vacuum chamber where, under the influence of extreme heat and pressure, gaseous deuterium becomes a plasma confined and controlled by means of strong magnetic fields. When temperatures of 150 million °C are reached, deuterium and tritium particles have enough kinetic energy to overcome the Coulomb repulsive barrier and fuse, releasing huge amounts of energy [2].

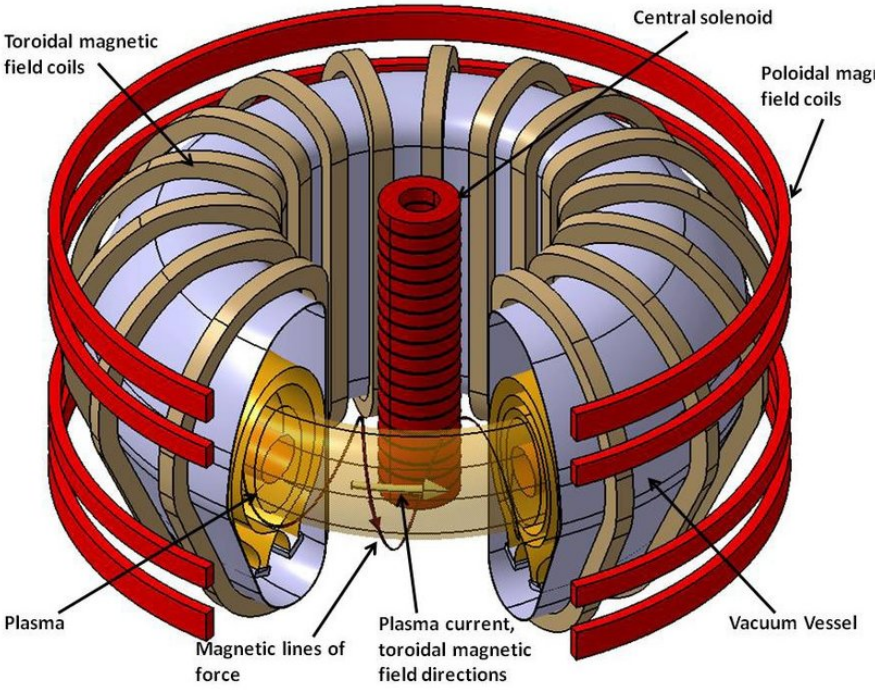

Figure 1.3: Tokamak

1.3 ITER and the way to power plants

ITER is an experiment located in Saint-Paul-lès-Durance, southern France, aimed at proving the feasibility of the nuclear fusion as a large-scale source of energy [2].

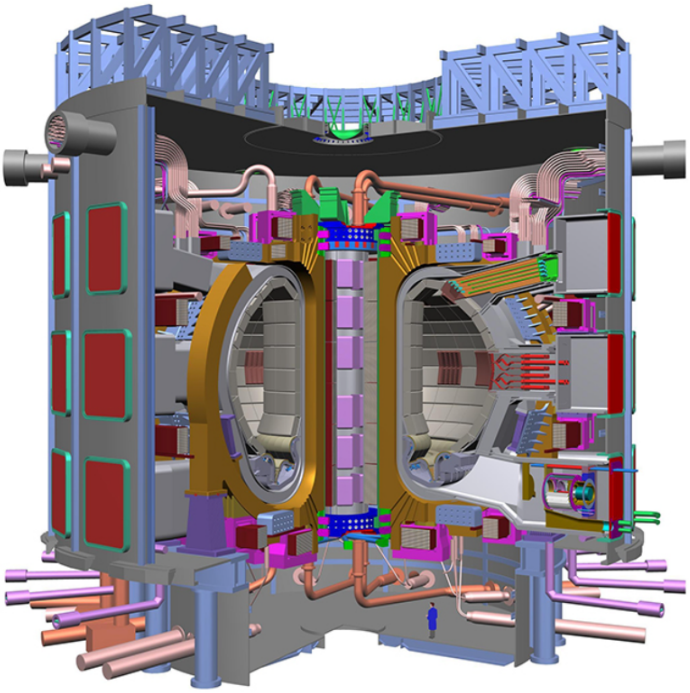

Figure 1.4: ITER experiment

35 countries are collaborating to build and operate the ITER experimental device: the European union, Russia, China, Japan, South Korea, India and the United States. The machine is designed to produce 500 MW fusion power from 50 MW input heating ($Q \geq 10$, where Q is defined as the ratio between the power produced by fusion reactions and the power required to heat the plasma). When operating, ITER will be the World's largest tokamak [2].

1.4 Plasma heating

To bring tokamak plasmas to suitable temperatures for fusion reactions to occur, they must be heated. Three are the possible strategies to achieve this aim: ohmic heating, Radio-Frequency (RF) heating and Neutral Beam Injectors (NBIs).

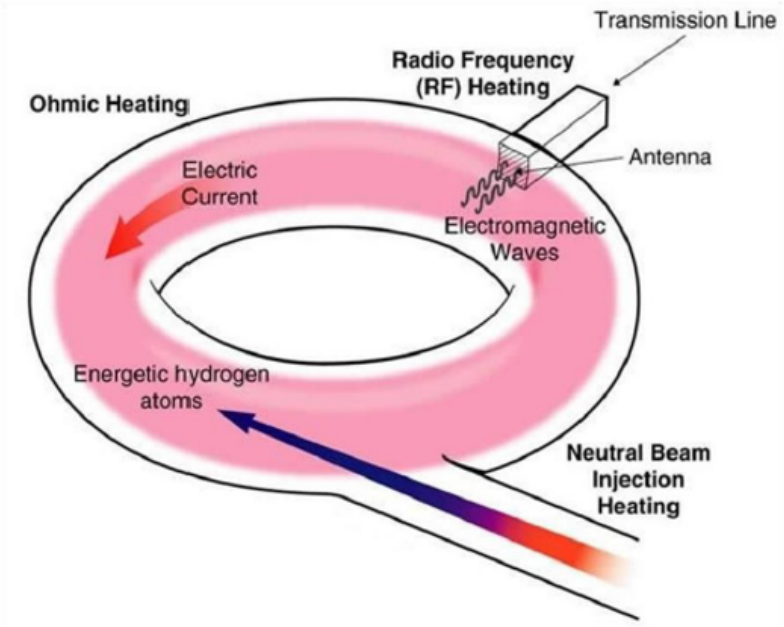

Figure 1.5: Plasma heating strategies

- Ohmic heating
  Like an electric current flowing through a metal wire heats it up, the toroidal plasma current flowing around the tokamak dissipates its energy and heats the plasma. Thanks to the analogy with electricity dissipation in a metal wire, this process is commonly known as ohmic heating. However, the latter only provides the initial heating to plasma tokamaks; in fact, by ohmic heating alone, fusion plasma can be brought to temperatures no higher than few tenth million °C. This is due to the fact that, as plasma temperature T increases, plasma resistivity η decreases ($\eta \propto T^{-3/2}$), therefore collisions are no longer effective in bringing the plasma to higher temperatures [5].
  To reach temperatures on the order of 150 million °C necessary for fusion reactions to occur, ohmic heating must be accompanied by Radio-Frequency heating or Neutral Beam Injectors.

- Radio-Frequency (RF) heating
  Radio-Frequency heating consists in launching electromagnetic (EM) waves inside the tokamak. EM waves penetrate the plasma until they reach the resonance condition and get absorbed transferring their energy to plasma particles. Thanks to this power deposition and by properly choosing the frequency of the injected EM wave, plasmas can be brought to very high temperatures.

- Neutral Beam Injectors (NBIs)
  Finally, the last technique to heat fusion plasmas is based on neutral beam injection that will be more deeply described in the next section.

1.5 Neutral Beam Injectors (NBIs)

Neutral beam injection is based on the injection of highly energetic hydrogen or deuterium atoms inside the tokamak. Since neutral particles are not affected by the presence of the magnetic fields confining the plasma, they travel along straight lines until they are ionized in the collision with a plasma ion or electron according to the following reactions

$$\underline{H} + H^+ \longrightarrow \underline{H}^+ + H \qquad \text{(charge exchange)} \tag{1.5}$$

$$\underline{H} + H^+ \longrightarrow \underline{H}^+ + \underline{e}^- + H^+ \qquad \text{(ion-driven ionization)} \tag{1.6}$$

$$\underline{H} + e^- \longrightarrow \underline{H}^+ + \underline{e}^- + e^- \qquad \text{(electron-driven ionization)} \tag{1.7}$$

where the underscore is exploited to label fast particles and to distinguish them from slower ones. All these reactions feature the production of a positive ion that thermalizes transferring its energy to the plasma through collisions; in this way, energy but also current and momentum can be transferred to the plasma.

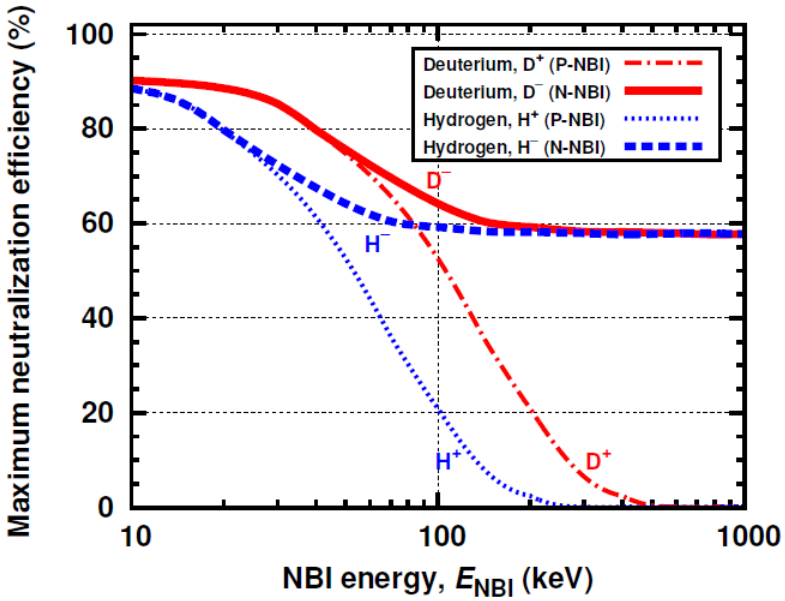

Figure 1.6: Neutralization efficiencies for hydrogen and deuterium ions

NBIs produce a hydrogen or deuterium neutral beam starting from a precursor positive (P-NBI) or negative (N-NBI) ion beam of the same species.
Typically positive ions are exploited for NBIs since much easier to handle than negative ions; in fact, once generated, negative ions gets very easily stripped of their weakly bound (0.75 eV) electron by collision with energetic particles, thus they require much more attention than positive ions to prevent them from being destroyed. However, at 1 MeV energy required by the ITER Heating Neutral Beam (HNB), positive ions become difficult to neutralize. In fact, as shown in figure 1.6, the neutralization efficiency at energies higher than 100 keV remains constant at 60% for negative ions while rapidly drops for positive ions. As a consequence, even though much more difficult to manage, only negative ion NBIs are exploited for highly energetic beams.

1.6 Negative ion Neutral Beam Injectors (N-NBIs)

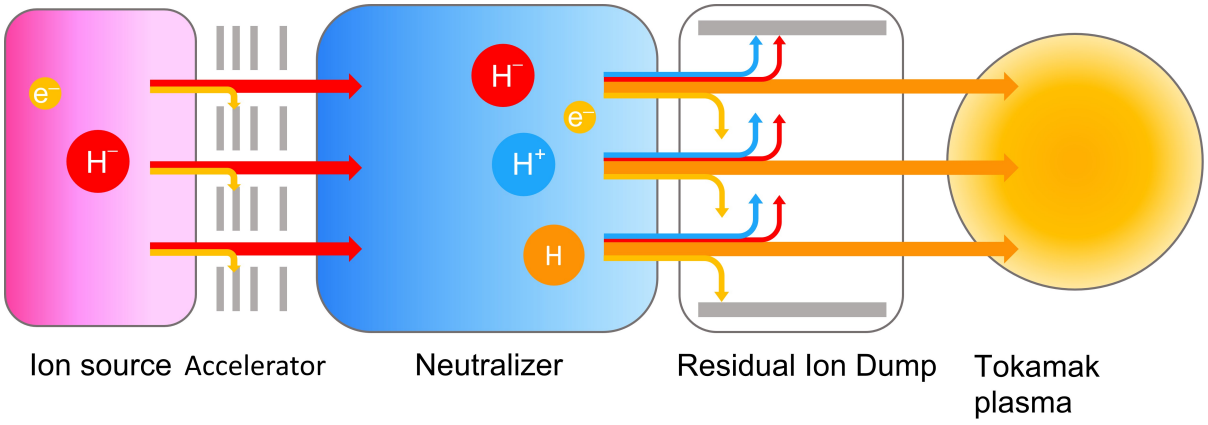

Figure 1.7: Negative ion Neutral Beam Injector

In N-NBIs, negative ions (H^- or D^-) are produced by the source plasma; then they are extracted and accelerated thanks to a system of metallic grids kept at increasing potential. Once the negative beam is fully accelerated to the required energy, it must be neutralized. To comply with this task, the beam passes through a neutralizer consisting of a chamber filled with molecular gas (H_2 or D_2) of the same species of which the beam is composed. Finally, before the neutral beam enters the tokamak, the residual fraction of charged particles is dumped by means of electrostatic fields along the Residual Ion Dump (RID).

1.7 Neutral Beam Test Facility (NBTF)

To heat its plasma, ITER will be equipped with two Heating Neutral Beams (HNBs), each one capable of operating for up to 3600 seconds, delivering deuterium beams of 16.5 MW power and 1 MeV energy. Their combined heating power of 33 MW represents over half of the external heating required by ITER [2].
Creating reliable high energy neutral beams at ITER parameters from a negative ion source will require a large jump in technology. Some of the critical challenges include:

- Extracting a 59 A negative deuterium ion beam from a large-size radiofrequency source;
- Accelerating the negative ion beam to 1 MeV, with a current of 40 A and divergence no higher than 7 mrad;
- Holding high voltage (1 MV) over pulses of 3600 seconds.

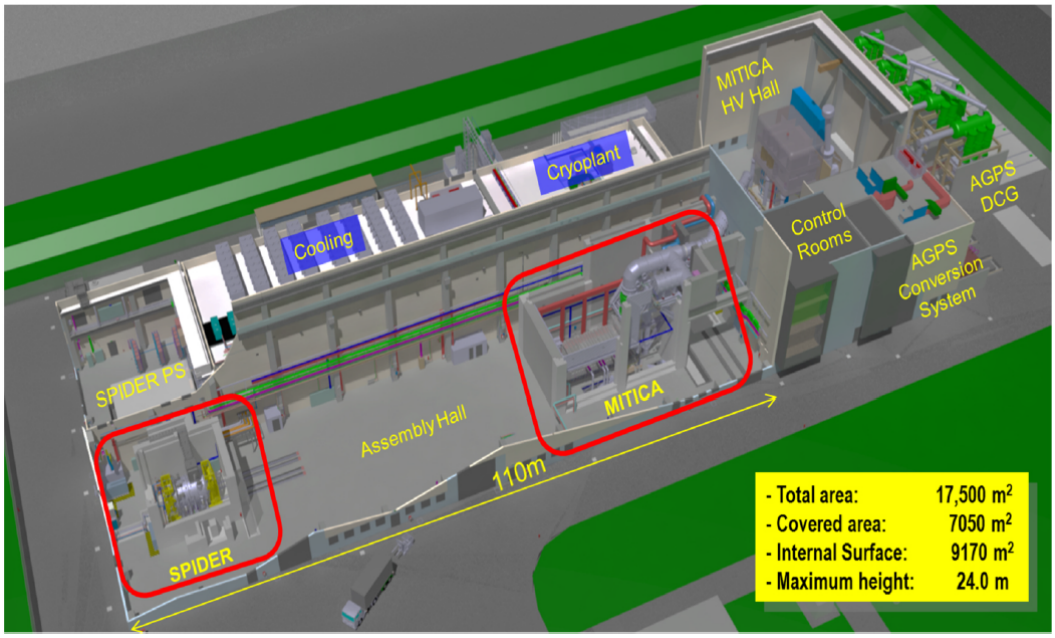

Figure 1.8: Neutral Beam Test Facility (NBTF)

To achieve all these requirements for the ITER tokamak, the Neutral Beam Test Facility (NBTF) was built at Consorzio RFX, in Padova [2]. The NBTF is a 17500 m^2 building hosting two experiments:

- SPIDER (Source for the Production of Ions of Deuterium Extracted from a Radio frequency plasma) is the full-size prototype of the negative ion source and extractor for the ITER heating neutral beam, based on a Radio-Frequency (RF) plasma;
- MITICA (Megavolt ITER Injector and Concept Advancement) is the full-size prototype of the heating neutral beam injectors for ITER.

1.8 The SPIDER experiment

The aim of the SPIDER experiment is the assessment and optimization of H^- or D^- ion beam extraction from a source having the same features and physical dimensions as those envisaged for the ITER NBIs. In particular, SPIDER is designed to:

- Produce and extract a negative ion beam with a current density of 355 A/m^2 in hydrogen or 258 A/m^2 in deuterium;

- Accelerate it up to an energy of 100 keV with a pulse duration of 3600 s.

Views of the actual SPIDER assembly are shown in figure 1.9 and 1.10 along with its operating requirements in table 1.1.

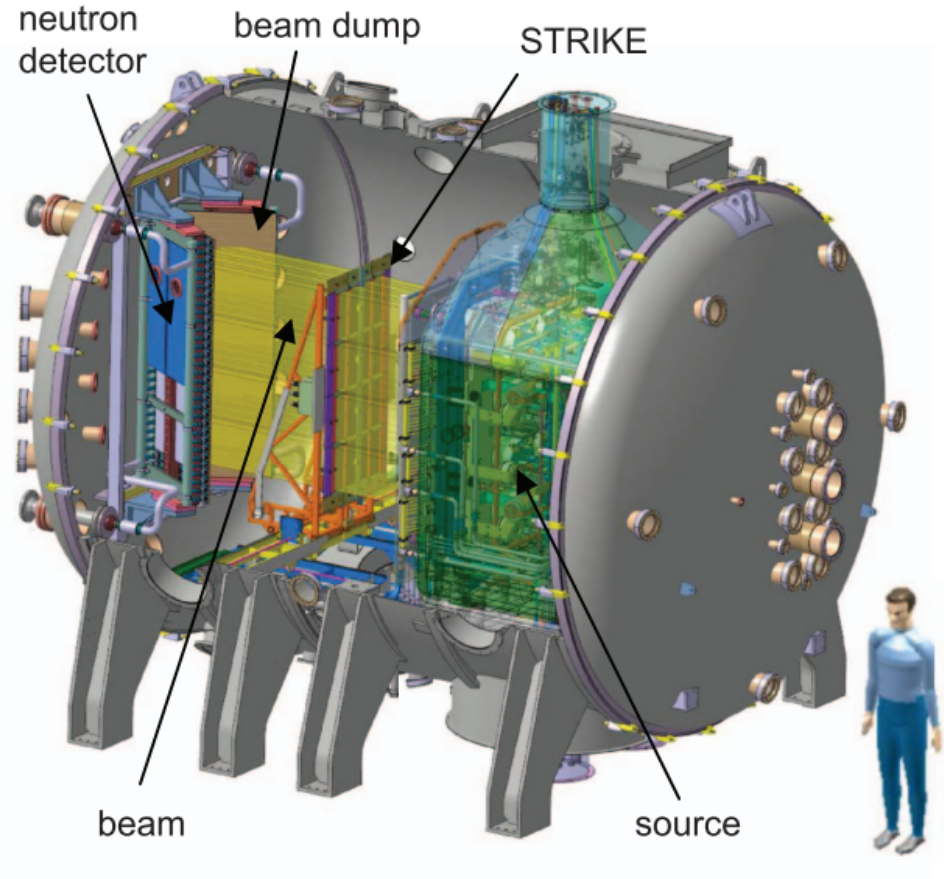

Figure 1.9: SPIDER experiment [10]

Physical quantity	Hydrogen H_2	Deuterium D_2
Beam energy	100 keV	
Beam current density	355 A/m^2	258 A/m^2
Beam pulse duration	3600 s	
Fraction of co-extracted electrons	< 0.5	< 1
Beam uniformity	$> 10\,\%$	
Maximum source filling pressure	0.3 Pa	
Divergence	< 7 mrad	

Table 1.1: SPIDER requirements

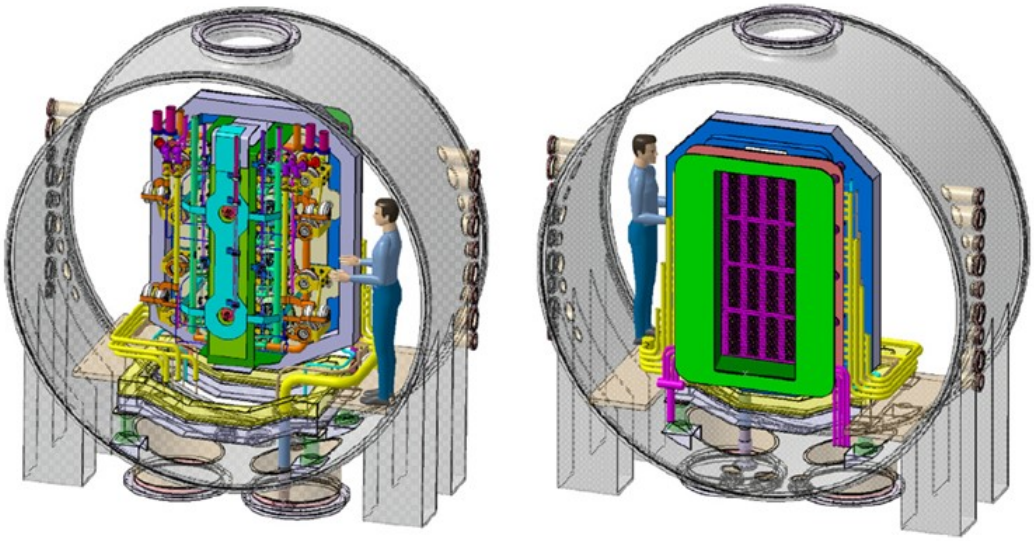

Figure 1.10: Rear (left) and front (right) side of SPIDER's source and accelerator [9]

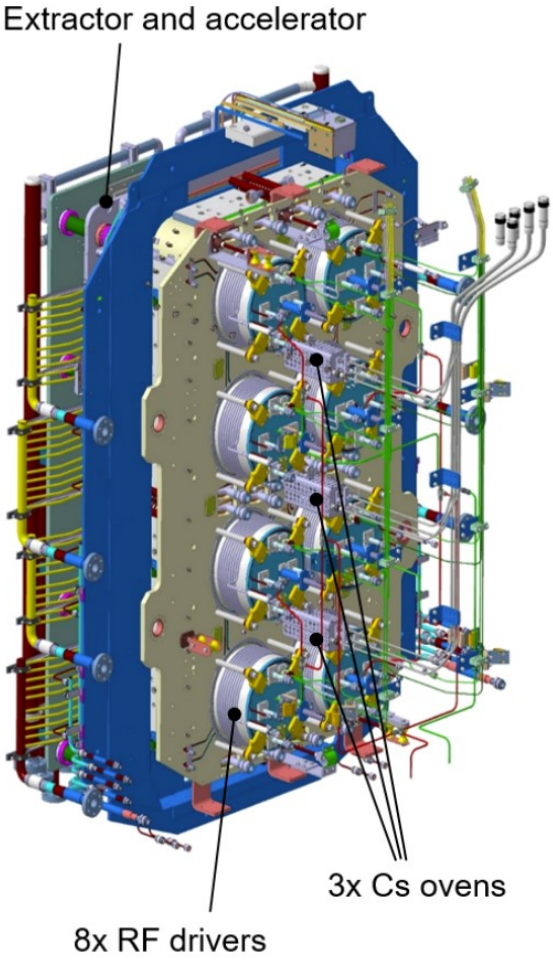

Figure 1.11: Rear side of the source: drivers and caesium ovens

The beam source is contained in a 6 m long stainless steel cylindrical vessel having 4 m

diameter. The gas (H_2 or D_2) is injected in the rear part of the source inside eight cylindrical chambers called drivers at a pressure of 0.3 Pa. Plasma is generated inside the drivers connected to the expansion chamber through which plasma can diffuse. Each driver can be supplied with 100 kW power at 1 MHz frequency by means of RF coils wounded around it. Three caesium ovens located in the rear part of the source evaporate caesium and spread it inside the source to lower the work function of the metallic surfaces so as to significantly enhance the production of negative ions that will be extracted.
The accelerating column is composed of three grids: Plasma Grid (PG), Extraction Grid (EG) and Grounded Grid (GG), each one featuring 1280 apertures, arranged in 4×4 groups of 5×16 apertures.

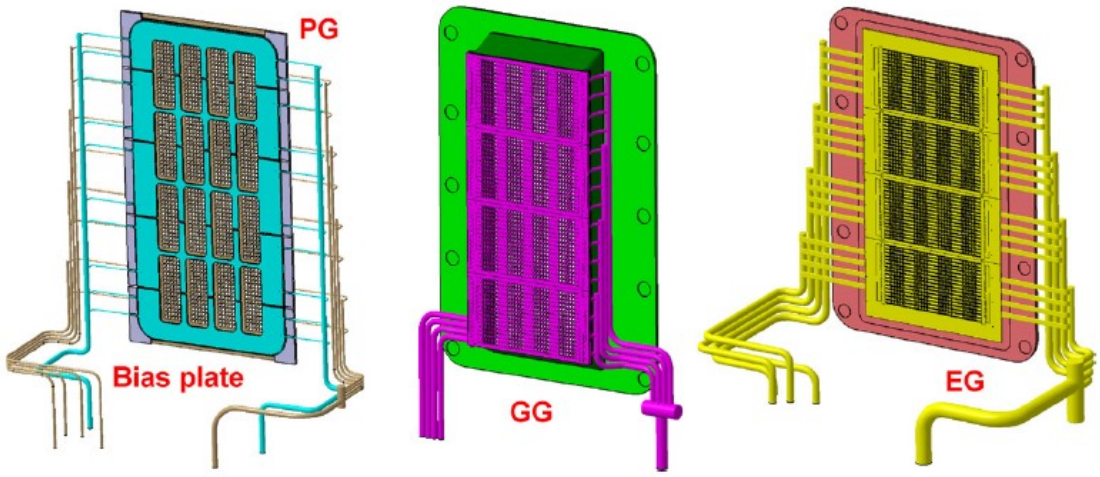

Figure 1.12: Accelerator grids [9]

The Plasma Grid separates the source from the accelerating column, a bias plate (BP) electrode is mounted 10 mm upstream of the PG and can be used to adjust the electric field to maximize the extracted ion current and to reduce the number of co-extracted electrons. In the plasma source a magnetic filter field on the order of few mT is produced by a current flowing through the PG to prevent hot electrons ($T > 2$ eV) from reaching the extraction region and destroying negative ions produced in proximity of the PG.
When a 10 kV negative voltage is applied between the PG and the EG, H^- or D^- ions are extracted through the 1280 PG apertures. The extracted ions are then accelerated up to 100 keV thanks to the 90 kV negative voltage between the EG and the grounded grid. Since electrons are unavoidably extracted along with negative ions, permanent magnets are located in the EG to deflect and dump electrons onto the EG. This arrangement produces also an undesired deflection of the ions that is corrected by properly arranged compensating magnets [8].
After being fully accelerated, the entire beam made of 1280 beamlets travels along the vessel reaching the beam dump consisting of two walls arranged in a V-shape configuration and terminates its propagation [12].
Finally, to investigate and optimize the source and the beam, various types of diagnostics are exploited. In particular, the focus of this thesis work is on beam diagnostics among which Beam Emission Spectroscopy (BES) and beam tomography.

Chapter 2

Thesis motivation

During the 2021 SPIDER experimental campaign, Beam Emission Spectroscopy (BES) and beam tomography measurements were performed whose results left some unanswered points.

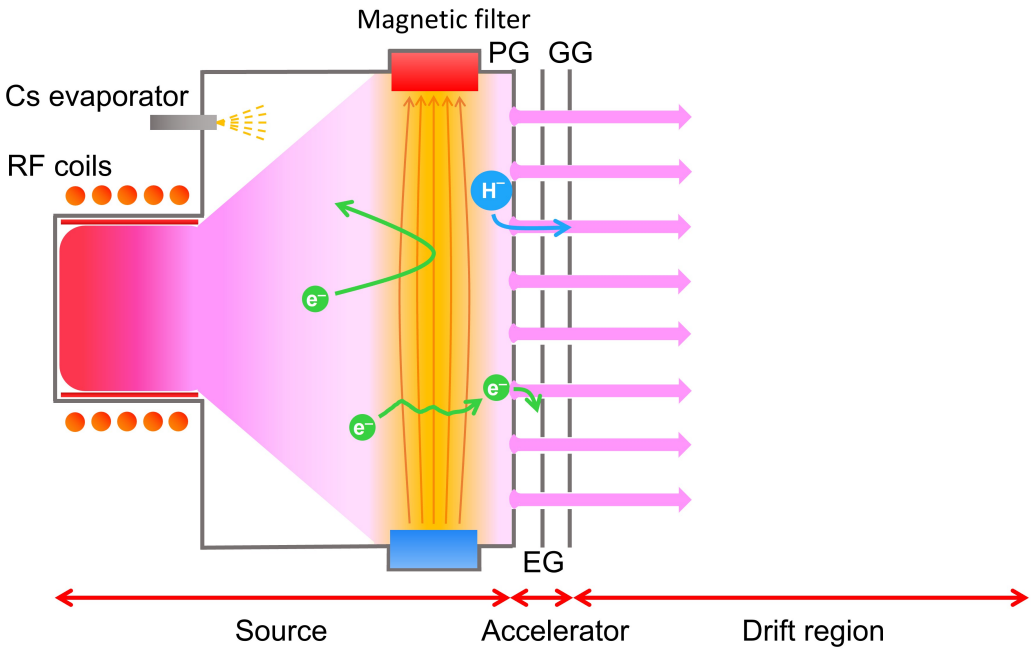

Figure 2.1: General scheme for a negative ion source and extractor system

2.1 Beam Emission Spectroscopy (BES)

The first point concerns Beam Emission Spectroscopy (BES). BES is a diagnostic system based on the measurement of the α-Balmer (B_α) radiation spontaneously emitted during the interaction of the SPIDER beam with the background gas along the drift region. An example of BES spectrum taken during the 2021 SPIDER campaign is shown in Figure 2.2, where two peaks are visible: a Doppler shifted and an unshifted peak.

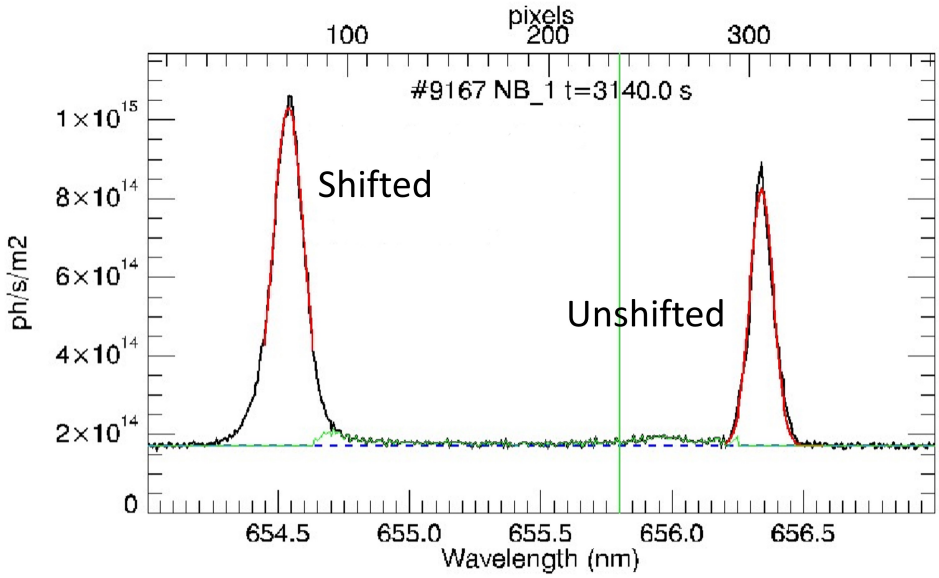

Figure 2.2: Example of BES spectrum measured during the 2021 SPIDER campaign.

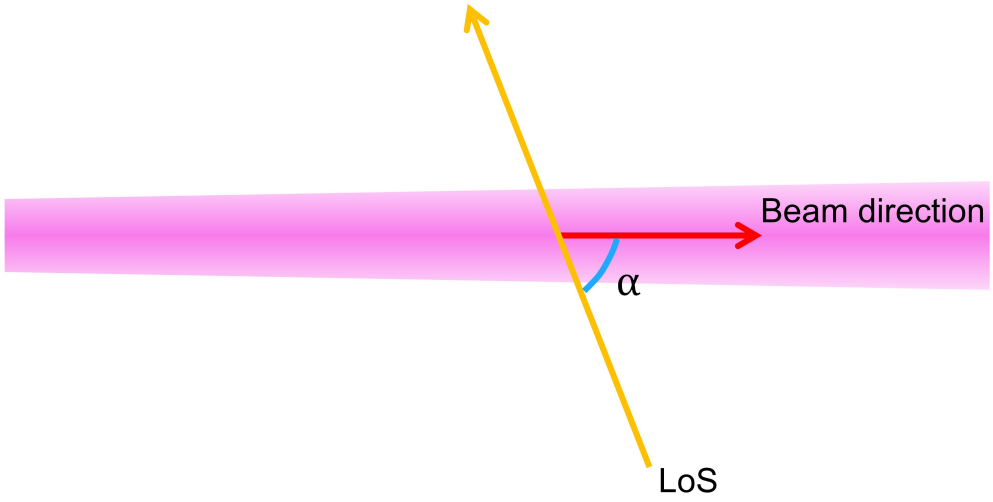

Figure 2.3: SPIDER beamlet and BES Line of Sight

The shifted peak accounts for the emission by fast excited beam atoms. In fact, since beam particles are moving, the wavelength of the emitted radiation is Doppler shifted according to the following relation

$$\lambda' = \lambda_0 \frac{1 - \beta \cos \alpha}{\sqrt{1 - \beta^2}} \tag{2.1}$$

where λ' and λ_0 are the observed and the nominal transition wavelengths respectively, β the ratio between the speed of beam particles and the speed of light, α the angle between the beam particle velocity and the direction of propagation of the detected photons, the latter represented by the BES Line of Sight (LoS) [17]. For hydrogen beams, the nominal

B_α wavelength is given by $\lambda_0 = 656.28\,\text{nm}$. λ' is red or blue shifted according to the value of α [17]. Since in SPIDER the LoS inclination angle α was set to 75°, the peak in the BES spectrum results blue shifted. Doppler shifted B_α photons can be emitted by decayment of fast n=3 excited atoms to the n=2 state produced by way of the following interactions [17]:

$$\underline{H}^- + H_2 \longrightarrow \underline{H}(n=3) + \underline{e}^- + H_2 \tag{2.2}$$

$$\underline{H} + H_2 \longrightarrow \underline{H}(n=3) + H_2 \tag{2.3}$$

$$\underline{H}^+ + H_2 \longrightarrow \underline{H}(n=3) + H_2^+ \tag{2.4}$$

Instead, the unshifted peak accounts for the B_α emission from n=3 slow excited atoms (few eV) that can be produced in the fragmentation of the target gas according to the following reactions:

$$\underline{H}^\pm + H_2 \longrightarrow \underline{H}^\pm + H + H(n=3) \tag{2.5}$$

$$\underline{H} + H_2 \longrightarrow \underline{H} + H + H(n=3) \tag{2.6}$$

$$\underline{e}^- + H_2 \longrightarrow \underline{e}^- + H + H(n=3) \tag{2.7}$$

$$e^- + H_2 \longrightarrow e^- + H + H(n=3) \tag{2.8}$$

$$e^- + H_2^+ \longrightarrow H + H(n=3) \tag{2.9}$$

where the underscore labels fast beam particles.
Since for slow atoms $\beta \sim 0$, the relation in 2.1 reduces to $\lambda' = \lambda_0$ and thus the unshifted peak results centred around the nominal value λ_0.
The first target of this thesis work consists in finding how much all these processes for both fast and slow particles contribute to the total B_α emission so as to justify the comparable amplitude of the two shifted and unshifted peaks in the BES spectrum.

2.2 Beam tomography

The second point regards instead beam tomography. Beam emission tomography reconstructs the 2D emissivity profile $\epsilon(y,z)$ by measuring the integrated B_α radiation along a suitable number of Lines of Sight (LoSs). A set of visible cameras mounted all around the beam collect the integrated optical signals coming from a fan of LoSs lying on a plane perpendicular to the beam direction (x-direction) as in figure 2.5.
The measured radiation f_j (brightness) integrated over the emitting area S_j seen from the j-th LoS depends on the emissivity profile $\epsilon(y,z)$ perpendicular to the beam direction of propagation according to the following integral [13]:

$$f_j = \int_{S_j} \epsilon(y,z)\, dy\, dz \tag{2.10}$$

Several algorithms can be used to invert it and find the emissivity profile $\epsilon(y,z)$ of the beam, but this will not be the aim of this thesis work [14].

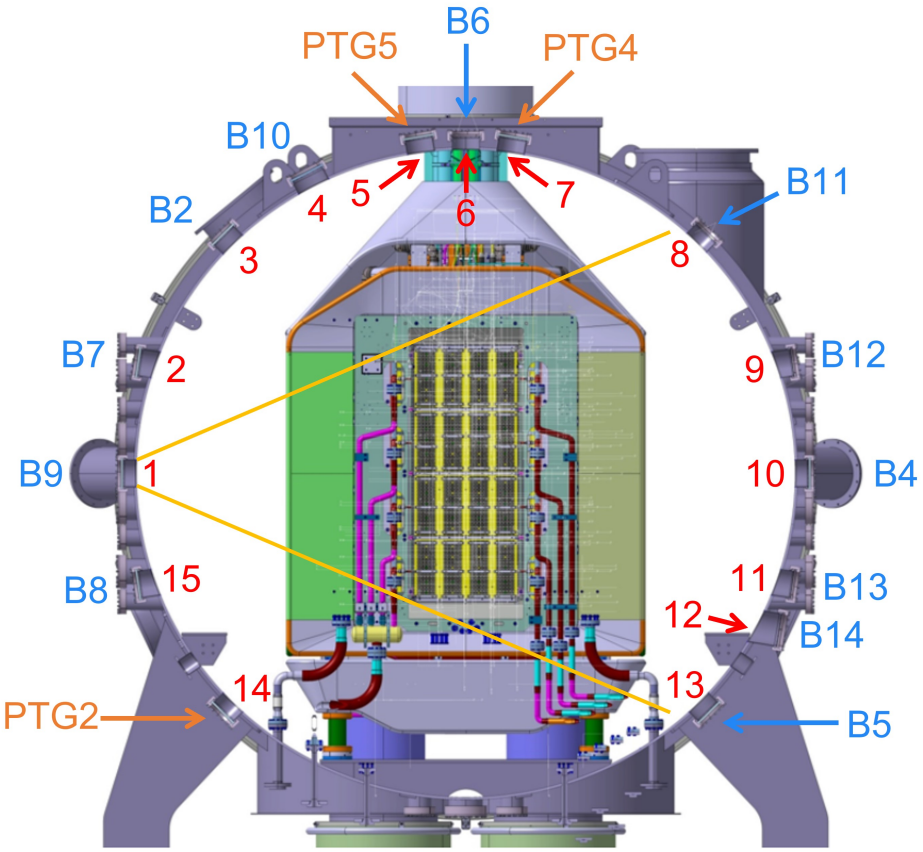

Figure 2.4: Section of SPIDER vessel with the installed cameras. The notation B# in blue labels a Basler camera, instead PTG# in orange a PointGrey camera [13]. The numbers in red enumerate the camera view ports. Finally, the yellow lines represent the LoSs for the B9 camera installed in the port 1.

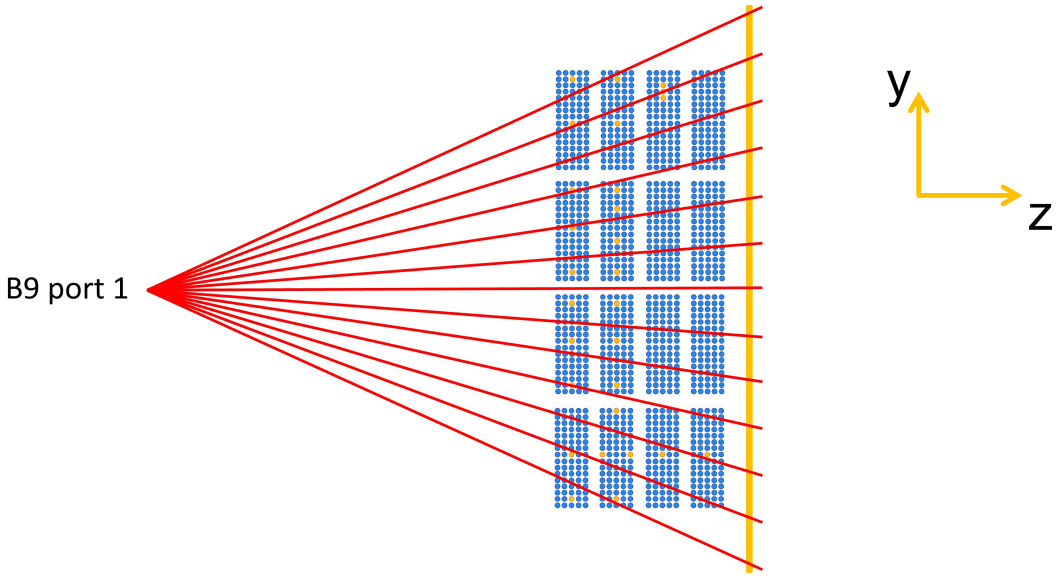

Figure 2.5: Fan of LoSs for camera B9 port 1

A tomography profile collected during the 2021 SPIDER experimental campaign from camera B9 port 1 is shown in figure 2.6.

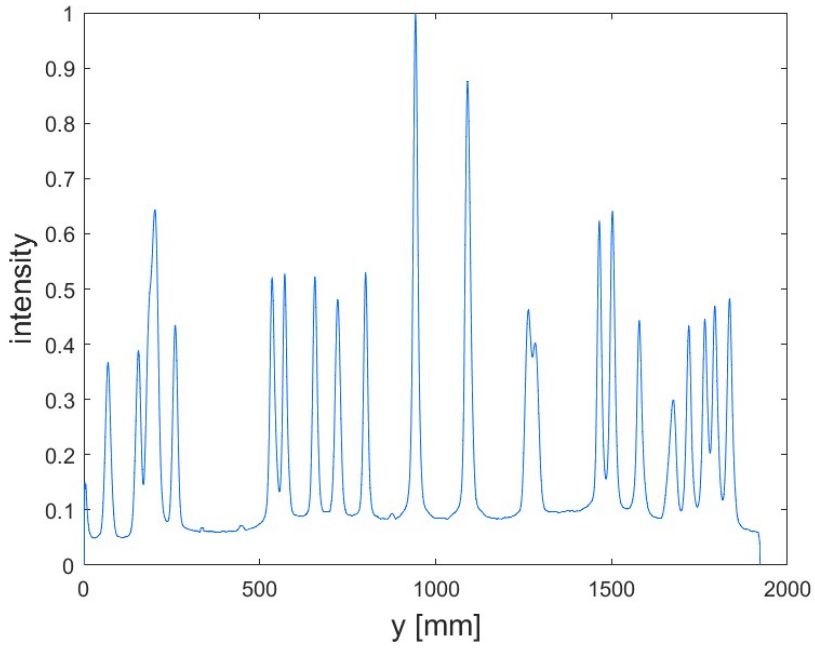

Figure 2.6: Beam tomography spectrum from camera B9 port 1 measured with the LoS pattern of figure 2.5. More specifically, each one of the points on the horizontal axis represents the y coordinate of the single LoS intersection point with the vertical yellow bar of figure 2.5; the vertical axis, instead, is the result of the integration along that specific line of sight normalized to the height of the highest peak. The experimental data are represented in blue.

What can be observed in figure 2.6 is the presence of a luminous background on the entire beam section, even in the space between one beamlet and the others, but the origin of that luminosity has not yet been clarified.
To conclude, the second target of this thesis work consists in finding the processes or the reasons leading to the formation of that luminous background present in the beam tomography spectrum.

2.3 Thesis motivation and aim

To summarize, this thesis work aims at investigating the two experimental observations described in the two previous sections by means of numerical simulations. In particular, the evolution of beam species and the formation of the beam plasma during the beam propagation. In addition, this work aims at giving a deeper understanding regarding the beam propagation for the future experimental campaigns and being of inspiration for a future improvements to optimize SPIDER operations.

Chapter 3

Beam composition

The aim of this chapter is to outline how SPIDER beam species evolve while the beam propagates along the drift region; this will be performed by means of numerical simulations, in particular, codes written in MATLAB will be exploited.

3.1 Beam composition with no atomic emission

This section will be devoted to investigating how the beam composition evolves while propagating along the drift region but, for the moment, without considering the possibility for atoms to be excited and decay to lower energy levels with ensuing emission of radiation. To comply with this task the beam propagation is modelled with a MATLAB 1D simulation.
The algorithm solves the system of differential equations 3.1 found in [16] describing how SPIDER beam species evolve along the drift region due to the interaction with the background, composed of partially ionized gas. Beam particle fluxes of hydrogen negative ions Γ^{H^-}, atoms Γ^{H}, positive ions Γ^{H^+} and electrons Γ^{se} stripped from atoms or negative ions evolve according to the following system of equations:

$$\begin{cases} \dfrac{d\Gamma^{H^-}}{dx} = -\Gamma^{H^-} \displaystyle\sum_k \left(\sigma^k_{-10} + \sigma^k_{-11}\right) n_k \\ \dfrac{d\Gamma^{H}}{dx} = \Gamma^{H^-} \displaystyle\sum_k \sigma^k_{-10}\, n_k + \Gamma^{H^+} \sum_k \sigma^k_{10}\, n_k - \Gamma^{H} \sum_k \sigma^k_{01}\, n_k \\ \dfrac{d\Gamma^{+}}{dx} = \Gamma^{H^-} \displaystyle\sum_k \sigma^k_{-11}\, n_k + \Gamma^{H} \sum_k \sigma^k_{01}\, n_k - \Gamma^{H^+} \sum_k \sigma^k_{10}\, n_k \\ \dfrac{d\Gamma^{se}}{dx} = \Gamma^{H^-} \displaystyle\sum_k \left(\sigma^k_{-10} + 2\sigma^k_{-11}\right) n_k + \Gamma^{H} \sum_k \sigma^k_{01}\, n_k - \Gamma^{se} \sum_k \sigma^k_{m}\, n_k \end{cases} \tag{3.1}$$

where σ^k_{ij} denotes the cross sections for collisions on the k target species of a hydrogen beam particle having initial charge state i and final state charge j. Projectile-target interactions are treated as two-body collisions where the target species k can be molecular hydrogen, atomic hydrogen, plasma ions or electrons [16].

#	σ	reaction	name	reference	comment
1	σ_{-10}	$\underline{H}^- + H_2 \longrightarrow \underline{H} + \underline{e}^- + H_2$	stripping	[18]	-
2	σ_{-11}	$\underline{H}^- + H_2 \longrightarrow \underline{H}^+ + 2\underline{e}^- + H_2$	double stripping	[18]	-
3	σ_{01}	$\underline{H} + H_2 \longrightarrow \underline{H}^+ + \underline{e}^- + H_2$	ionization	[18]	-
4	σ_{10}	$\underline{H}^+ + H_2 \longrightarrow \underline{H} + H_2^+$	charge exchange	[18]	-
5	σ_m	$\underline{e}^- + H_2 \longrightarrow \underline{e}^- + H_2$	momentum transfer	[18]	a)

Table 3.1: Beam species interaction included in the model

a) Since the electron momentum transfer cross section was not found in literature, σ_m is replaced with the elastic scattering cross section for electron impact on H_2.

The first equation in 3.1 shows how the negative ion flux is decreased by single and double electron detachment, also known as stripping and double stripping. In the second equation, the flux of neutral atoms is increased by neutralization of both positive and negative ions, due to single stripping and charge exchange respectively, whilst the loss term accounts for the ionization of the neutral atoms. The third equation points out that the proton flux is increased by double stripping and ionization, while reduced by neutralization by charge exchange. Finally, the fourth equation introduces the flux of fast electrons with energy $E_{se} = (m_e/m_i)E_b \sim 26\,\text{eV}$ stripped from neutral atoms or negative ions; where E_b =48 keV denotes the beam energy, m_e and m_i the electron and proton mass respectively. The loss term for this kind of electrons is given by the momentum transfer cross section σ_m^k representing the complete loss of the electron parallel velocity.

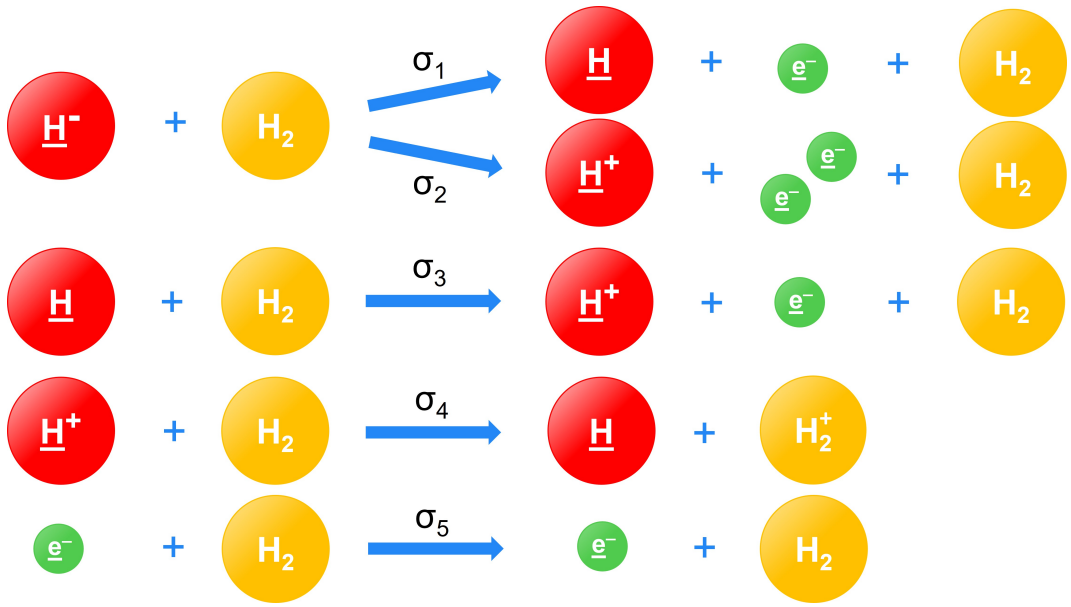

Figure 3.1: Scheme for all the reactions included in the model. The blue arrows indicate the possible outcomes for the reaction on the left-hand side

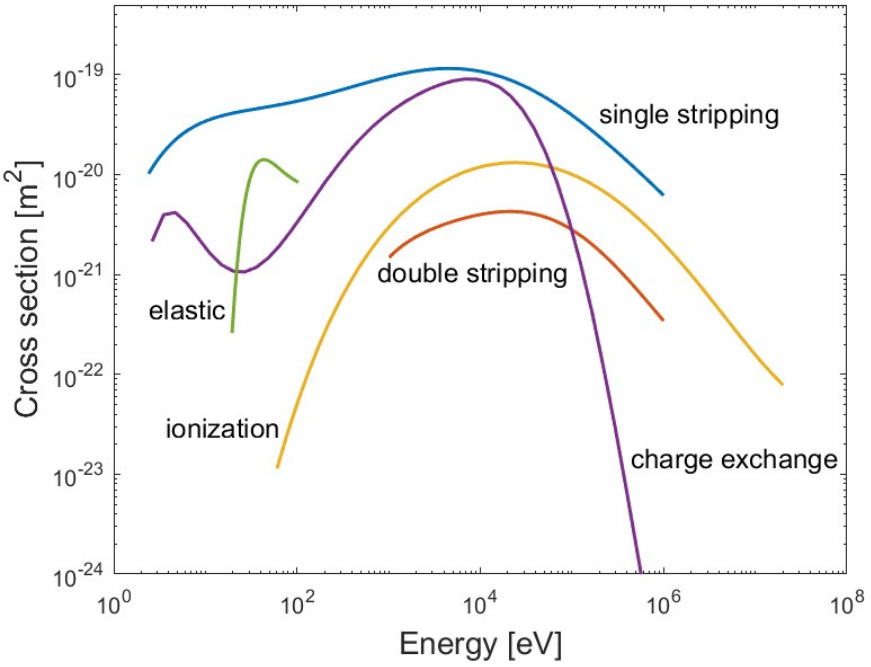

Figure 3.2: Cross sections included in the model

To reproduce SPIDER's conditions along the drift region during the 2021 experimental campaign, the H_2 background gas pressure is uniformly set to $p = 0.03\,\text{Pa}$ corresponding to $n_{H_2} = 7.2 \cdot 10^{18}\,\text{m}^{-3}$ gas density; moreover, it is assumed that the single beamlet at the accelerator exit is fully composed of negative hydrogen ions featuring $I = 25\,\text{mA}$ current and $E_b = 48\,\text{keV}$ energy corresponding to $n_b = 3.5 \cdot 10^{14}\,\text{m}^{-3}$ beam density.
To simplify the numerical computation, some approximations can be made: since the densities of plasma ions, plasma electrons and dissociated atoms produced during the interaction of the beam with the molecular gas are at least 3 orders of magnitude lower than the density of the molecular gas itself, the first approximation consists in considering only reactions having H_2 as target, hence the system of equations 3.1 can be simplified in the following way:

$$\begin{cases} \dfrac{d\Gamma^{H^-}}{dx} = -\Gamma^{H^-}\left(\sigma_{-10} + \sigma_{-11}\right) n_{H_2} \\ \dfrac{d\Gamma^{H}}{dx} = \Gamma^{H^-}\,\sigma_{-10}\,n_{H_2} + \Gamma^{H^+}\,\sigma_{10}\,n_{H_2} - \Gamma^{H}\,\sigma_{01}\,n_{H_2} \\ \dfrac{d\Gamma^{H^+}}{dx} = \Gamma^{H^-}\,\sigma_{-11}\,n_{H_2} + \Gamma^{H}\,\sigma_{01}\,n_{H_2} - \Gamma^{H^+}\,\sigma_{10}\,n_{H_2} \\ \dfrac{d\Gamma^{se}}{dx} = \Gamma^{H^-}\left(\sigma_{-10} + 2\sigma_{-11}\right) n_{H_2} + \Gamma^{H}\,\sigma_{01}\,n_{H_2} - \Gamma^{se}\,\sigma_m\,n_{H_2} \end{cases} \tag{3.2}$$

where the sum over the k target species disappears since only molecular hydrogen is considered and n_k is replaced by n_{H_2}. Furthermore, in order to solve them, the previous equations are expanded to the first order, discretized and rearranged as follows

$$
\begin{cases}
\Gamma^{H^-}(i) = \Gamma^{H^-}(i-1) - \Gamma^{H^-}(i-1)\,(\sigma_{-10} + \sigma_{-11})\,n_{H_2}\,dx \\
\Gamma^{H}(i) = \Gamma^{H}(i-1) + \Gamma^{H^-}(i-1)\,\sigma_{-10}\,n_{H_2}\,dx + \Gamma^{H^+}(i-1)\,\sigma_{10}\,n_{H_2}\,dx + \\
\qquad - \Gamma^{H}(i-1)\,\sigma_{01}\,n_{H_2}\,dx \\
\Gamma^{H^+}(i) = \Gamma^{H^+}(i-1) + \Gamma^{H^-}(i-1)\,\sigma_{-11}\,n_{H_2}\,dx + \Gamma^{H}(i-1)\,\sigma_{01}\,n_{H_2}\,dx + \\
\qquad - \Gamma^{H^+}(i-1)\,\sigma_{10}\,n_{H_2}\,dx \\
\Gamma^{se}(i) = \Gamma^{se}(i-1) + \Gamma^{H^-}(i-1)(\sigma_{-10} + 2\sigma_{-11})\,n_{H_2}\,dx + \Gamma^{H}(i-1)\,\sigma_{01}\,n_{H_2}\,dx + \\
\qquad - \Gamma^{se}(i-1)\,\sigma_m\,n_{H_2}\,dx
\end{cases}
\tag{3.3}
$$

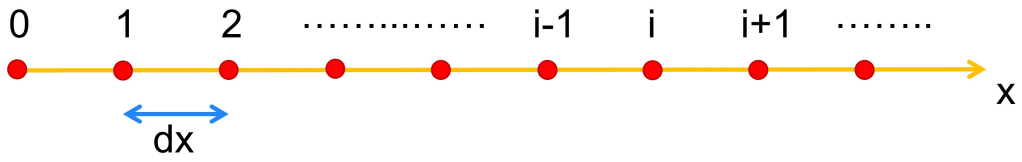

Figure 3.3: Discretization of the beam direction of propagation

where the beam is assumed to propagate along the x direction discretized in many arbitrary small steps of length dx. Each equation represents the flux $\Gamma^m(i)$ of the m beam species at the i-th position, that is determined by the flux at the previous (i-1)-th step to which gain and loss terms are added.

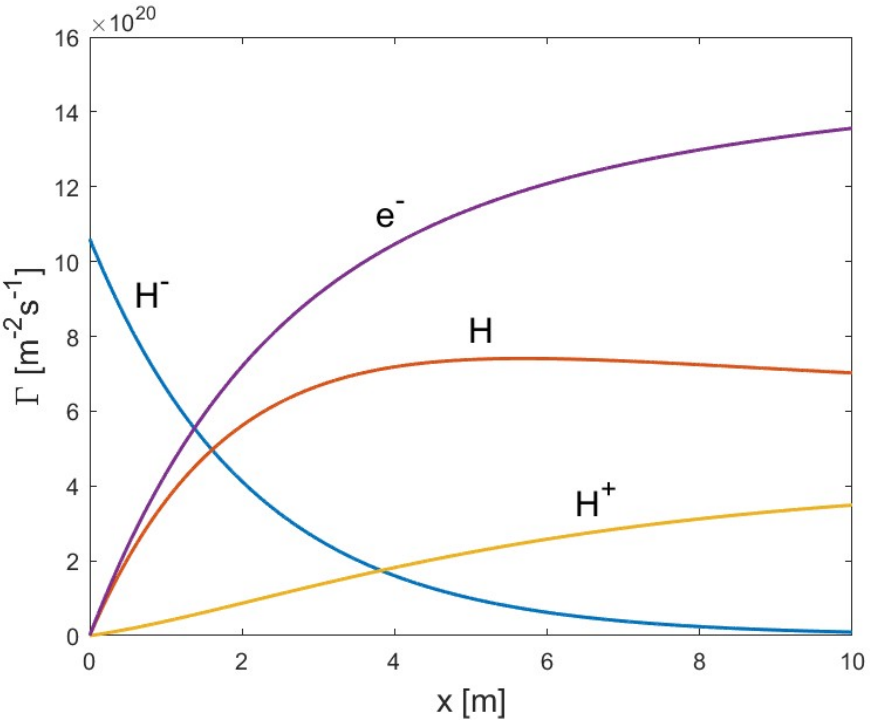

Figure 3.4: Beam composition resulting from the simulation

Figure 3.4 shows the results of the simulation where the particles fluxes are represented as a function of the distance x travelled by the single beamlet along the drift region. As expected, the interaction of the beam with the background gas changes the beam particle composition: the population of negative ions exponentially decreases due to losses by both stripping and double stripping. As a consequence, the beam populations of positive ions, neutral atoms and stripped electrons initially increase. At large distance from the accelerator exit, instead, since the number of negative ions is strongly reduced, the ionization of neutral atoms takes over stripping processes resulting in the flattening of the neutral atom profile and in a further increase of the positive ions flux.

3.2 Hydrogen transitions

So far, the possibility that beam hydrogen atoms can be found in their excited states was not considered. However, to investigate the luminous background in the tomography spectrum of figure 2.6, excited atom species must be included in the model. A scheme of the transition that will be considered is shown in figure 3.5.

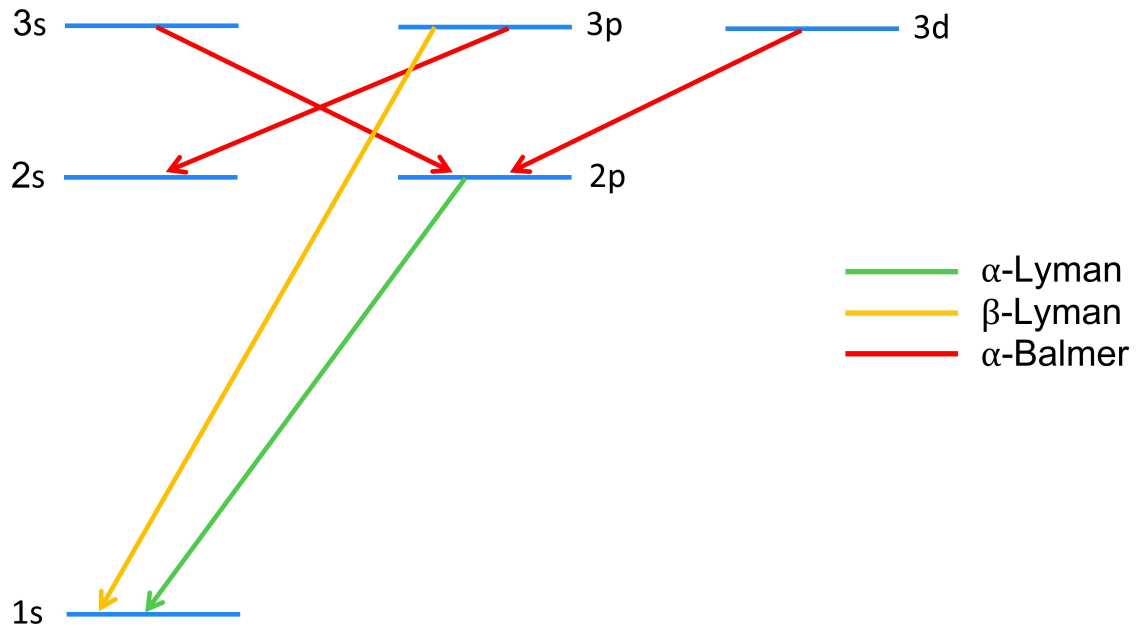

Figure 3.5: Allowed hydrogen transitions included in the model

Only states up to the n=3 energy levels decaying to lower levels and emitting α-Lyman, β-Lyman or α-Balmer will be included. Yet, selection rules allow only 5 among the possible transitions between these states, namely those obeying:

- Δn = any integer value;
- $\Delta\ell = \pm 1$;

where Δn is the difference between the principal quantum number of the initial and the final state and $\Delta\ell$ the same for the angular momentum quantum number. All the possible

transitions are reported in table 3.2 along with their decay times and wavelengths taken from [23].

transition	$\lambda_{i\to j}$ $[nm]$	$A_{i\to j}$ $[s^{-1}]$	$\tau_{i\to j}$ $[ns]$	name	$br_{i\to j}$
2s $\to$ 1s	-	-	-	-	-
2p $\to$ 1s	121.57	$6.26 \cdot 10^8$	1.6	α-Lyman	1.00
3s $\to$ 1s	-	-	-	-	-
3s $\to$ 2s	-	-	-	-	-
3s $\to$ 2p	656.28	$3.16 \cdot 10^6$	316	α-Balmer	1.00
3p $\to$ 1s	102.57	$6.26 \cdot 10^8$	1.6	β-Lyman	0.88
3p $\to$ 2s	656.27	$2.24 \cdot 10^7$	45	α-Balmer	0.12
3p $\to$ 2p	-	-	-	-	-
3d $\to$ 1s	-	-	-	-	-
3d $\to$ 2s	-	-	-	-	-
3d $\to$ 2p	656.28	$4.31 \cdot 10^7$	23	α-Balmer	1.00

Table 3.2: Atomic hydrogen transitions [23]. Transitions marked with the - sign are not allowed by selection rules. λ_{ij} is the wavelength for the decayment from the initial state i to the final state j and A_{ij} the spontaneous emission Einstein's coefficient of the decayment process.The characteristic time τ_{ij} of the decayment is nothing but the reciprocal of A_{ij}. $\text{br}_{i\to j}$ is the branching ratio for the transition.

$\text{A}_{i\to j}$ represents the Einstein coefficient for spontaneous emission from the initial state i to the final state j; the reciprocal of the spontaneous emission coefficient denotes the characteristic time $\tau_{i\to j}$ of the specific decayment, namely the time required to reduce the initial population of the emitting species by a factor 1/e. Furthermore, the 3p state can both decay to the 1s or to the 2s state, thus the branching ratios for the 3p state must be specified and can be computed by way of the following formulae exploiting the spontaneous emission coefficients:

$$br_{3p\to 1s} = \frac{A_{3p\to 1s}}{A_{3p\to 1s} + A_{3p\to 2s}} = 0.88 \qquad br_{3p\to 2s} = \frac{A_{3p\to 2s}}{A_{3p\to 1s} + A_{3p\to 2s}} = 0.12 \tag{3.4}$$

The 3p state decays 88% of the times to the 1s state, while the remaining 12% to the 2s state. All the other excited states decay 100% of the times to the same lower state, therefore $br_{i\to j} = 1$.

3.3 Beam composition including atomic emission

In this section, interactions of excited atom species are included in the 1D model. In particular, the exploited processes are listed in table 3.3 specified only up to the n=3 energy level.

#	σ	reaction	name	reference	comment
1	$\sigma_{-10_{tot}}$	$\underline{H}^- + H_2 \longrightarrow \underline{H}(tot) + \underline{e}^- + H_2$	stripping	[18]	a)
2	$\sigma_{-10_{1s}}$	$\underline{H}^- + H_2 \longrightarrow \underline{H}(1s) + \underline{e}^- + H_2$	stripping	-	b)
3	$\sigma_{-10_{2s}}$	$\underline{H}^- + H_2 \longrightarrow \underline{H}(2s) + \underline{e}^- + H_2$	stripping	[19]	c)
4	$\sigma_{-10_{2p}}$	$\underline{H}^- + H_2 \longrightarrow \underline{H}(2s) + \underline{e}^- + H_2$	stripping	[19]	c)
5	$\sigma_{-10_{3s}}$	$\underline{H}^- + H_2 \longrightarrow \underline{H}(3s) + \underline{e}^- + H_2$	stripping	[19]	c)
6	$\sigma_{-10_{3p}}$	$\underline{H}^- + H_2 \longrightarrow \underline{H}(3p) + \underline{e}^- + H_2$	stripping	[19]	c) d)
7	$\sigma_{-10_{3d}}$	$\underline{H}^- + H_2 \longrightarrow \underline{H}(3d) + \underline{e}^- + H_2$	stripping	[19]	c) d)
8	σ_{-11}	$\underline{H}^- + H_2 \longrightarrow \underline{H}^+ + 2\underline{e}^- + H_2$	double stripping	[18]	
9	$\sigma_{0_{1s}1}$	$\underline{H}(1s) + H_2 \longrightarrow \underline{H}^+ + \underline{e}^- + H_2$	ionization	[18]	-
10	$\sigma_{0_{2s}1}$	$\underline{H}(2s) + H_2 \longrightarrow \underline{H}^+ + \underline{e}^- + H_2$	ionization	[18]	-
11	$\sigma_{0_{2p}1}$	$\underline{H}(2p) + H_2 \longrightarrow \underline{H}^+ + \underline{e}^- + H_2$	ionization	-	e)
12	$\sigma_{0_{3s}1}$	$\underline{H}(3s) + H_2 \longrightarrow \underline{H}^+ + \underline{e}^- + H_2$	ionization	-	e)
13	$\sigma_{0_{3p}1}$	$\underline{H}(3p) + H_2 \longrightarrow \underline{H}^+ + \underline{e}^- + H_2$	ionization	-	e)
14	$\sigma_{0_{3d}1}$	$\underline{H}(3d) + H_2 \longrightarrow \underline{H}^+ + \underline{e}^- + H_2$	ionization	-	e)
15	$\sigma_{0_{1s}0_{2s}}$	$\underline{H}(1s) + H_2 \longrightarrow \underline{H}(2s) + H_2$	excitation	[18]	-
16	$\sigma_{0_{1s}0_{2p}}$	$\underline{H}(1s) + H_2 \longrightarrow \underline{H}(2p) + H_2$	excitation	[18]	f)
17	$\sigma_{0_{1s}0_{3s}}$	$\underline{H}(1s) + H_2 \longrightarrow \underline{H}(3s) + H_2$	excitation	[18]	-
18	$\sigma_{0_{1s}0_{3p}}$	$\underline{H}(1s) + H_2 \longrightarrow \underline{H}(3p) + H_2$	excitation	[18]	g)
19	$\sigma_{0_{1s}0_{3d}}$	$\underline{H}(1s) + H_2 \longrightarrow \underline{H}(3d) + H_2$	excitation	[18]	g)
20	$\sigma_{10_{tot}}$	$\underline{H}^+ + H_2 \longrightarrow \underline{H}(tot) + H_2^+$	charge exchange	[18]	h)
21	$\sigma_{10_{1s}}$	$\underline{H}^+ + H_2 \longrightarrow \underline{H}(1s) + H_2^+$	charge exchange	-	i)
22	$\sigma_{10_{2s}}$	$\underline{H}^+ + H_2 \longrightarrow \underline{H}(2s) + H_2^+$	charge exchange	[18]	-
23	$\sigma_{10_{2p}}$	$\underline{H}^+ + H_2 \longrightarrow \underline{H}(2p) + H_2^+$	charge exchange	[18]	-
24	$\sigma_{10_{3s}}$	$\underline{H}^+ + H_2 \longrightarrow \underline{H}(3s) + H_2^+$	charge exchange	[18]	-
25	$\sigma_{10_{3p}}$	$\underline{H}^+ + H_2 \longrightarrow \underline{H}(3p) + H_2^+$	charge exchange	[18]	-
26	$\sigma_{10_{3d}}$	$\underline{H}^+ + H_2 \longrightarrow \underline{H}(3d) + H_2^+$	charge exchange	[18]	-
27	σ_m	$\underline{e}^- + H_2 \longrightarrow \underline{e}^- + H_2$	momentum transfer	[18]	j)

Table 3.3: Beam species interaction included in the model

Comments to table 3.3:

a) $\sigma_{-10_{tot}}$ is the cumulative cross section for the single stripping process, namely $\sigma_{-10_{tot}} = \sigma_{-10_{1s}} + \sigma_{-10_{2s}} + \sigma_{-10_{2p}} + \sigma_{-10_{3s}} + \sigma_{-10_{3p}} + \sigma_{-10_{3d}}$;

b) Since not present in literature, $\sigma_{-10_{1s}}$ is found in the following way: $\sigma_{-10_{1s}} = \sigma_{-10_{tot}} - [\sigma_{-10_{2s}} + \sigma_{-10_{2p}} + \sigma_{-10_{3s}} + \sigma_{-10_{3p}} + \sigma_{-10_{3d}}]$;

c) Since $\sigma_{-10_{2s}}$, $\sigma_{-10_{2p}}$, $\sigma_{-10_{3s}}$, $\sigma_{-10_{3p}}$ and $\sigma_{-10_{3d}}$ are defined only in the interval 3-25 keV, their validity is arbitrarily extended up to 100 keV reproducing the same asymptotic behaviour of $\sigma_{-10_{tot}}$ at high energies;

d) Since in [19] only the cumulative cross section $\sigma_{-10_{3p+3d}}$ is reported, $\sigma_{-10_{3p}}$ is arbitrarily chosen to be 75% of $\sigma_{-10_{3p+3d}}$ while $\sigma_{-10_{3d}}$ the remaining 25%, namely $\sigma_{-10_{3p}} = 0.75 \cdot \sigma_{-10_{3p+3d}}$ and $\sigma_{-10_{3d}} = 0.25 \cdot \sigma_{-10_{3p+3d}}$;

e) Since $\sigma_{0_{2p}1}$, $\sigma_{0_{3s}1}$, $\sigma_{0_{3p}1}$ and $\sigma_{0_{3d}1}$ were not found in literature, they are arbitrarily chosen to be the same as $\sigma_{0_{2s}1}$;

f) $\sigma_{0_{1s}0_{2p}}$ is defined only up to 25 keV, it is arbitrarily extended to 100 keV;
g) Since $\sigma_{0_{1s}0_{3p}}$ and $\sigma_{0_{1s}0_{3d}}$ were not found separately, they were arbitrarily taken to be 75% and 25% respectively of the cumulative cross section $\sigma_{0_{1s}0_{3p+3d}}$, namely $\sigma_{0_{1s}0_{3p}} = 0.75 \cdot \sigma_{0_{1s}0_{3p+3d}}$ and $\sigma_{0_{1s}0_{3d}} = 0.25 \cdot \sigma_{0_{1s}0_{3p+3d}}$;
h) $\sigma_{10_{tot}}$ is the cumulative cross section for the charge exchange process, namely: $\sigma_{10_{tot}} = \sigma_{10_{1s}} + \sigma_{10_{2s}} + \sigma_{10_{2p}} + \sigma_{10_{3s}} + \sigma_{10_{3p}} + \sigma_{10_{3d}}$;
i) Since not present in literature, $\sigma_{10_{1s}}$ is found in the following way: $\sigma_{10_{tot}} - [\sigma_{10_{2s}} + \sigma_{10_{2p}} + \sigma_{10_{3s}} + \sigma_{10_{3p}} + \sigma_{10_{3d}}]$;
j) As in table 3.1, σ_m is represented by the elastic scattering cross section.

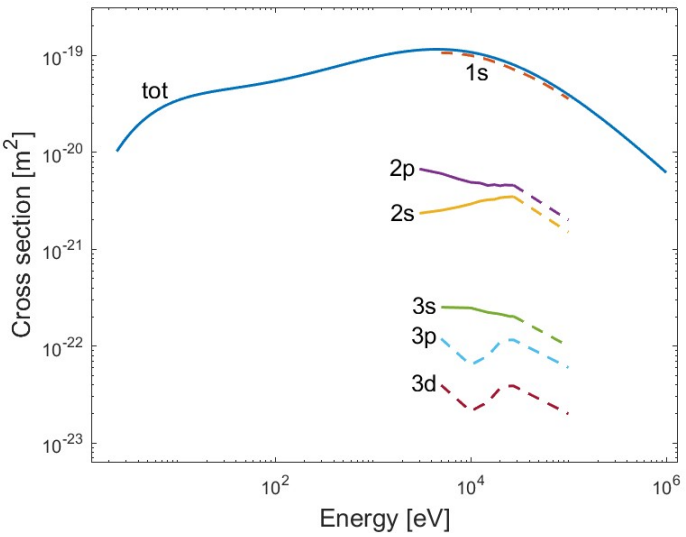

(a) Single stripping: $\underline{H}^- + H_2 \rightarrow \underline{H}(\ ) + \underline{e}^- + H_2$

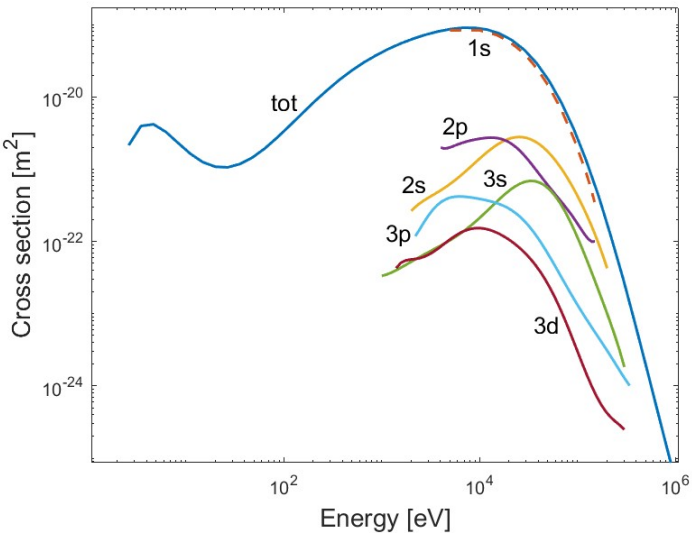

(b) Charge exchange: $\underline{H}^+ + H_2 \rightarrow \underline{H}(\ ) + H_2^+$

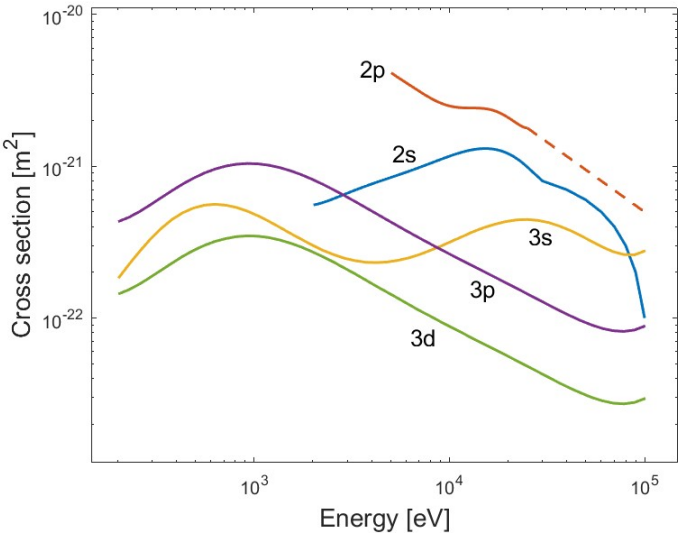

(c) Excitation: $\underline{H}(1s) + H_2 \rightarrow \underline{H}(\ ) + H_2$

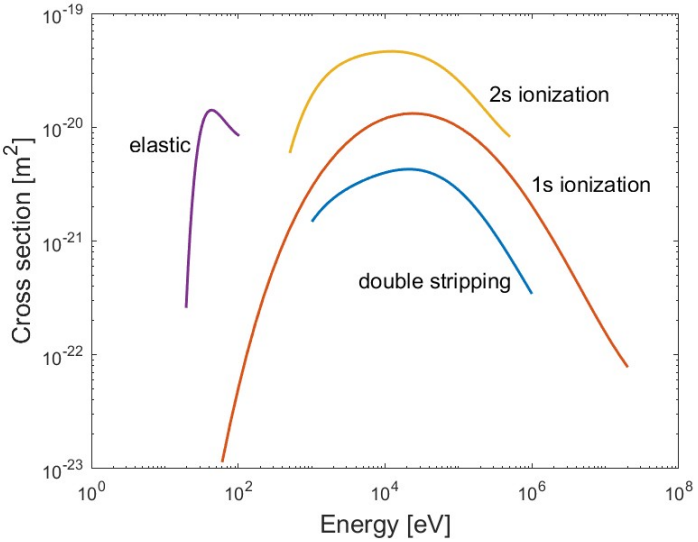

(d) Double stripping: $\underline{H}^- + H_2 \rightarrow \underline{H}^+ + 2\underline{e}^- + H_2$
Ionization: $\underline{H}(\ ) + H_2 \rightarrow \underline{H}^+ + \underline{e}^- + H_2$
Electron elastic collision: $\underline{e}^- + H_2 \rightarrow \underline{e}^- + H_2$

Figure 3.6: Cross sections adopted for the model

$$
\begin{cases}
\Gamma^{H^-}(i) = \Gamma^{H^-}(i-1) - \Gamma^{H^-}(i-1)\,(\sigma_{-10_{tot}} + \sigma_{-11})\,n_{H_2}\,dx \\
\Gamma^{H(1s)}(i) = \Gamma^{H(1s)}(i-1) + \Gamma^{H^-}(i-1)\,\sigma_{-10_{1s}}\,n_{H_2}\,dx + \Gamma^{H^+}(i-1)\,\sigma_{10_{1s}}\,n_{H_2}\,dx + \\
\qquad -\Gamma^{H(1s)}(i-1)\,(\sigma_{0_{1s}0_{2s}} + \sigma_{0_{1s}0_{2p}} + \sigma_{0_{1s}0_{3s}} + \sigma_{0_{1s}0_{3p}} + \sigma_{0_{1s}0_{3d}} + \sigma_{0_{1s}1})\,n_{H_2}\,dx + \\
\qquad +\Gamma^{H(2p)}(i-1)\left[1 - \exp\left(-\frac{dx}{v_b \cdot \tau_{2p\to 1s}}\right)\right] + \\
\qquad +\Gamma^{H(3p)}(i-1)\left[1 - \exp\left(-\frac{dx}{v_b \cdot \tau_{3p\to 1s}}\right)\right] br_{3p\to 1s} \\
\Gamma^{H(2s)}(i) = \Gamma^{H(2s)}(i-1) + \Gamma^{H^-}(i-1)\,\sigma_{-10_{2s}}\,n_{H_2}\,dx + \Gamma^{H^+}(i-1)\,\sigma_{10_{2s}}\,n_{H_2}\,dx + \\
\qquad +\Gamma^{H(1s)}(i-1)\,\sigma_{0_{1s}0_{2s}}\,n_{H_2}\,dx - \Gamma^{H(2s)}(i-1)\,\sigma_{0_{2s}1}\,n_{H_2}\,dx + \\
\qquad +\Gamma^{H(3p)}(i-1)\left[1 - \exp\left(-\frac{dx}{v_b \cdot \tau_{3p\to 2s}}\right)\right] br_{3p\to 2s} \\
\Gamma^{H(2p)}(i) = \Gamma^{H(2p)}(i-1)\,\exp\left(-\frac{dx}{v_b \cdot \tau_{2p\to 1s}}\right) + \\
\qquad +\Gamma^{H^-}(i-1)\,\sigma_{-10_{2p}}\,n_{H_2}\,dx + \Gamma^{H^+}(i-1)\,\sigma_{10_{2p}}\,n_{H_2}\,dx + \\
\qquad +\Gamma^{H(1s)}(i-1)\,\sigma_{0_{1s}0_{2p}}\,n_{H_2}\,dx - \Gamma^{H(2p)}(i-1)\,\sigma_{0_{2p}1}\,n_{H_2}\,dx + \\
\qquad +\Gamma^{H(3s)}(i-1)\left[1 - \exp\left(-\frac{dx}{v_b \cdot \tau_{3s\to 2p}}\right)\right] + \\
\qquad +\Gamma^{H(3d)}(i-1)\left[1 - \exp\left(-\frac{dx}{v_b \cdot \tau_{3d\to 2p}}\right)\right] \\
\Gamma^{H(3s)}(i) = \Gamma^{H(3s)}(i-1)\,\exp\left(-\frac{dx}{v_b \cdot \tau_{3s\to 2p}}\right) + \\
\qquad +\Gamma^{H^-}(i-1)\,\sigma_{-10_{3s}}\,n_{H_2}\,dx + \Gamma^{H^+}(i-1)\,\sigma_{10_{3s}}\,n_{H_2}\,dx + \\
\qquad +\Gamma^{H(1s)}(i-1)\,\sigma_{0_{1s}0_{3s}}\,n_{H_2}\,dx - \Gamma^{H(3s)}(i-1)\,\sigma_{0_{3s}1}\,n_{H_2}\,dx \\
\Gamma^{H(3p)}(i) = \Gamma^{H(3p)}(i-1)\left[\exp\left(-\frac{dx}{v_b \cdot \tau_{3p\to 2s}}\right) br_{3p\to 2s} + \exp\left(-\frac{dx}{v_b \cdot \tau_{3p\to 1s}}\right) br_{3p\to 1s}\right] + \\
\qquad +\Gamma^{H^-}(i-1)\,\sigma_{-10_{3p}}\,n_{H_2}\,dx + \Gamma^{H^+}(i-1)\,\sigma_{10_{3p}}\,n_{H_2}\,dx + \\
\qquad +\Gamma^{H(1s)}(i-1)\,\sigma_{0_{1s}0_{3p}}\,n_{H_2}\,dx - \Gamma^{H(3p)}(i-1)\,\sigma_{0_{3p}1}\,n_{H_2}\,dx \\
\Gamma^{H(3d)}(i) = \Gamma^{H(3d)}(i-1)\,\exp\left(-\frac{dx}{v_b \cdot \tau_{3d\to 2p}}\right) + \\
\qquad +\Gamma^{H^-}(i-1)\,\sigma_{-10_{3d}}\,n_{H_2}\,dx + \Gamma^{H^+}(i-1)\,\sigma_{10_{3d}}\,n_{H_2}\,dx + \\
\qquad +\Gamma^{H(1s)}(i-1)\,\sigma_{0_{1s}0_{3d}}\,n_{H_2}\,dx - \Gamma^{H(3d)}(i-1)\,\sigma_{0_{3d}1}\,n_{H_2}\,dx \\
\Gamma^{H^+}(i) = \Gamma^{H^+}(i-1) + \Gamma^{H^-}(i-1)\,\sigma_{-11}\,n_{H_2}\,dx + \Gamma^{H(1s)}(i-1)\,\sigma_{0_{1s}1}\,n_{H_2}\,dx + \\
\qquad +\Gamma^{H(2s)}(i-1)\,\sigma_{0_{2s}1}\,n_{H_2}\,dx + \Gamma^{H(2p)}(i-1)\,\sigma_{0_{2p}1}\,n_{H_2}\,dx + \\
\qquad +\Gamma^{H(3s)}(i-1)\,\sigma_{0_{3s}1}\,n_{H_2}\,dx + \Gamma^{H(3p)}(i-1)\,\sigma_{0_{3p}1}\,n_{H_2}\,dx + \\
\qquad +\Gamma^{H(3d)}(i-1)\,\sigma_{0_{3d}1}\,n_{H_2}\,dx - \Gamma^{H^+}(i-1)\,\sigma_{10_{tot}}\,n_{H_2}\,dx \\
\Gamma^{se}(i) = \Gamma^{se}(i-1) + \Gamma^{H^-}(i-1)\,[\sigma_{-10_{tot}} + 2\sigma_{-11}]\,n_{H_2}\,dx + \Gamma^{H(1s)}(i-1)\,\sigma_{0_{1s}1} n_{H_2}\,dx + \\
\qquad +\Gamma^{H(2s)}(i-1)\,\sigma_{0_{2s}1}\,n_{H_2}\,dx + \Gamma^{H(2p)}(i-1)\,\sigma_{0_{2p}1}\,n_{H_2}\,dx + \\
\qquad +\Gamma^{H(3s)}(i-1)\,\sigma_{0_{3s}1}\,n_{H_2}\,dx + \Gamma^{H(3p)}(i-1)\,\sigma_{0_{3p}1}\,n_{H_2}\,dx + \\
\qquad +\Gamma^{H(3d)}(i-1)\,\sigma_{0_{3d}1}\,n_{H_2}\,dx - \Gamma^{se}(i-1)\,\sigma_m\,n_{H_2}\,dx
\end{cases}
\tag{3.5}
$$

The first equation is exactly the same as 3.1 describing how the negative ion flux decreases by stripping and double stripping reactions. The other equations describe the evolution of ground and excited hydrogen atoms: the gain terms stems from stripping losses of negative ions and charge exchange interactions of positive ions, the loss term instead is due to ionization leading to the formation of positive ions; in addition, excited atoms may also decay emitting photons and thus decreasing their number, but at the same time increasing the population of lower atomic levels. The flux increase or decrease is described by the help of decreasing exponentials. In general, due to decayment, the fraction of flux $\Delta\Gamma^{H(k)}(i)$ of atoms populating the k energy level at the i-th position and decaying to the ℓ energy level is described by

$$\Delta\Gamma^{H(k)}(i) = \Gamma^{H(k)}(i-1)\left[1-\exp\left(-\frac{dt}{\tau_{k\to\ell}}\right)\right] = \Gamma^{H(k)}(i-1)\left[1-\exp\left(-\frac{dx}{v_b\,\tau_{k\to\ell}}\right)\right] \quad (3.6)$$

where $\Gamma^{H}(k)(i-1)$ is the flux of the decaying species at the previous step position, dt the time required by the beam to travel a step of length dx, v_b the beam velocity corresponding to $E_b = 48\,\mathrm{keV}$ and τ the characteristic time for the considered decayment process. Finally, the positive ion flux is increased by ionization of neutral atoms while reduced by positive ions undergoing charge exchange; concerning instead stripped electrons, the flux is increased by electrons detached from negative ions or neutral atoms and decreased by momentum transfer. The results showing the beam composition as a function of the distance travelled along the drift region are shown in figure 3.6

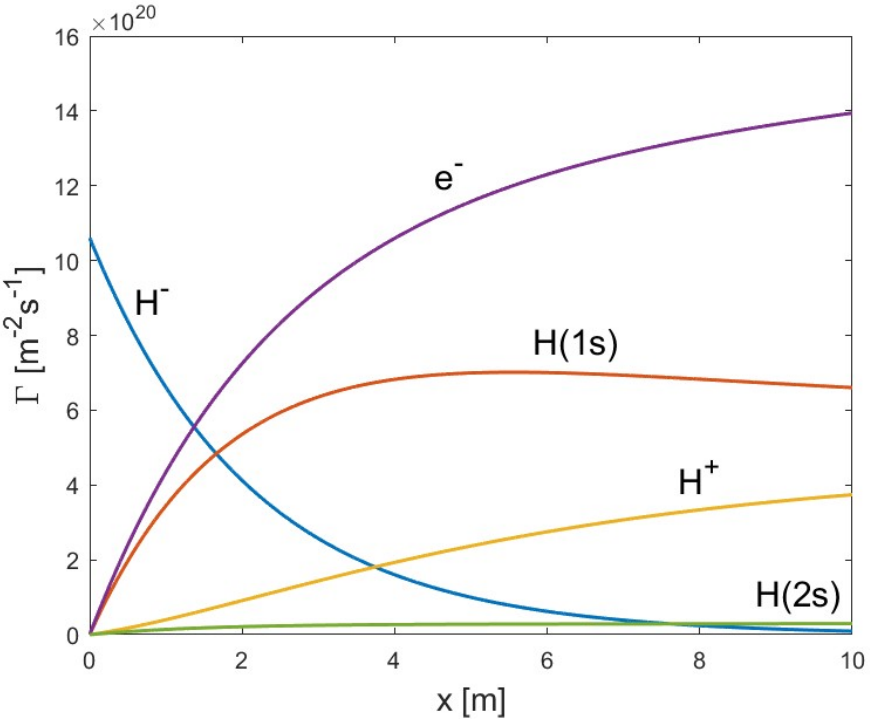

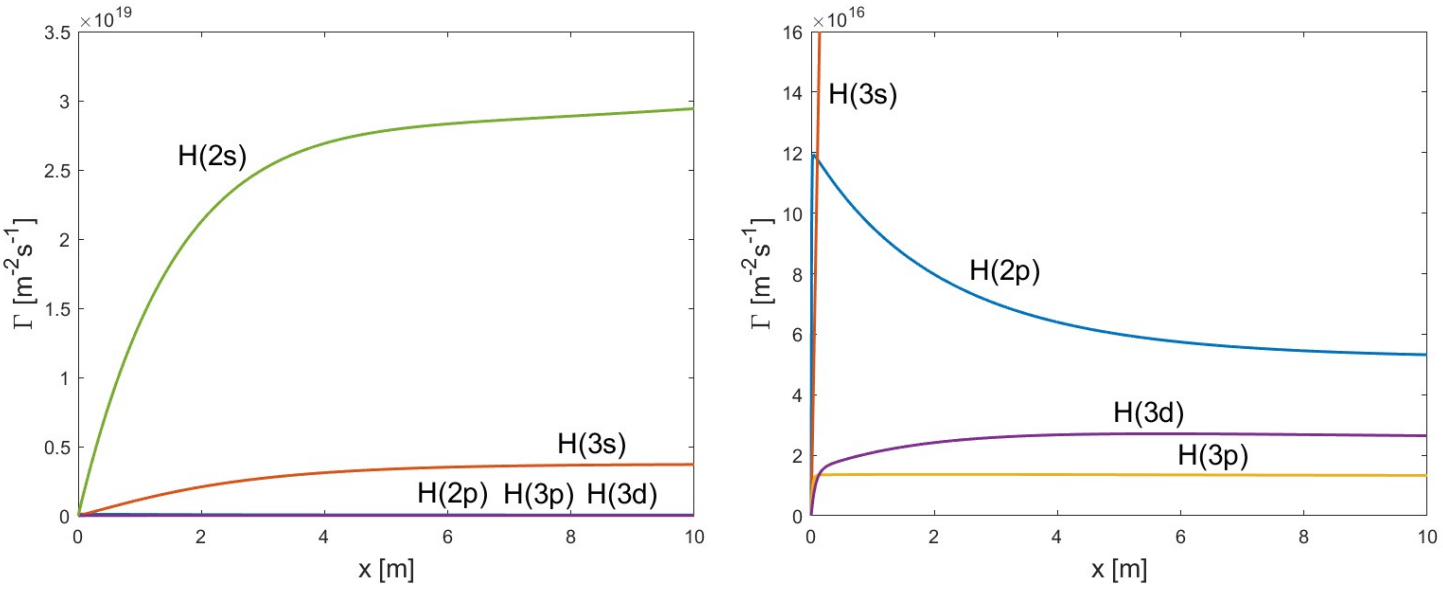

Figure 3.6: Beam composition. The upper panel shows the evolution of the beam species as a function of the distance travelled in the drift region. The lower panels depict the same quantities but zoomed since not visible in the upper panel

The two lower panels of figure 3.6 represent the profiles for the excited species. Among the factors influencing the excited atom fluxes, two are the most significant: the energy states towards which the atom is going to be excited and their characteristic decay lifetimes τ. Regarding the former, lower energy levels gets more easily populated since less energy is required to excite atoms to those states: in fact, as cross sections in figure 3.6 prove, 2s and 2p states will more easily get populated than 3s, 3p and 3d at 48 keV. On the other hand, for what concerns lifetimes, shorter lifetime states take lesser time to decay, so they will be more rapidly depopulated. The combination of these two factors helps justifying why, for example, the 3s flux of hydrogen atoms results to be larger than 2p: at first sight, by looking at the cross sections of figure 3.6, one may expect the 2p flux to be larger since more populated, the 3s state ($\tau_{3s\to 2p} = 316$ ns) takes on average two orders of magnitude more time than the 2p state to decay ($\tau_{2p\to 1s} = 1.6$ ns), hence this is the reason why the 3s flux is larger than 2p. A similar reasoning can also be applied to other excited atom species: for instance, the 2s state features the largest population among all the excited species since 2s is the lowest atomic excited level and the only possible transition to the 1s state is not allowed by selection rules.
To conclude, it only remains to compare the beam composition before and after including the possibility for atom species to be excited and emit light. Figure 3.7 shows that the fluxes of stripped electrons, negative and positive ions remain more or less the same, while the flux of neutral atoms H in the left panel is split in its ground H(1s) and excited state fluxes H(2s), H(2p), H(3s), H(3p), H(3d) such that the sum of them yields exactly H.

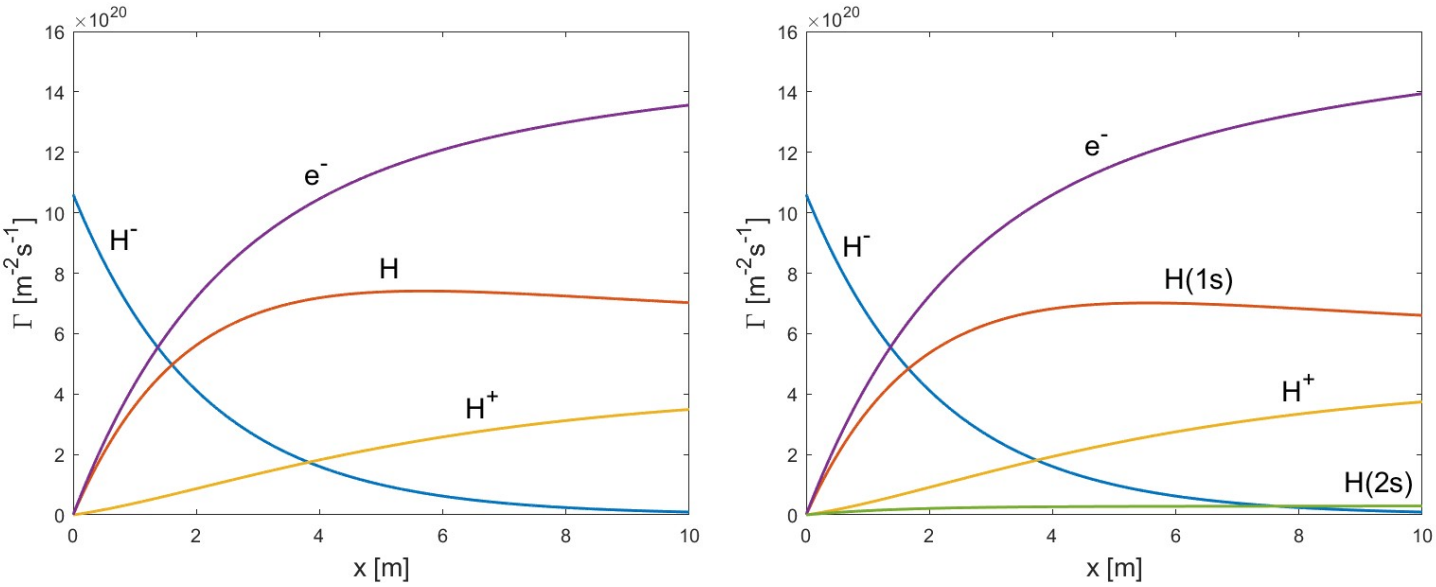

(a) H excited states not included

(b) H excited states included

Figure 3.7: Beam composition before and after including excited species and light emission

3.4 Light volumetric emission rates

From the results of the previous section it is possible to determine the photon emission rates. In particular, three are the contributions that can be estimated thanks to the results obtained with the previous 1D model: emission from fast excited beam atoms, emission by H_2 dissociative excitation induced by stripped electron impact and, finally, emission by H_2 dissociative excitation induced by ion or atom impact, as described in the following.

3.4.1 Emission from fast beam atoms

The L_α, L_β and B_α volumetric emission rates by de-excitation of fast beam atoms are described by way of the following equations:

$$\begin{cases} \left.\dfrac{dn}{dt}\right|_{L_\alpha}(i) = \dfrac{\Gamma^{H(2p)}(i-1)}{dx}\left[1-\exp\left(-\dfrac{dx}{v_b\cdot\tau_{2p\to1s}}\right)\right] \\ \left.\dfrac{dn}{dt}\right|_{B_\alpha}(i) = \dfrac{\Gamma^{H(3s)}(i-1)}{dx}\left[1-\exp\left(-\dfrac{dx}{v_b\cdot\tau_{3s\to2p}}\right)\right] + \\ \qquad + \dfrac{\Gamma^{H(3p)}(i-1)}{dx}\left[1-\exp\left(-\dfrac{dx}{v_b\cdot\tau_{3p\to2s}}\right)\right] br_{3p\to2s} + \\ \qquad + \dfrac{\Gamma^{H(3d)}(i-1)}{dx}\left[1-\exp\left(-\dfrac{dx}{v_b\cdot\tau_{3d\to2p}}\right)\right] \\ \left.\dfrac{dn}{dt}\right|_{L_\beta}(i) = \dfrac{\Gamma^{H(3p)}(i-1)}{dx}\left[1-\exp\left(-\dfrac{dx}{v_b\cdot\tau_{3p\to1s}}\right)\right] br_{3p\to1s} \end{cases} \tag{3.7}$$

where the emission rate at the i-th step is determined by the particle flux at the previous (i-1)-th position multiplied by the exponential argument inside the square brackets that quantifies the fraction of flux lost by decayment to a lower atomic state during the time taken by the beam to travel a step dx along the drift region. Moreover, while the B_α rate features three different contributions, one for each of the n=3 excited states, L_α and L_β have one only.

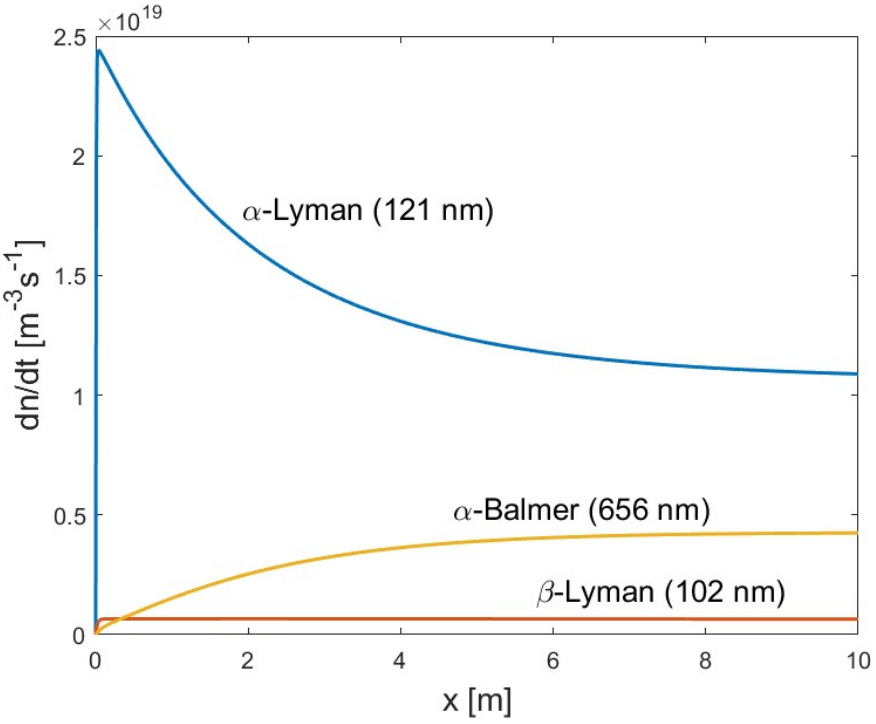

Figure 3.8: Volumetric emission rates by fast beam excited atoms

Figure 3.8 shows the results of the numerical simulation expressed as a function of the distance x travelled by the beam along the drift region. The largest contribution to light emission stems from L_α, featuring a initial step rise and then a slower decrease. The second largest contribution is from B_α followed by L_β. Two are the factors determining the rates of figure 3.8: the particle fluxes of the decaying atom species and their lifetimes. Concerning the former, larger atom fluxes imply larger emission rates; whereas for the latter, shorter lifetimes induce a larger emission for the considered transition. For example, the 2p state features both the smaller lifetime $\tau_{2p\rightarrow 1s}$ and the largest flux (figure 3.6) compared to the n=3 states, as a consequence, the emission rate for the L_α proves to be the largest one. Similar considerations can be also made to justify the L_β and the B_α contributions.

3.4.2 Emission by H_2 dissociative excitation induced by stripped electron impact

In the interaction of the beam with the molecular gas, electrons can be stripped from negative ions or neutral atoms and, once detached, mostly move in the same direction

of the beam with energy $E_{se} \sim 26\,eV$ for 48 keV beams. In turn, stripped electrons can dissociate hydrogen molecules producing excited atoms. This kind of interaction is commonly known as dissociative excitation by electron impact and its contribution to light emission is investigated in this section. The reactions exploited to find the rates can be found in table 3.4 along with their cross sections in figure 3.9.

#	σ	reaction	name	ref.	comment
1	σ_{2p}	$\underline{e}^- + H_2 \longrightarrow \underline{e}^- + H(2s) + H(2p)$	dissociative excitation	[20]	-
2	$\sigma_{n=3}$	$\underline{e}^- + H_2 \longrightarrow \underline{e}^- + H(1s) + H(n=3)$	dissociative excitation	[20]	a)
3	σ_{3s}	$\underline{e}^- + H_2 \longrightarrow \underline{e}^- + H(1s) + H(3s)$	dissociative excitation	-	b)
4	σ_{3p}	$\underline{e}^- + H_2 \longrightarrow \underline{e}^- + H(1s) + H(3p)$	dissociative excitation	-	b)
5	σ_{3d}	$\underline{e}^- + H_2 \longrightarrow \underline{e}^- + H(1s) + H(3d)$	dissociative excitation	-	b)

Table 3.4: Dissociative excitation by electron impact on H_2

Comments to table 3.4:

a) $\sigma_{n=3}$ the cumulative cross section for the production of n=3 excited atoms by molecular hydrogen dissociation, namely $\sigma_{n=3} = \sigma_{3s} + \sigma_{3p} + \sigma_{3d}$;

b) Since not present in literature, σ_{3s}, σ_{3p} and σ_{3d} are arbitrarily chosen to be a third of the cumulative cross section $\sigma_{n=3}$, namely: $\sigma_{3s} = \sigma_{3p} = \sigma_{3d} = 0.33 \cdot \sigma_{n=3}$ so as to have $\sigma_{n=3} = \sigma_{3s} + \sigma_{3p} + \sigma_{3d}$.

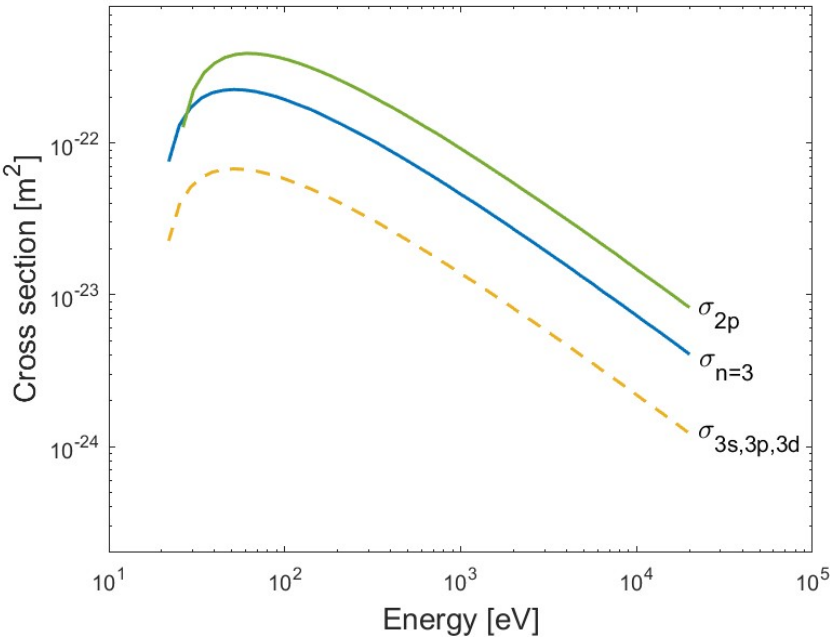

Figure 3.9: Dissociative excitation cross sections by electron impact on H_2

To investigate the emission rate induced by stripped electrons the following equations are exploited:

$$\begin{cases} \left.\frac{dn}{dt}\right|_{L_\alpha}(i) = \Gamma^{se}(i-1)\,\sigma_{2p}\,n_{H_2}\cdot\left[1-\exp\left(-\frac{dx}{v_b\cdot\tau_{2p\to1s}}\right)\right] \\ \left.\frac{dn}{dt}\right|_{B_\alpha}(i) = \Gamma^{se}(i-1)\,\sigma_{3s}\,n_{H_2}\cdot\left[1-\exp\left(-\frac{dx}{v_b\cdot\tau_{3s\to2p}}\right)\right]+ \\ \qquad +\Gamma^{se}(i-1)\,\sigma_{3p}\,n_{H_2}\cdot\left[1-\exp\left(-\frac{dx}{v_b\cdot\tau_{3p\to2s}}\right)\right]br_{3p\to2s}+ \\ \qquad +\Gamma^{se}(i-1)\,\sigma_{3d}\,n_{H_2}\cdot\left[1-\exp\left(-\frac{dx}{v_b\cdot\tau_{3d\to2p}}\right)\right] \\ \left.\frac{dn}{dt}\right|_{L_\beta}(i) = \Gamma^{se}(i-1)\,\sigma_{3p}\,n_{H_2}\cdot\left[1-\exp\left(-\frac{dx}{v_b\cdot\tau_{3p\to1s}}\right)\right]br_{3p\to1s} \end{cases} \tag{3.8}$$

where the emission rates at the i-th position are determined as a sum of different contributions, one for each possible atom transition from H(k) to H(ℓ) responsible for the L_α L_β or B_α emission; as an example, B_α is produced in the transition from H(n=3) to H(n=2), thus three are the possible contributions: H(k=3s)→H(ℓ=2p), H(k=3p)→H(ℓ=2s) and H(k=3d)→H(ℓ=2p). In general, each one of the additive contributions in 3.4.2 assumes the following shape:

$$\begin{aligned} \left.\frac{dn}{dt}\right|_{H(k)\to H(\ell)}(i) &= \frac{dn_{H(k)}}{dt}(i)\cdot\left[1-\exp\left(-\frac{dx}{v_b\cdot\tau_{k\to\ell}}\right)\right] = \\ &= \Gamma^{se}(i-1)\,\sigma_k\,n_{H_2}\cdot\left[1-\exp\left(-\frac{dx}{v_b\cdot\tau_{k\to\ell}}\right)\right] \end{aligned} \tag{3.9}$$

The quantity before the multiplication dot represents the rate of dissociated atoms produced in the k state at the i-th step by stripped electron impact on H_2; whereas, the term inside the squared brackets quantifies the fraction of atoms H(k) decaying to H(ℓ) during the time taken by the 100 keV beamlet to travel a distance dx along the drift region.

Figure 3.10 shows the emission rates as a function of the distance travelled in the drift region. Even in this case, L_α emission prevails over L_β and B_α, but the emission rates are at least two orders of magnitude smaller than those obtained in the previous section from fast excited beam atoms. According to equation 3.10, two factors determine the behaviour of the emission profile: the dissociative excitation cross section σ_k that is computed at the stripped electron energy E_{se} and the lifetime $\tau_{k\to\ell}$ characterizing the decay from the initial k to the final ℓ atomic state. In particular, the emission is favoured by large cross sections and small lifetimes. For example, σ_{2p} is larger than $\sigma_{n=3}$ and $\tau_{2p\to1s}$ much smaller compared to $\tau_{n=3\to n=2}$: this implies that the production of dissociated atoms in the 2p state is favoured and that their transition to the 1s state generates a larger number of photons per unit time than any other longer lifetime transition; both these factors justify why the L_α profile appears to be larger than all the others. Similar considerations can also be applied to explain L_β and B_α profiles.

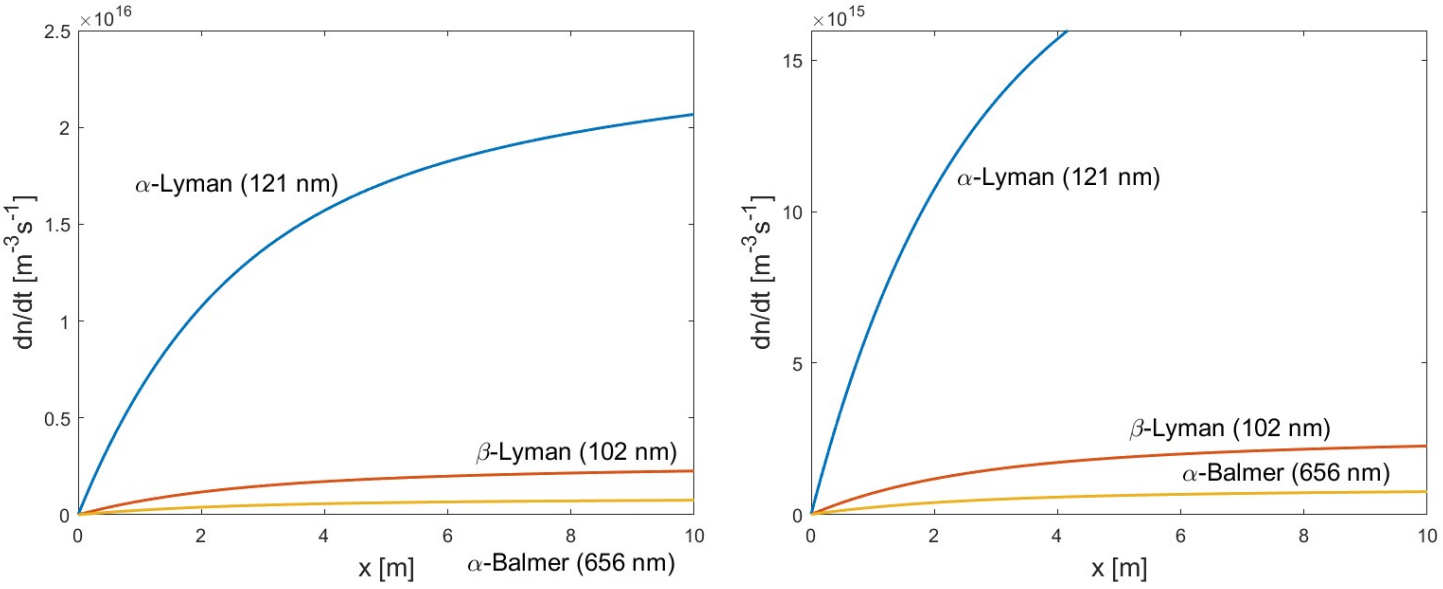

Figure 3.10: Volumetric emission rates by electron-driven dissociative excitation. The figure in the left panel is the same as the right one but zoomed on L_β and B_α.

3.4.3 Emission by H_2 dissociative excitation induced by beam atom or ion impact

The last contribution to line emission that can be estimated by the help of this 1D model is ion-driven H_2 dissociative excitation.
The exploited interactions are reported in table 3.5 along with their cross sections in figure 3.11.

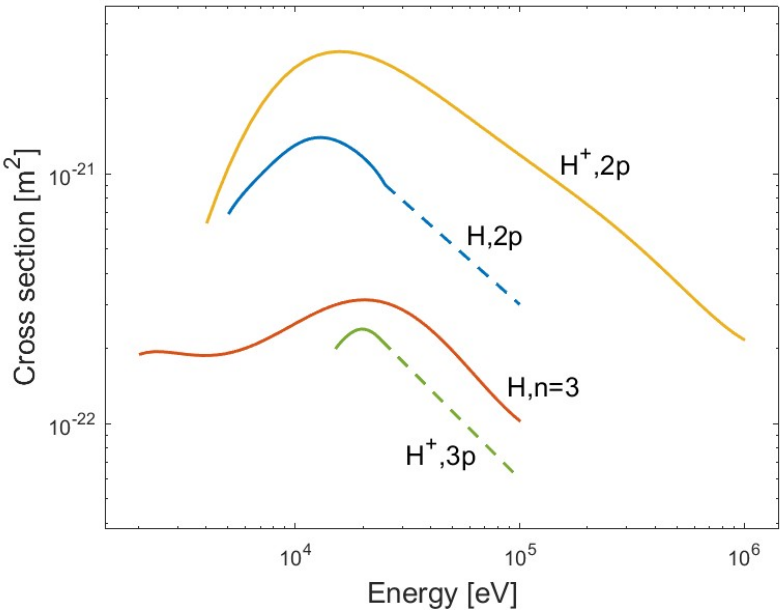

Figure 3.11: Dissociative excitation cross sections by atom or ion impact on H_2

#	σ	reaction	name	ref.	comment
1	$\sigma_{H,2p}$	$\underline{H} + H_2 \longrightarrow \underline{H} + H(2p) + H$	dissociative excitation	[18]	-
2	$\sigma_{H,n=3}$	$\underline{H} + H_2 \longrightarrow \underline{H} + H(n=3) + H$	dissociative excitation	[18]	a)
3	$\sigma_{H,3s}$	$\underline{H} + H_2 \longrightarrow \underline{H} + H(3s) + H$	dissociative excitation	-	b)
4	$\sigma_{H,3p}$	$\underline{H} + H_2 \longrightarrow \underline{H} + H(3p) + H$	dissociative excitation	-	b)
5	$\sigma_{H,3d}$	$\underline{H} + H_2 \longrightarrow \underline{H} + H(3d) + H$	dissociative excitation	-	b)
6	$\sigma_{H^+,2p}$	$\underline{H^+} + H_2 \longrightarrow \underline{H^+} + H(2p) + H$	dissociative excitation	[18]	-
7	$\sigma_{H^+,3s}$	$\underline{H^+} + H_2 \longrightarrow \underline{H^+} + H(3s) + H$	dissociative excitation	-	c)
8	$\sigma_{H^+,3p}$	$\underline{H^+} + H_2 \longrightarrow \underline{H^+} + H(3p) + H$	dissociative excitation	[18]	d)
9	$\sigma_{H^+,3d}$	$\underline{H^+} + H_2 \longrightarrow \underline{H^+} + H(3d) + H$	dissociative excitation	-	c)
10	$\sigma_{H^-,2p}$	$\underline{H^-} + H_2 \longrightarrow \underline{H^-} + H(2p) + H$	dissociative excitation	-	e)
11	$\sigma_{H^-,3s}$	$\underline{H^-} + H_2 \longrightarrow \underline{H^-} + H(3s) + H$	dissociative excitation	-	e)
12	$\sigma_{H^-,3p}$	$\underline{H^-} + H_2 \longrightarrow \underline{H^-} + H(3p) + H$	dissociative excitation	-	e)
13	$\sigma_{H^-,3d}$	$\underline{H^-} + H_2 \longrightarrow \underline{H^-} + H(3d) + H$	dissociative excitation	-	e)

Table 3.5: Dissociative excitation interactions by atom or ion impact on H_2

Comments to table 3.5:

a) $\sigma_{n=3}$ is the cumulative cross section for the production of n=3 excited atoms by dissociation of H_2, namely $\sigma_{H,n=3} = \sigma_{H,3s} + \sigma_{H,3p} + \sigma_{H,3d}$. Moreover, since not defined at energies larger than 20 keV, its validity is extended up to 100 keV as shown in figure 3.11 by way of a dashed line;

b) Since not present in literature, $\sigma_{H,3s}$, $\sigma_{H,3p}$ and $\sigma_{H,3d}$ are arbitrarily taken as a third of $\sigma_{n=3}$, namely $\sigma_{H,3s} = 0.33 \cdot \sigma_{H,n=3}$, $\sigma_{H,3p} = 0.33 \cdot \sigma_{H,n=3}$ and $\sigma_{H,3d} = 0.33 \cdot \sigma_{H,n=3}$ so as to have $\sigma_{H,n=3} = \sigma_{H,3s} + \sigma_{H,3p} + \sigma_{H,3d}$;

c) Since not present in literature, $\sigma_{H^+,3s}$ and $\sigma_{H^+,3d}$ are assumed to be the same as $\sigma_{H^+,3p}$, namely $\sigma_{H^+,3s} = \sigma_{H^+,3p} = \sigma_{H^+,3d}$;

d) Since not defined for energies higher than 20 keV, the cross section validity is arbitrarily extended up to 100 keV as shown in figure 3.11 by means of a dashed line.

e) Since $\sigma_{H^-,2p}$, $\sigma_{H^-,3s}$, $\sigma_{H^-,3p}$, $\sigma_{H^-,3d}$ are not present in literature, they are arbitrarily assumed to be the same as $\sigma_{H,2p}$, $\sigma_{H,3s}$, $\sigma_{H,3p}$, $\sigma_{H,3d}$ respectively, namely $\sigma_{H^-,2p} = \sigma_{H,2p}$, $\sigma_{H^-,3s} = \sigma_{H,3s}$, $\sigma_{H^-,3p} = \sigma_{H,3p}$ and finally $\sigma_{H^-,3d} = \sigma_{H,3d}$.

The following system of equations describes line emission ensuing from atom or ion-driven H_2 dissociative excitation:

$$\begin{cases} \left.\frac{dn}{dt}\right|_{L_\alpha}(i) = \frac{dn_{H(2p)}}{dt}(i)\cdot\left[1-\exp\left(-\frac{dx}{v_b\cdot\tau_{2p\to1s}}\right)\right] \\ \left.\frac{dn}{dt}\right|_{B_\alpha}(i) = \frac{dn_{H(3s)}}{dt}(i)\cdot\left[1-\exp\left(-\frac{dx}{v_b\cdot\tau_{3s\to2p}}\right)\right]+ \\ \qquad +\frac{dn_{H(3p)}}{dt}(i)\cdot\left[1-\exp\left(-\frac{dx}{v_b\cdot\tau_{3p\to2s}}\right)\right]br_{3p\to2s} \\ \qquad +\frac{dn_{H(3d)}}{dt}(i)\cdot\left[1-\exp\left(-\frac{dx}{v_b\cdot\tau_{3d\to2p}}\right)\right] \\ \left.\frac{dn}{dt}\right|_{L_\beta}(i) = \frac{dn_{H(3p)}}{dt}(i)\cdot\left[1-\exp\left(-\frac{dx}{v_b\cdot\tau_{3p\to1s}}\right)\right]br_{3p\to1s} \end{cases} \tag{3.10}$$

where the rates at which the excited species are populated are given by

$$\begin{cases} \frac{dn_{H(2p)}}{dt}(i) = \left[\Gamma^{H^-}(i-1)\,\sigma_{H^-,2p}+\Gamma^{H}(i-1)\,\sigma_{H,2p}+\Gamma^{H^+}(i-1)\,\sigma_{H^+,2p}\right]n_{H_2} \\ \frac{dn_{H(3s)}}{dt}(i) = \left[\Gamma^{H^-}(i-1)\,\sigma_{H^-,3s}+\Gamma^{H}(i-1)\,\sigma_{H,3s}+\Gamma^{H^+}(i-1)\,\sigma_{H^+,3s}\right]n_{H_2} \\ \frac{dn_{H(3p)}}{dt}(i) = \left[\Gamma^{H^-}(i-1)\,\sigma_{H^-,3p}+\Gamma^{H}(i-1)\,\sigma_{H,3p}+\Gamma^{H^+}(i-1)\,\sigma_{H^+,3p}\right]n_{H_2} \\ \frac{dn_{H(3d)}}{dt}(i) = \left[\Gamma^{H^-}(i-1)\,\sigma_{H^-,3d}+\Gamma^{H}(i-1)\,\sigma_{H,3d}+\Gamma^{H^+}(i-1)\,\sigma_{H^+,3d}\right]n_{H_2} \end{cases} \tag{3.11}$$

In general, each of the additive terms in 3.4.3 assumes the following shape:

$$\begin{aligned} \left.\frac{dn}{dt}\right|_{H(k)\to H(\ell)}(i) &= \frac{dn_{H(k)}}{dt}(i)\cdot\left[1-\exp\left(-\frac{dx}{v_b\cdot\tau_{k\to\ell}}\right)\right] = \\ &= \left[\Gamma^{H^-}(i-1)\,\sigma_{H^-,k}+\Gamma^{H}(i-1)\,\sigma_{H,k}+\Gamma^{H^+}(i-1)\,\sigma_{H^+,k}\right]n_{H_2}\cdot \\ &\qquad\cdot\left[1-\exp\left(-\frac{dx}{v_b\cdot\tau_{k\to\ell}}\right)\right] \end{aligned} \tag{3.12}$$

The quantity on the right-hand represents the production rate of dissociated atoms in the k state at the i-th step generated by beam atoms or ions impact on H_2 multiplied by the term inside the squared brackets quantifying the fraction of H(k) atoms decaying to H(ℓ) during the time taken by the 100 keV beamlet to travel a distance dx along the drift region.
Figure 3.10 shows the resulting emission rates as a function of the distance travelled by the beam in the drift region.

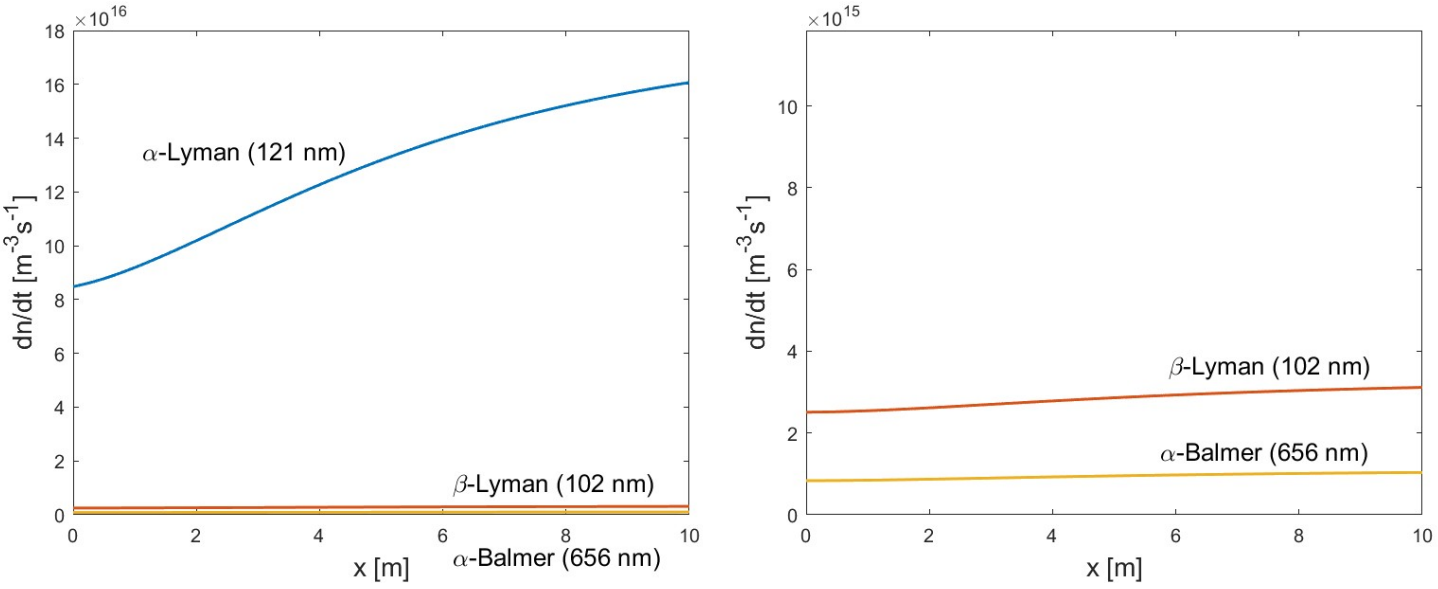

Figure 3.12: Volumetric emission rates by atom and ion-driven dissociative excitation. The figure in the left panel is the same as the right one but zoomed.

For the same reasons as stripped electron-driven dissociative excitation, L_α prevails over L_β and B_α. The emission rate profiles of figure 3.12 are still at least two order or magnitude smaller than those obtained from fast beam atoms and the difference with stripped electrons consists in the non-zero emission at x=0: this stems from the fact that at the entrance of the drift region the beam is fully composed of negative ions and thus, they can immediately induce target dissociation with formation of excited atoms and subsequent emission of light.

3.5 Conclusion of the chapter

According to this 1D model the emission from fast beam atoms is at least two orders of magnitude larger than electron, atom or ion driven dissociative excitation. However, this is not in agreement with the experimental results of the BES spectrum. In fact, the experimentally measured heights of the two peaks are comparable while, according to this model, the shifted peak should be much higher than the unshifted one. The reason of that may lie in the intrinsic limitations of this numerical simulation: in fact, only the evolution of beam particles like fast atoms, fast ions or stripped electrons along with the line emission they induce can be estimated. However, even dissociated atoms, cold plasma ions or electrons are produced during the interaction of the beam with the H_2 gas and their contribution to the emission of photons must be addressed. To comply with this task, more complex and more computationally demanding codes are needed; in fact, while in very first approximation it can be assumed that beam particles follow straight-line trajectories even when they undergo collisions, plasma particles randomly wander around the simulation domain, thus a much larger number of degrees of freedom and higher dimensional models are required, making the description much more complicated; this analysis will however be carried out in one of the following chapters by means of a

Particle-In-Cell code.
To conclude, despite lacking of information regarding the formation and evolution of the beam plasma, this model allowed to give an approximate idea on how the composition of the beam evolves while the latter propagates along the drift region and to prove that beam-induced emission is not sufficient to justify the height of the BES unshifted peak.

Chapter 4

Electron distributions

By looking at the tomography spectrum of figure 2.6, it can be observed that light is detected even in the space between one beamlet and the neighbouring ones; this suggests that there must be processes producing n=3 excited atoms where beamlets are not present. Since their mass is much lower than hydrogen atoms or ions, electrons are the most promising candidates to spread radially out of the beamlets and fill that region. Electrons can then dissociate H_2 producing n=3 excited atoms as follows

$$\underline{e}^- + H_2 \longrightarrow \underline{e}^- + H + H(n=3) \tag{4.1}$$

$$e^- + H_2 \longrightarrow e^- + H + H(n=3) \tag{4.2}$$

where the underscore labels fast beam particles, while its absence indicates slow plasma particles. Yet, according to their energy and origin, different types of electrons can be produced during the beam propagation. Four types of electrons will be discussed in this chapter that may give rise to excited atoms by target dissociation:

- Co-extracted electrons;
- Electrons stripped along the accelerator column;
- Electrons stripped along the drift region;
- Rudd ionization electrons.

Co-extracted electrons will be the first ones to be discussed.

4.1 Co-extracted electrons

Being negatively charged, electrons are co-extracted from the SPIDER source along with negative ions. Once extracted, they are deflected and dumped against the extraction grid. However, a very small amount of them may escape the dumping and be fully accelerated to energies up to 48 keV reached during the 2021 experimental campaign.

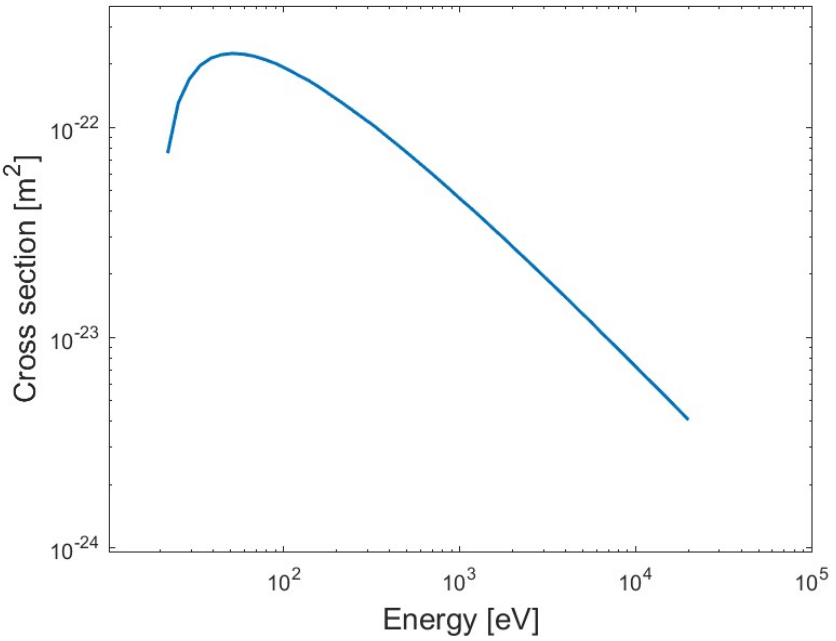

Figure 4.1: Dissociative excitation cross sections by electron impact on molecular hydrogen producing a n=3 hydrogen atom: $e^- + H_2 \longrightarrow e^- + H + H(n = 3)$

However, at 48 keV the electron-driven dissociative excitation cross sections in figure 4.1 is on the order of $\sigma \sim 10^{-23}\,\mathrm{m}^2$, hence too small to justify the luminous background in the tomography spectrum; consequently co-extracted electrons have been immediately set aside.

4.2 Electrons stripped along the accelerating column

Another possibility is to consider electrons detached from beam atoms or negative ions along the accelerator according to the following electron detachment reactions:

$$\underline{H}^- + H_2 \longrightarrow \underline{H} + \underline{e}^- + H_2 \tag{4.3}$$

$$\underline{H}^- + H_2 \longrightarrow \underline{H}^+ + 2\,\underline{e}^- + H_2 \tag{4.4}$$

$$\underline{H} + H_2 \longrightarrow \underline{H} + \underline{e}^- + H_2 \tag{4.5}$$

Even though pressure inside SPIDER accelerator is kept low to reduce as much as possible stripping losses of negative ions, some electrons may detach from beam atoms or negative ions and reach the drift region. The energy gain of stripped electrons once they reach the drift region depends upon their birth position along the accelerating column: the closer to the grounded grid, the lower their final energy. Typically, they reach energies on the order of 5-50 keV. However, as for co-extracted electrons, the dissociative excitation cross section in this energy interval is still too low to justify a significant B_α emission. Moreover, magnets embedded on the grounded grid deflect most of the electrons released along the accelerator onto the grid itself, preventing them from reaching the drift region. Thus, also electrons stripped along the accelerating column are ruled out from the following discussion.

4.3 Electrons stripped along the drift region

This section deals with electrons detached from beam atoms or negative ions along the drift region. Hence, to examine stripped electrons, a Montecarlo simulation written in MATLAB is performed aiming at investigating their radial spreading out of the beamlet. The domain of the simulation is assumed as a cylinder of length $L = 1\,\mathrm{m}$ along the x direction of propagation of the beam and radius $R_{vessel} = 2\,\mathrm{m}$, the latter to simulate SPIDER's vessel radial extension, but yet not relevant for the final result of the numerical investigation. Moreover, the cylinder is filled with molecular hydrogen at a pressure of $p = 0.03\,\mathrm{Pa}$.

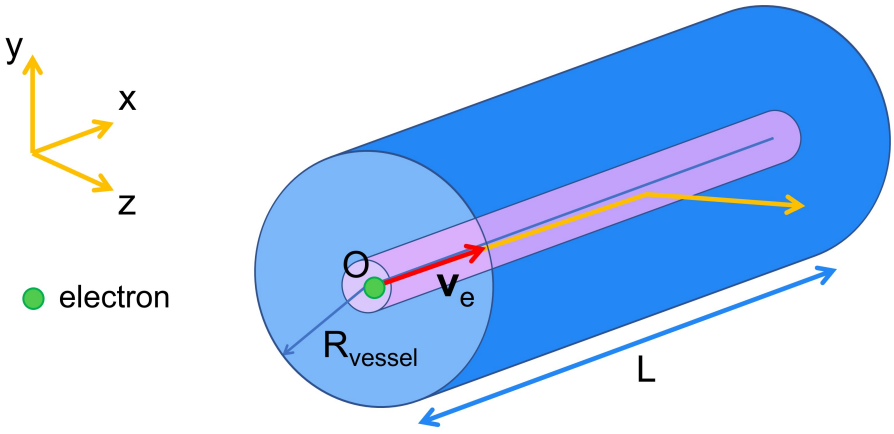

Figure 4.2: Simulation domain representing the propagation of one single beamlet along SPIDER's vessel. The figure displays one of the possible trajectories of an electron generated with velocity $\boldsymbol{v}_e$ during the interaction of the beamlet with the H_2 gas.

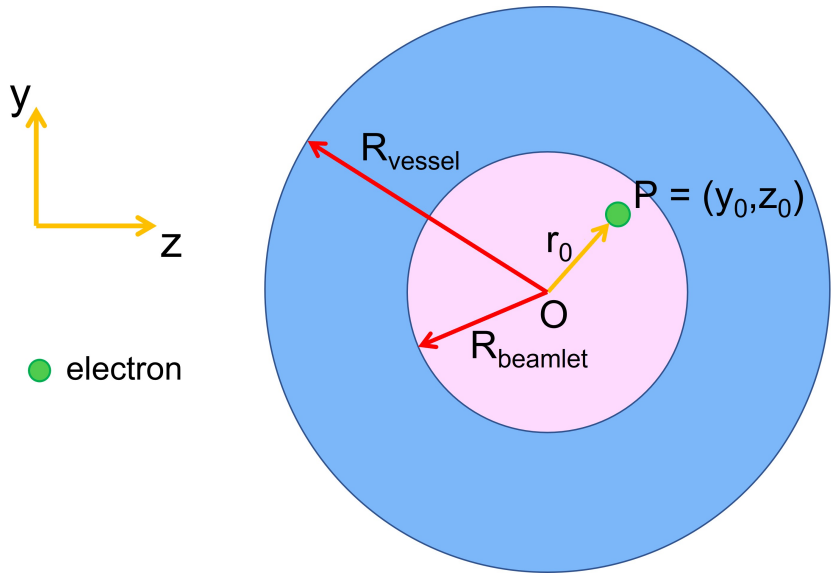

Figure 4.3: Transversal section of the simulation domain

For simplicity, the beamlet is approximated as a cylinder of radius $R_{beamlet} = 8\,\mathrm{mm}$ centred on the vessel axis and propagating along the x direction. In particular, this simulation

aims at determining the probability distribution of finding a stripped electron with energy E at a distance r from the beamlet axis. To comply with this task, one electron at a time is generated along the beamlet and propagates through the vessel until it reaches the domain boundaries, so that another electron can be generated. As a consequence of the cylindrical symmetry of the problem, there is no dependence on the x coordinate; therefore the problem can be simplified from 3D to 2D on the yz plane containing the point O as shown in figure 4.3. To start the numerical simulation, a stripped electron is generated with energy $E_{se} = 26\,\text{eV}$ in a generic random point $P = (y_0, z_0)$ inside the beamlet area of figure 4.3 according to a bi-dimensional gaussian distribution centred on the beamlet axis O and having a third of the beamlet radius as standard deviation. Concerning the electron velocity, the following formula is exploited

$$\boldsymbol{v_{se}} = \sqrt{\frac{2eE_{se}}{m_e}}\,\hat{\boldsymbol{v}}_{\boldsymbol{se}} = \sqrt{\frac{2eE_{se}}{m_e}}\,(\hat{v}_x, \hat{v}_y, \hat{v}_z) \tag{4.6}$$

where e is the elementary charge, m_e the electron mass and $\hat{\boldsymbol{v}}_{\boldsymbol{se}}$ the versor pointing at the direction at which the electron is emitted. To determine it, the angular distribution for stripped electron must be known. Yet, for 48 keV negative beams propagating in H_2 nothing was found in literature, only in [26] for 500 keV H^- in argon gas where it can be observed that stripped electrons are emitted at very small angles with respect to the beamlet direction, within few degrees. For that reason, in this model stripped electrons are chosen to be emitted in the same direction as the emitting atom or negative ion. Thus the components of the stripped electron velocity are only determined by the beamlet divergence $div = 10\,\text{mrad}$ as

$$\hat{v}_y = \hat{v}_{Hy} = N \cdot div \qquad \hat{v}_z = \hat{v}_{Hz} = N' \cdot div \qquad \hat{v}_x = \hat{v}_{Hx} = \sqrt{1 - (\hat{v}_y^2 + \hat{v}_z^2)} \tag{4.7}$$

where N and N′ are two normal distributed random numbers with mean 0 and 1 as standard deviation and $\hat{\boldsymbol{v}}_{\boldsymbol{H}} = (\hat{v}_{Hx}, \hat{v}_{Hy}, \hat{v}_{Hz})$ the versor indicating the moving direction of the particle impinging on H_2 as in figure 4.4. The transversal velocity components v_y and v_z are on purpose created small compared to v_x to reproduce the small angle emission of detached electrons with respect the beamlet axis direction. The angle ω at which the single electron is emitted with respect to the beamlet axis is thus found as

$$\omega = \arctan\left(\frac{\hat{v}_x}{\sqrt{\hat{v}_y^2 + \hat{v}_z^2}}\right) \tag{4.8}$$

To briefly summarize, an electron is generated in a random position P with velocity $\hat{\boldsymbol{v}}_{\boldsymbol{se}}$ and must propagate along the vessel filled with H_2 gas.

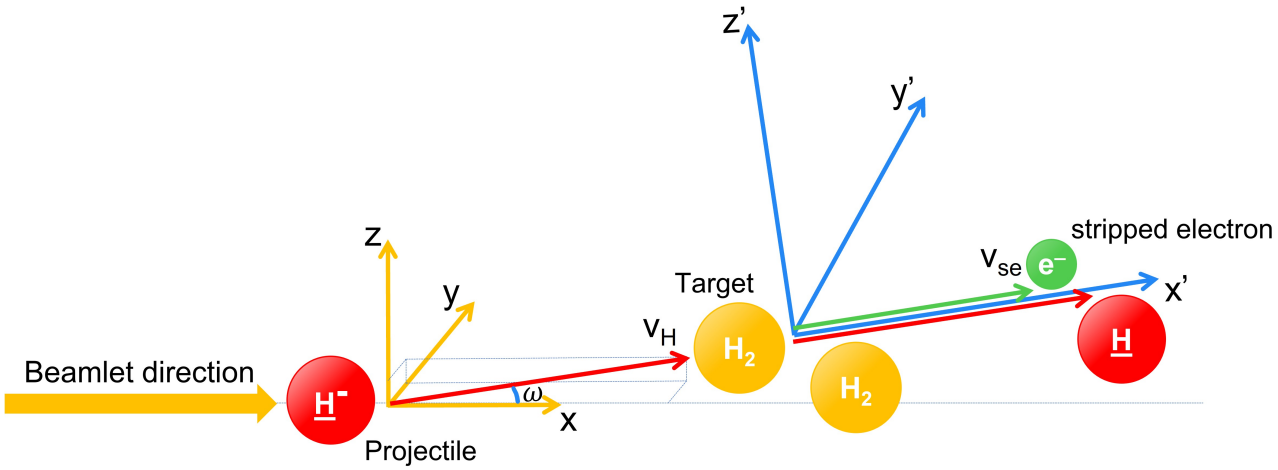

Figure 4.4: Example of process leading to the formation of stripped electrons.

To model the propagation, the timeline is divided in arbitrary small intervals dt. Once generated, the electron travels a step Δ proportional to the electron velocity v_{se} according the following relation

$$\Delta(E_{se}) = v_{se}(E_{se})\, dt = \sqrt{\frac{2eE_{se}}{m_e}}\, dt \tag{4.9}$$

After the electron makes the first step, it is necessary to determine whether it undergoes a collision or not. To this purpose, the total scattering cross section $\sigma(E_{se})$ by electron impact on H_2 is taken from [25] and shown in figure 4.5.

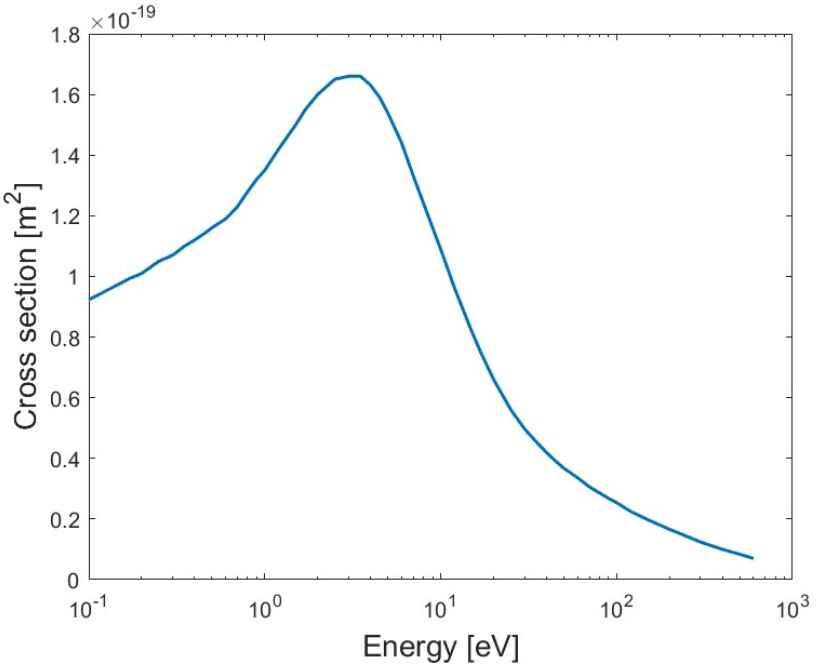

Figure 4.5: Total scattering cross section by electron impact on H_2 [25]

From the cross section it is possible to determine the mean free path $\lambda(E_{se})$ as

$$\lambda(E_{se}) = \frac{1}{\sigma(E_{se})\, n_{H_2}} \tag{4.10}$$

The probability $\Pr(E_{se})$ for the stripped electron to collide is thus given as

$$Pr(E_{se}) = 1 - \exp\left(-\frac{\Delta(E_{se})}{\lambda(E_{se})}\right) \in [0,1] \tag{4.11}$$

A random number δ is then drawn from a uniform distribution in the interval (0,1). For this Montecarlo simulation the reference frame of figure 4.6 is adopted to model the interaction with the H_2 gas:

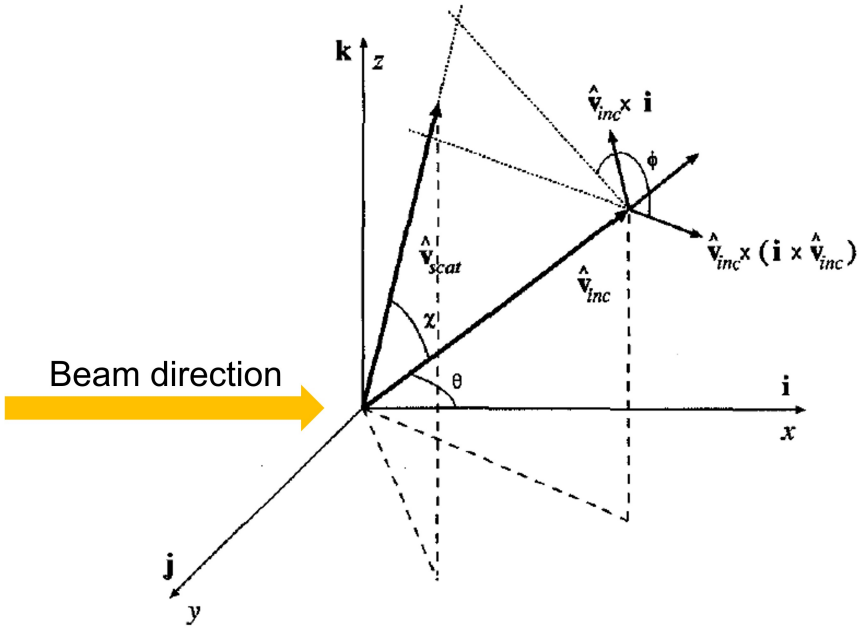

Figure 4.6: Reference frame adopted for the model [24]

where $\boldsymbol{v}_{inc}$ and $\boldsymbol{v}_{scat}$ denote the electron velocity before after making the step respectively; instead, $\hat{\boldsymbol{v}}_{inc}$ and $\hat{\boldsymbol{v}}_{scat}$ the corresponding versors.
Now two cases are possible according to figure 4.7.

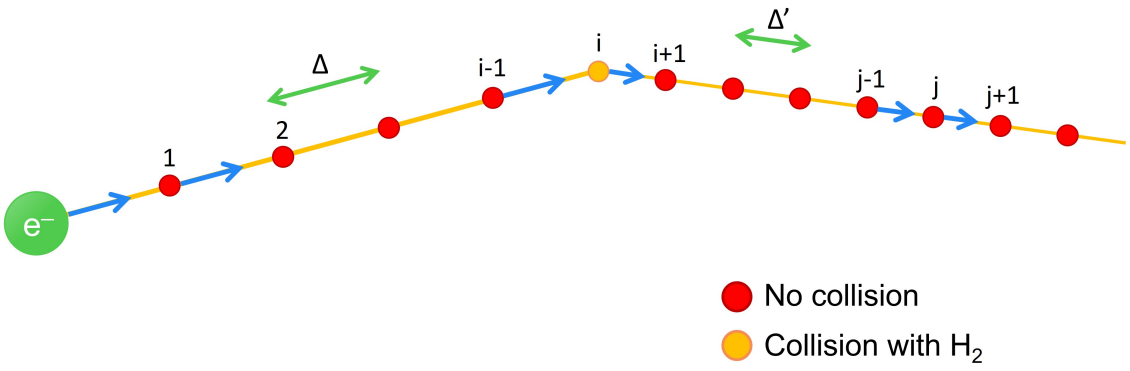

Figure 4.7: Discretization of the electron propagation

If $\delta > Pr(E_{se})$ no collision occurs, the electron does not change either direction or energy for the following step, hence:

$$\hat{\boldsymbol{v}}_{\boldsymbol{scat}} = \hat{\boldsymbol{v}}_{\boldsymbol{inc}} \qquad E_{scat} = E_{inc} \tag{4.12}$$

If instead $\delta \leq Pr(E_{se})$, the electron undergoes a collision where its energy and direction of motion are modified. The collision is modelled as in Vahedi [24], with the new reference frame determined by the following equations

$$\begin{cases} \boldsymbol{i'} = \hat{\boldsymbol{v}}_{inc} \\ \boldsymbol{j'} = \hat{\boldsymbol{v}}_{inc} \times \boldsymbol{i} \\ \boldsymbol{k'} = \hat{\boldsymbol{v}}_{inc} \times (\boldsymbol{i} \times \hat{\boldsymbol{v}}_{inc}) \end{cases} \tag{4.13}$$

According to [24], the velocity direction of the scattered electron is found as:

$$\hat{\boldsymbol{v}}_{scat} = \hat{\boldsymbol{v}}_{inc} \cos\chi + (\hat{\boldsymbol{v}}_{inc} \times \boldsymbol{i}) \frac{\sin\chi \sin\phi}{\sin\theta} + [\hat{\boldsymbol{v}}_{inc} \times (\boldsymbol{i} \times \hat{\boldsymbol{v}}_{inc})] \frac{\sin\chi \cos\phi}{\sin\theta} \tag{4.14}$$

with

$$\cos\theta = \hat{\boldsymbol{v}}_{inc} \cdot \boldsymbol{i} \qquad \cos\chi = \frac{2 + E_{inc} - 2(1 + E_{inc})^S}{E_{inc}} \qquad \phi = 2\pi S \tag{4.15}$$

where S is a random number drawn from a uniform distribution in the interval $(0, 1)$ [24]. It only remains to find the electron energy E_{scat} after the scattering:

$$E_{scat} = E_{inc} - \Delta E = E_{inc}\left[1 - \frac{2m_e}{M}(1 - \cos\chi)\right] \tag{4.16}$$

where m_e is the electron mass, M the molecular hydrogen mass, χ the scattering angle and ΔE the energy lost during the collision. This formula is taken from Vahedi [24] and represents the electron energy after a scattering event with a neutral atom. However, in this model the target is actually molecular and not atomic hydrogen. Nonetheless, this formula will anyway be exploited to model the electron-gas energy losses.
In both cases, the electron velocity vector becomes

$$\boldsymbol{v}_{\boldsymbol{scat}} = \sqrt{\frac{2eE_{scat}}{m_e}}\, \hat{\boldsymbol{v}}_{\boldsymbol{scat}} \tag{4.17}$$

Once $\boldsymbol{v}_{\boldsymbol{scat}}$ is determined, the electron makes another step and $\boldsymbol{v}_{\boldsymbol{scat}}$ becomes $\boldsymbol{v}_{\boldsymbol{inc}}$ for the new interaction. The electron continues this propagation process until it reaches the domain boundaries or its energy goes below a threshold arbitrarily fixed at 1 eV. At this point, another electron is generated and propagates through the vessel the same way. The simulation stops after reaching the number of electron to be processed. A detailed schematic of the simulation is shown in figure 4.8.

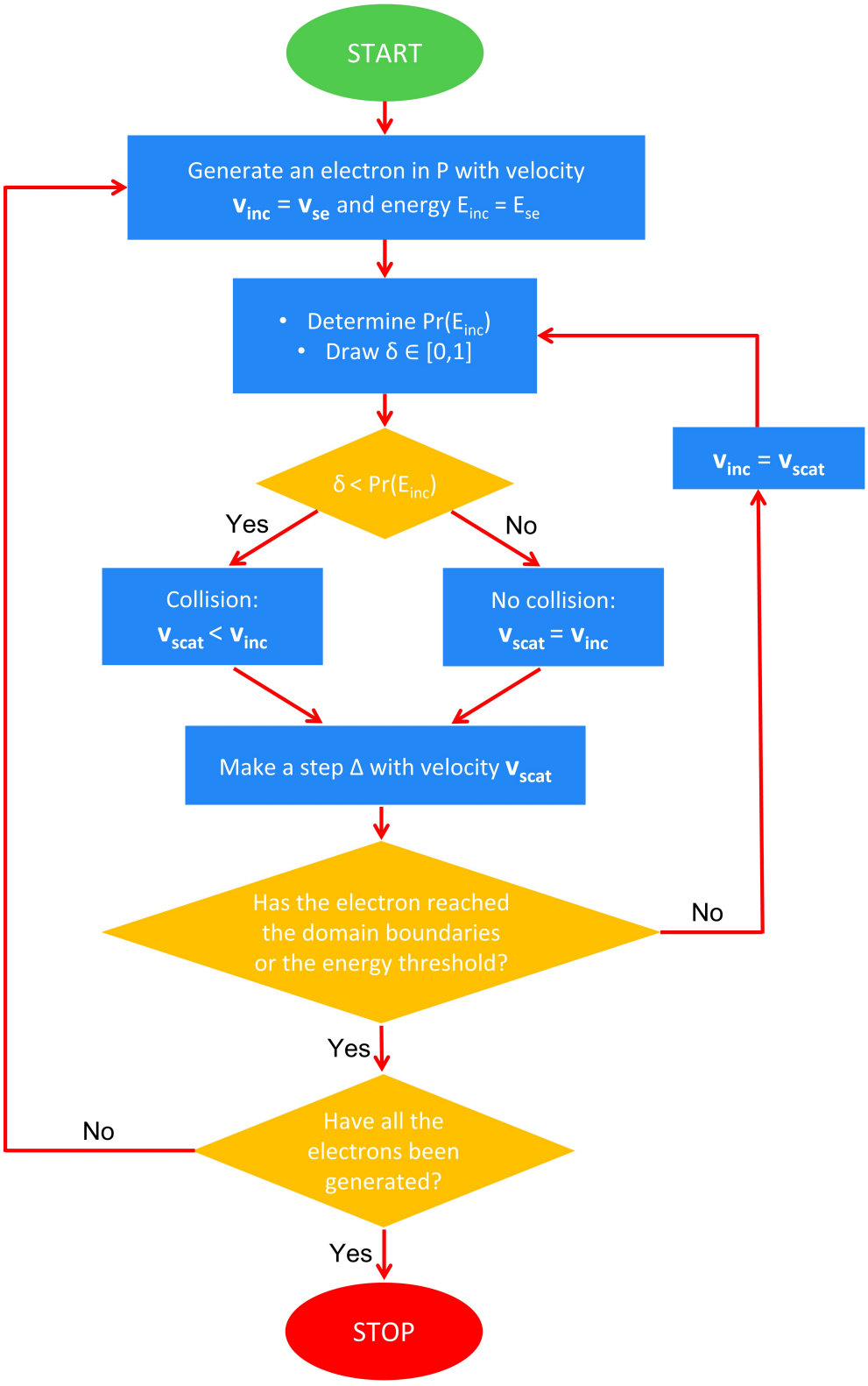

Figure 4.8: Stripped electron simulation scheme

To investigate the radial distribution of stripped electrons, for each step $\Delta(E)$ made by the simulated electrons, the radial distance r from the vessel axis and the electron energy E are registered as pairs (r,E) and put as entries in the 3D histogram of figure 4.9.

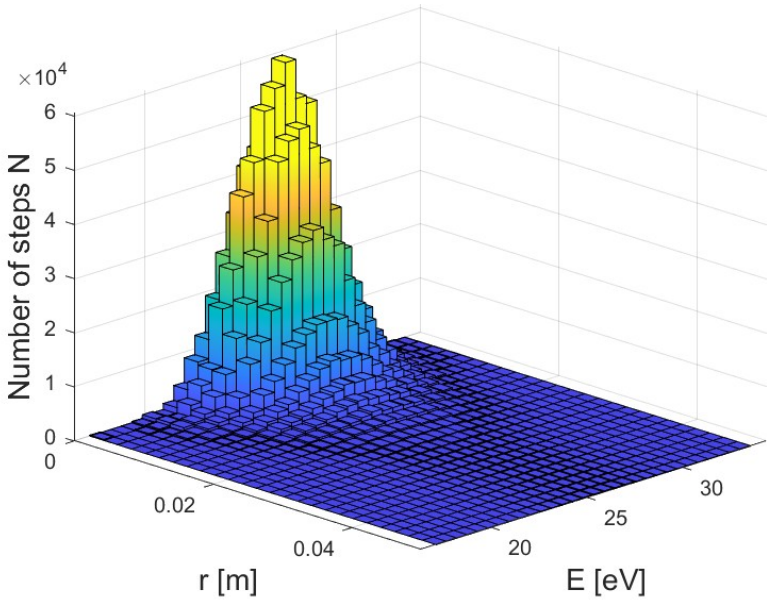

Figure 4.9: Energy and radial distribution for stripped electrons

Since each step always takes a fixed time dt to be travelled, the height of the bins in the histogram of figure 4.9 divided by the total number of electrons being fired yields the average time spent by an electron with energy E at a distance r from the beamlet axis.

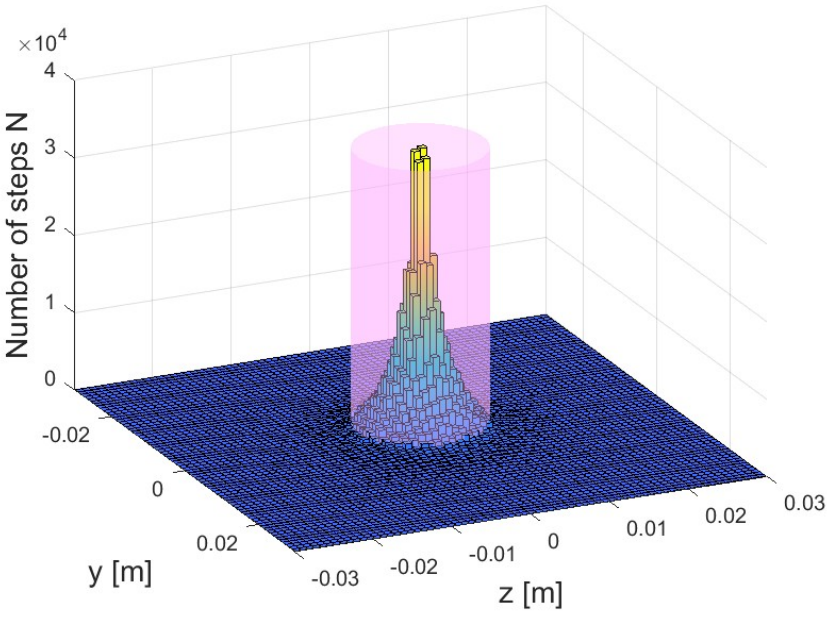

Figure 4.10: Spatial distribution of stripped electrons on the yz plane. The cylinder represents the beamlet area.

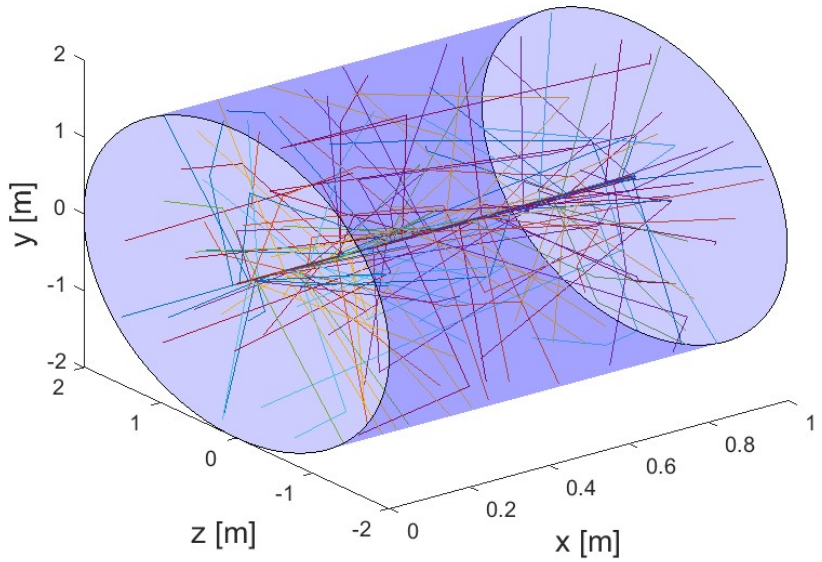

Figure 4.11: Trajectories of stripped electrons propagating along the vessel

Figures 4.9, 4.10 and 4.11 show that stripped electrons mostly remain in the vicinity of the beamlet axis: in fact, due to their small emission angle determined mostly by the intrinsic beamlet divergence and due to their large mean free path $\lambda \sim 2\,\mathrm{m}$, only 10% of the stripped electrons is deflected towards the domain boundaries, most of them instead go straight undeflected staying close to the beamlet axis.
However, due to their vicinity to the beamlet axis, stripped electrons are actually not able to justify the luminous background present in the beam tomography spectrum: in fact, according to figure 2.6, B_α radiation is produced even in the region between one beamlet and the others, but since stripped electrons remain close to the beamlet axis, they are not able to fill the space between the beamlets so as to justify the considerable B_α emission in those regions.

4.4 Rudd ionization electrons

Only Rudd electrons remain to be discussed, namely those produced by ionization of H_2 through the following processes [27]:

$$\underline{H}^- + H_2 \longrightarrow \underline{H}^- + H_2^+ + e^- \tag{4.18}$$

$$\underline{H} + H_2 \longrightarrow \underline{H} + H_2^+ + e^- \tag{4.19}$$

$$\underline{H}^+ + H_2 \longrightarrow \underline{H}^+ + H_2^+ + e^- \tag{4.20}$$

$$\underline{e}^- + H_2 \longrightarrow \underline{e}^- + H_2^+ + e^- \tag{4.21}$$

While stripped electrons are emitted with energy around 26 eV and angle ω only determined by the beamlet divergence, Rudd electrons are produced with specific angular and energy distributions given in [28] as double differential cross sections for molecular hydrogen ionization by 20-114 keV proton impact.

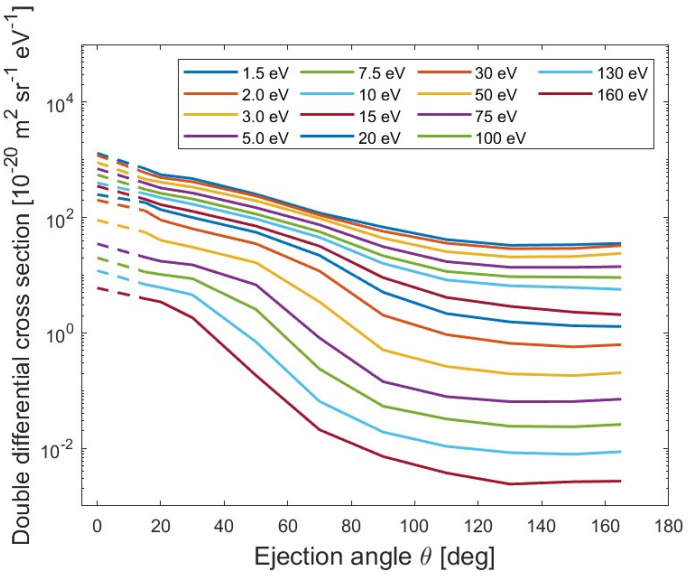

Figure 4.12: Double differential cross section by 48 keV proton impact on H_2 as a function of the ejection angle θ. The different colors in the legend represent the different energies at which ionization electrons are emitted. Finally, the dashed lines represent the artificial extension down to $\theta = 0°$.

However, double differential cross sections in [28] are not measured for ejection angles θ smaller than 15°. Nonetheless, they are arbitrarily extended down to small angles as shown with dashed lines in figure 4.12 where the double differential cross sections by 48 keV proton impact are plotted as a function of the ejection angle for different ejection energies W. The result is shown in figure 4.13: it can be observed that the surface representing the double differential cross section for 48 keV proton impact is peaked at small ejection angles θ and small ejection energies W.

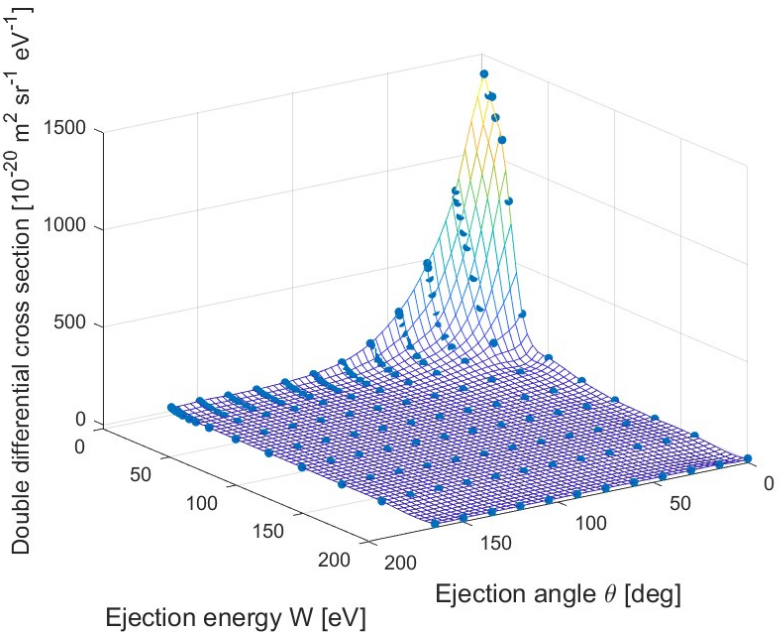

Figure 4.13: Double differential cross section by 48 keV proton impact [28]. Blue points are the experimental data while the surface connecting them is the interpolation result.

To start the numerical computation a Rudd ionization electron is generated according to the distribution of figure 4.13 with energy W and angle θ with respect to the direction of propagation of the beam particle impinging on the H_2 molecule in figure 4.14. Concerning the position in which the Rudd electron is generated, the procedure to find it is the same as in the previous section for stripped electrons.

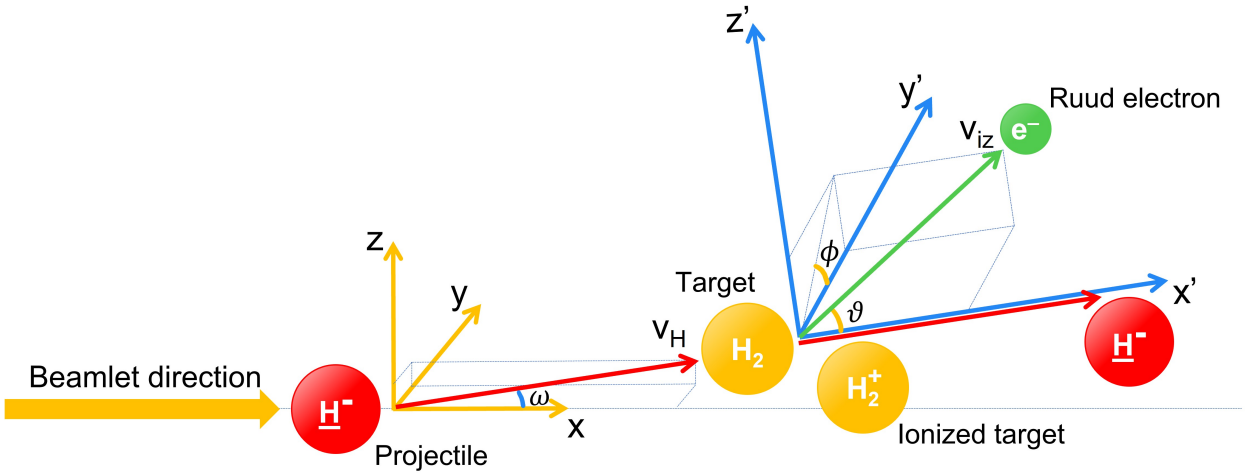

Figure 4.14: Example of process leading to the formation of Rudd ionization electrons.

The velocity vector of the Rudd electron is then determined in the $x'y'z'$ frame as

$$\boldsymbol{v'_{iz}} = \sqrt{\frac{2eW}{m_e}}\,\boldsymbol{\hat{v}'_{iz}} = \sqrt{\frac{2eW}{m_e}}\,(\hat{v}'_x, \hat{v}'_y, \hat{v}'_z) \tag{4.22}$$

where the components of the versor $\boldsymbol{\hat{v}'_{iz}}$ are given by

$$\hat{v}'_x = \cos\theta \qquad \hat{v}'_y = \sin\theta\,\cos\phi \qquad \hat{v}'_z = \sin\theta\,\sin\phi \tag{4.23}$$

and the $x'y'z'$ frame defined in the following way

$$\begin{cases} \boldsymbol{\hat{x}'} = \boldsymbol{\hat{v}}_H \\ \boldsymbol{\hat{y}'} = \boldsymbol{\hat{v}}_H \times \boldsymbol{\hat{x}} \\ \boldsymbol{\hat{z}'} = \boldsymbol{\hat{v}}_H \times (\boldsymbol{\hat{x}} \times \boldsymbol{\hat{v}}_H) \end{cases} \tag{4.24}$$

with the x' axis chosen in the same direction of the particle impinging on the H_2 molecule. As in the previous section for stripped electrons, the direction $\boldsymbol{\hat{v}_H} = (\hat{v}_{Hx}, \hat{v}_{Hy}, \hat{v}_{Hz})$ of the impinging particle atom or ion is determined by the beamlet divergence div as follows

$$\hat{v}_{Hy} = N \cdot div \qquad \hat{v}_{Hz} = N' \cdot div \qquad \hat{v}_{Hx} = \sqrt{1 - (\hat{v}^2_{Hy} + \hat{v}^2_{Hz})} \tag{4.25}$$

Thanks to the previous equations, the direction $\boldsymbol{\hat{v}_{iz}}$ of the Rudd electron in the xyz frame can be found as

$$\boldsymbol{v_{iz}} = \sqrt{\frac{2eW}{m_e}}\,(\boldsymbol{\hat{x}'}\cos\theta + \boldsymbol{\hat{y}'}\sin\theta\,\cos\phi + \boldsymbol{\hat{z}'}\sin\theta\,\sin\phi) \tag{4.26}$$

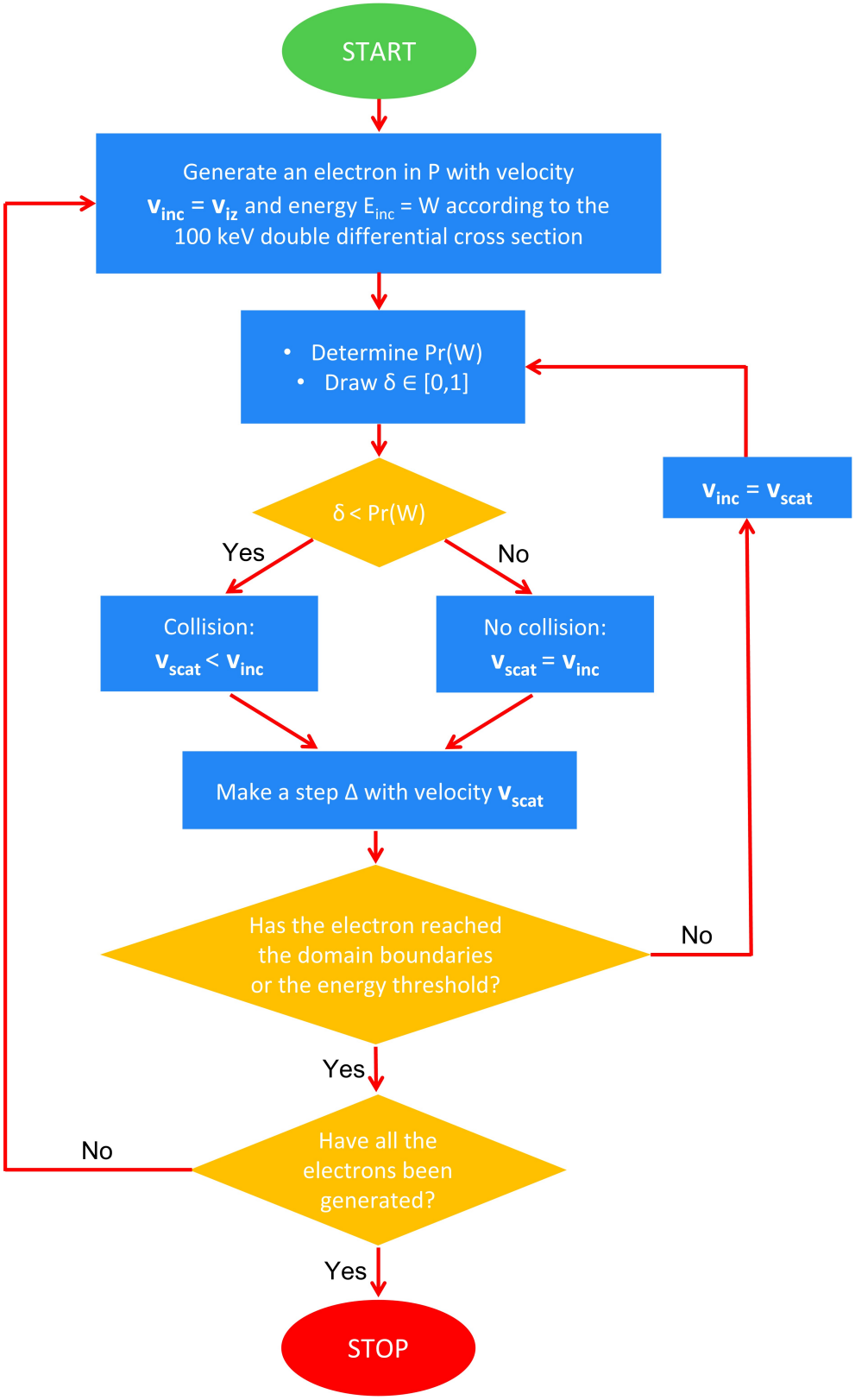

Figure 4.15: Rudd ionization electrons simulation scheme

Once the electron is generated, it propagates along the vessel the same way as stripped electrons in the previous section. To investigate the radial distribution of Rudd electrons, pairs (r,E) for each step Δ travelled by the electrons are put as entries of the 3D histogram of figure 4.16.

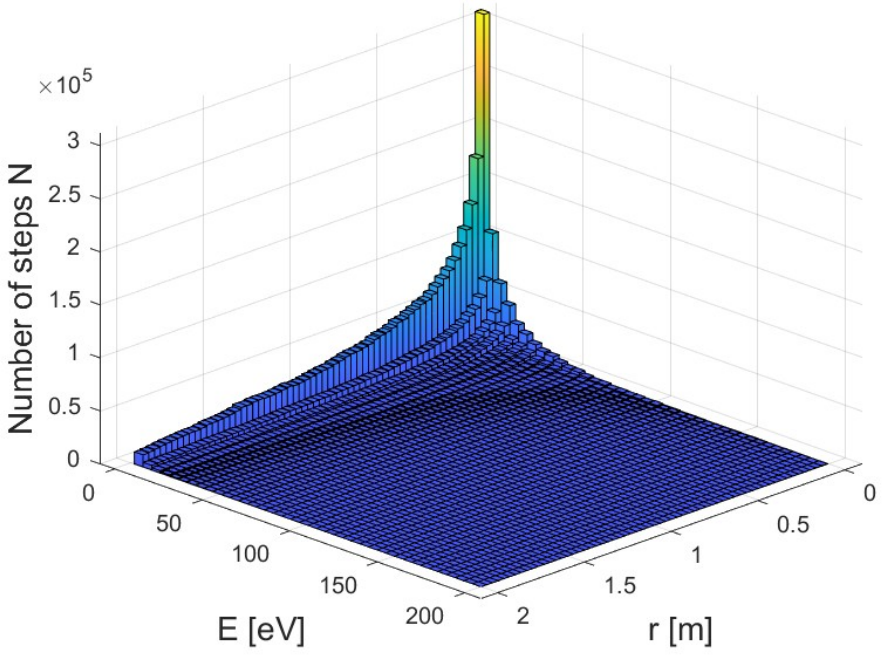

Figure 4.16: Energy and radial distribution for Rudd ionization electrons

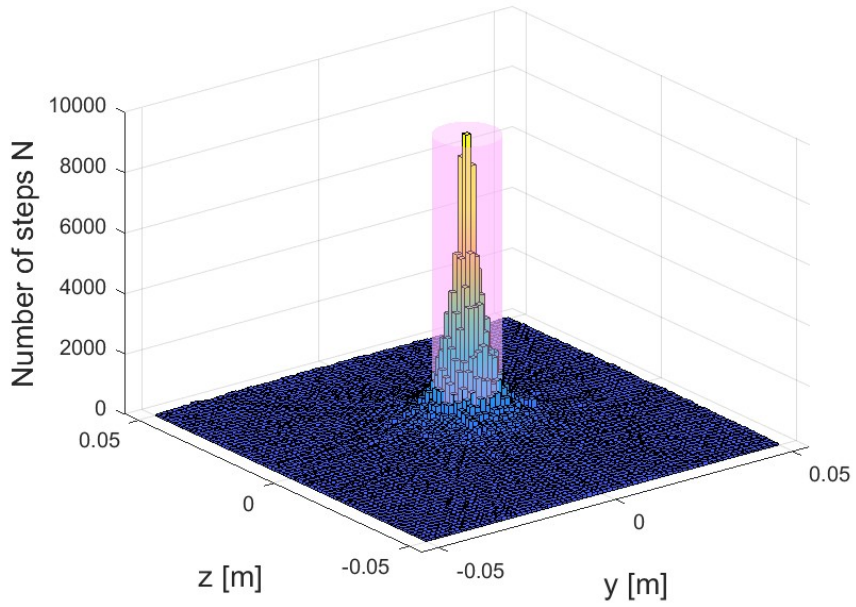

Figure 4.17: Spatial distribution of Rudd ionization electrons on the yz plane. The cylinder represents the beamlet area.

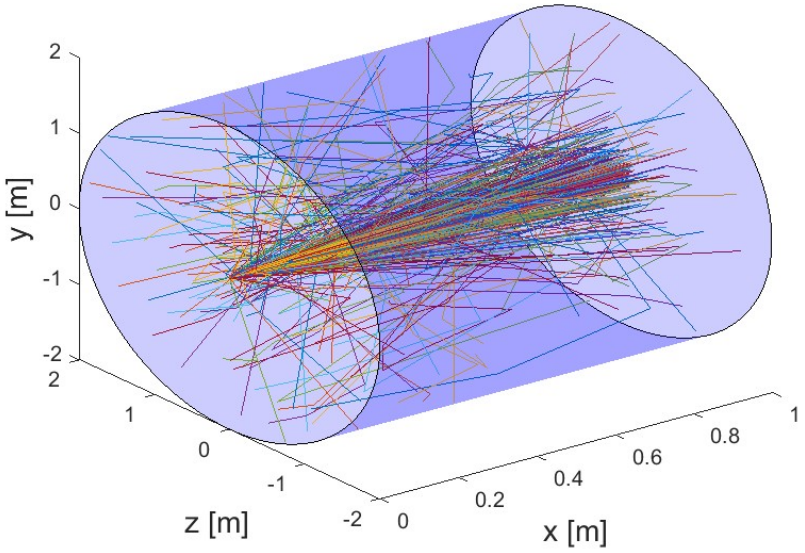

Figure 4.18: Trajectories of Rudd ionization electrons propagating along the vessel

The histograms of figures 4.16 and 4.17 show that, thanks to their angular emission, Rudd electrons can spread radially exiting the beamlet area. This is also proven by the image of figure 4.18 showing the trajectories of Rudd electrons along the vessel: in fact, while stripped electrons mostly go straight on along the beamlet axis, Rudd electrons are intrinsically emitted with the angular distribution of figure 4.13. Due to this fact, Rudd electrons spread out radially filling the space not occupied by the beamlet itself. These electrons can in turn produce n=3 excited atoms from the dissociation of the H_2 gas, justifying the emission of B_α radiation in the region between one beamlet and the others.

4.5 Histogram interpretation

As previously mentioned in the last two sections, the 3D histograms of figures 4.9 and 4.18 for stripped and Rudd electrons respectively are built inserting (r,E) pairs for each electron step Δ as histogram entries. As a consequence, the height of each bin represents the number of steps N(r,E) travelled by the electron with energy value within the histogram bin centred in E having width ΔE and distance from the beamlet axis belonging to the circular corona of figure 4.19 having radius r and width Δr. By properly rescaling the histogram for N(r,E) it is possible to find another histogram whose bin values $\nu(r, E)$ represent the average time per unit volume and unit spent by an electron at a distance r from the beamlet axis with energy E:

$$\nu_{strip}(r, E) = \frac{\tau_{strip}(r, E)}{2\pi r\, \Delta r_{strip}\, L\, \Delta E_{strip}} = \frac{N_{strip}(r, E)\, dt}{2\pi r\, \Delta r_{strip}\, L\, \Delta E_{strip}\, N_{electrons}} \tag{4.27}$$

$$\tau_{strip}(r, E) = \frac{N_{strip}(r, E)\, dt}{N_{electrons}} \tag{4.28}$$

where $\tau(r, E)$ is the average time spent by an electron at a distance r from the beamlet axis with energy E. Likewise for Rudd electrons

$$\nu_{Rudd}(r, E) = \frac{\tau_{Rudd}(r, E)}{2\pi r\, \Delta r_{Rudd}\, L\, \Delta E_{Rudd}} = \frac{N_{Rudd}(r, E)\, dt}{2\pi r\, \Delta r_{Rudd}\, L\, \Delta E_{Rudd}\, N_{electrons}} \tag{4.29}$$

$$\tau_{Rudd}(r, E) = \frac{N_{Rudd}(r, E)\, dt}{N_{electrons}} \tag{4.30}$$

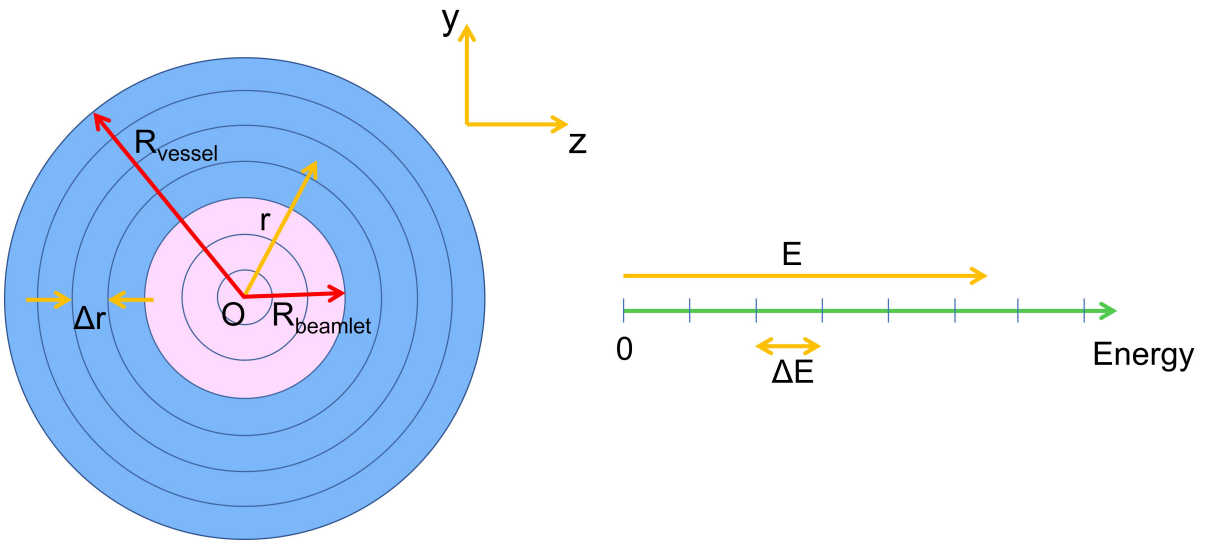

Figure 4.19: Simplified scheme to interpret the binning of histograms of figure 4.9 and 4.18.

In particular, $2\pi r\, \Delta r$ represent the area of the circular corona of radius r, L the length of the cylindrical simulation domain and $N_{electrons}$ the total number of electrons fired during the numerical computation.

4.6 Conclusion of the chapter

The aim of this chapter was to investigate several kinds of electrons that can be found along the drift region; in particular, it was found that co-extracted electrons and electrons stripped along the accelerator column does not give a significant contribution to the B_α emission; whereas, for electrons stripped along the drift region and Rudd ionization electrons this has not been determined yet. Nonetheless, they were found to have a specific energy and angular distribution from which it was possible to determine their radial spreading along the drift region by means of a simple numerical simulation. The results of this simulations will be then exploited in the next chapter to determine whether Rudd or stripped electrons are capable of justifying the luminous background in the beam tomography spectrum.

Chapter 5

B_α emission

Thanks to the knowledge of $\nu(r, E)$ found in the previous section for both Rudd and stripped electrons it is possible to find their B_α emission rates and to compare them with emission produced and induced by fast beam atoms. In particular, the aim of this chapter is to artificially reproduce the beam tomography spectrum starting from the different emission rates and to understand whether the presence of stripped or Rudd electrons is capable of justifying the luminous background in the space between the beamlets. The first contribution to light emission that is investigated in the next section is from dissociative excitation by Rudd ionization electrons.

5.1 H_2 dissociative excitation by Rudd electrons

The B_α emission rate by Rudd electron driven H_2 dissociative excitation can be expressed as a function of the distance r from the beamlet axis in the following way:

$$\left.\frac{dn}{dt}\right|_{Rudd}(r) = \phi_{Rudd} \sum_E \nu_{Rudd}(r, E)\, n_{H_2}\, \sigma_{dis}(E)\, v(E)\, \Delta E_{Rudd} = \tag{5.1}$$

$$= \phi_{Rudd} \sum_E \frac{N_{Rudd}(r, E)\, dt}{2\pi r\, \Delta r_{Rudd}\, L\, \Delta E_{Rudd}\, N_{electrons}}\, n_{H_2}\, \sigma_{dis}(E)\, v(E)\, \Delta E_{Rudd} \tag{5.2}$$

where the result is obtained by summing over all the bin values E along the energy axis, n_{H_2} is the H_2 density, $\sigma_{dis}(E)$ the dissociative excitation cross section of figure 5.2 for the production of n=3 excited atoms, $v(E)$ the electron velocity for electrons with energy E and finally, ϕ_{Rudd} the number of Rudd electrons per unit time produced by the beamlet interaction with the H_2 gas

$$\phi_{Rudd} = \frac{n_{H_2}\, \overline{\sigma}_{iz}\, I\, L}{e} \tag{5.3}$$

with $I = 25\,\text{mA}$ the current of a single beamlet, L the domain length of figure 4.2, e the elementary charge and $\overline{\sigma}_{iz}$ the effective ionization cross section by atom or ion impact on H_2 through which a Rudd electrons are produced:

$$\overline{\sigma}_{iz} = \frac{\Gamma^{H^-}\, \sigma^-_{iz}(E_b) + \Gamma^{H}\, \sigma^0_{iz}(E_b) + \Gamma^{H^+}\, \sigma^+_{iz}(E_b)}{\Gamma^{H^-} + \Gamma^{H} + \Gamma^{H^+}} = \tag{5.4}$$

$$= 0.70\, \sigma^-_{iz}(E_b) + 0.25\, \sigma^0_{iz}(E_b) + 0.05\, \sigma^+_{iz}(E_b)$$

where $\sigma^0_{iz}(E_b)$, $\sigma^-_{iz}(E_b)$, $\sigma^-_{iz}(E_b)$ are the target ionization cross sections for atom, positive or negative ion impact on H_2 computed at the beam energy $E_b = 48\,\text{keV}$; whereas Γ^H, Γ^{H^-}, Γ^{H^+} the atom, negative and positive ion beam fluxes. Since the length L of the SPIDER drift region is on the order of 1 m, the beam fluxes can be estimated thanks to the graph of figure 3.4 where the beam species fluxes are represented as a function of the distance travelled along the drift region. In particular, for distances smaller than 1 m where the diagnostic systems operate the beamlet is approximately composed of 70% negative ions, 25% neutral atoms and the remaining 5% positive ions.

#	σ	reaction	name	ref.	comment
1	σ^+_{iz}	$\underline{H}^+ + H_2 \longrightarrow \underline{H}^+ + H_2^+ + e^-$	ionization	[18]	-
2	σ^0_{iz}	$\underline{H} + H_2 \longrightarrow \underline{H} + H_2^+ + e^-$	ionization	[18]	-
3	σ^-_{iz}	$\underline{H}^- + H_2 \longrightarrow \underline{H}^- + H_2^+ + e^-$	ionization	-	a)
4	σ_{dis}	$\underline{e}^- + H_2 \longrightarrow \underline{e}^- + H + H(n=3)$	dissociative excitation	[20]	-

Table 5.1: Reactions exploited to find the emission rate induced by Rudd electrons

Comments to table 5.1:

a) Since σ^-_{iz} was not found in literature, it was chosen equal to σ^0_{iz}, namely $\sigma^-_{iz} = \sigma^0_{iz}$

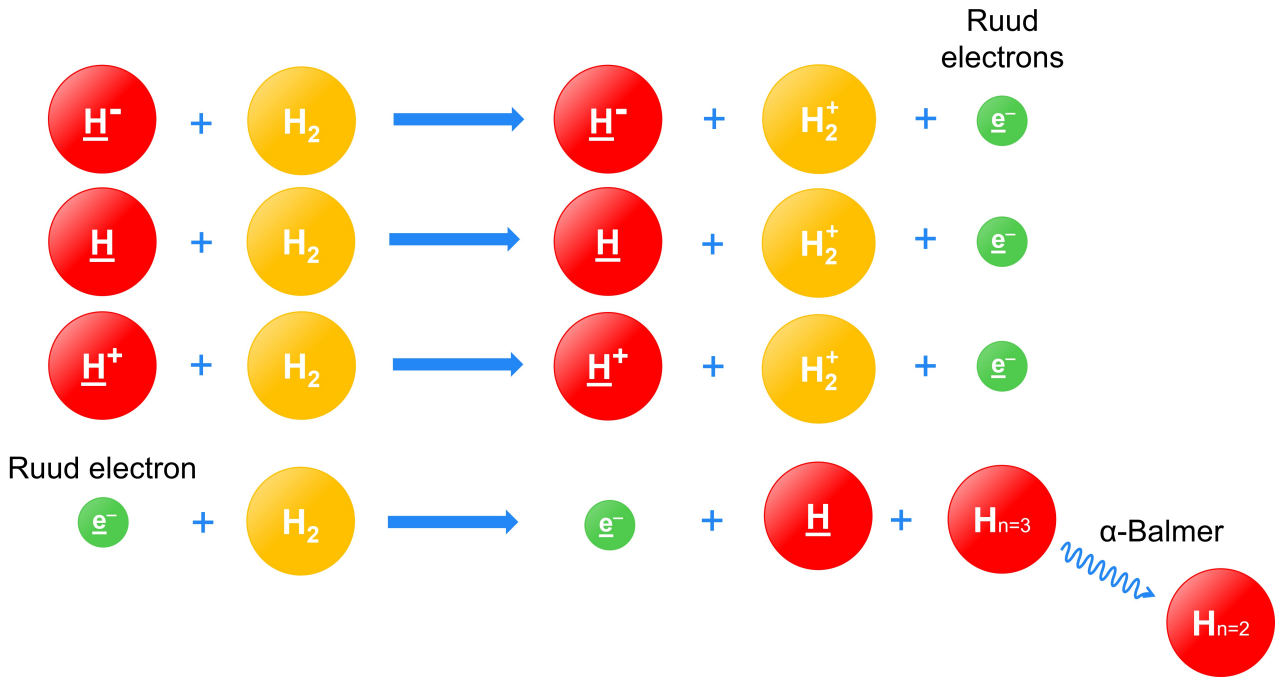

Figure 5.1: Processes leading to the formation of Rudd electrons and production of n=3 excited atoms by Rudd electron driven dissociative excitation

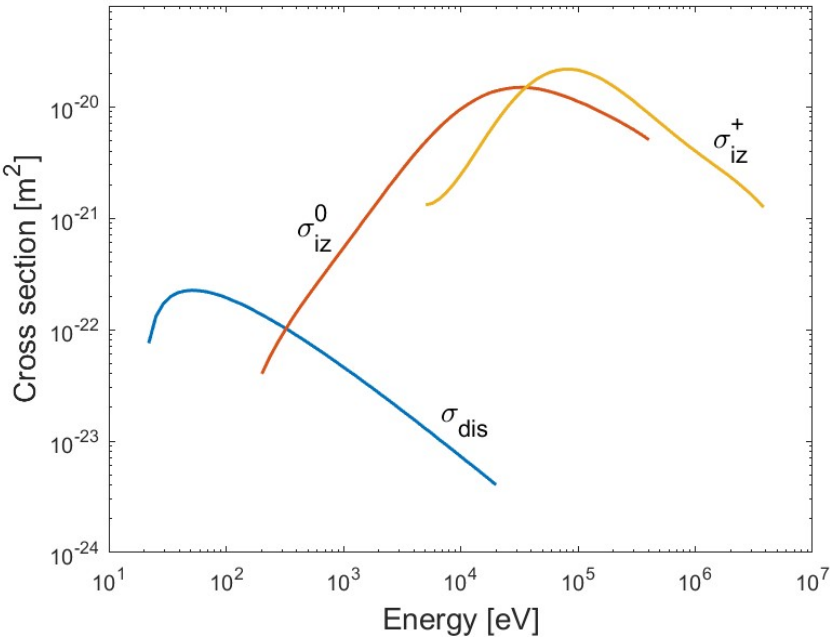

Figure 5.2: Cross sections exploited to find the emission rate induced by Rudd electrons

5.2 H_2 dissociative excitation by stripped electrons

The B_α emission rate by stripped electron driven H_2 dissociative excitation can be expressed as a function of the distance r from the beamlet axis in the following way:

$$\left.\frac{dn}{dt}\right|_{strip}(r) = \phi_{strip} \sum_E \nu_{strip}(r,E)\, n_{H_2}\, \sigma_{dis}(E)\, v(E)\, \Delta E_{strip} = \\ = \phi_{strip} \sum_E \frac{N_{strip}(r,E)\, dt}{2\pi r\, \Delta r_{strip}\, L\, \Delta E_{strip}\, N_{electrons}}\, n_{H_2}\, \sigma_{dis}(E)\, v(E)\, \Delta E_{strip} \tag{5.5}$$

The working principle of the previous equation is the same as the previous section but applied to stripped electrons. In particular, ϕ_{strip} is the number of stripped electrons per unit time produced by the beamlet interaction with the H_2:

$$\phi_{strip} = \frac{n_{H_2}\, \overline{\sigma}_{strip}\, I\, L}{e} \tag{5.6}$$

where $\overline{\sigma}_{strip}$ is the effective stripping cross section defined as

$$\overline{\sigma}_{strip} = \frac{\Gamma^{H^-}\left[\sigma^-_{strip}(E_b) + 2\sigma^-_{2strip}(E_b)\right] + \Gamma^H\, \sigma^0_{strip}(E_b)}{\Gamma^{H^-} + \Gamma^H + \Gamma^{H^+}} = \\ = 0.75\left[\sigma^-_{strip}(E_b) + 2\sigma^-_{2strip}(E_b)\right] + 0.20\, \sigma^0_{strip}(E_b) \tag{5.7}$$

where $\sigma^-_{strip}(E_b)$, $\sigma^-_{2strip}(E_b)$ and $\sigma^0_{strip}(E_b)$ are the electron stripping cross sections, while Γ^{H^-}, Γ^H and Γ^{H^+} the beam fluxes.

#	σ	reaction	name	ref.	comment
1	σ^{-}_{strip}	$\underline{H}^- + H_2 \longrightarrow \underline{H} + \underline{e}^- + H_2$	single stripping	[18]	-
2	σ^{-}_{2strip}	$\underline{H}^- + H_2 \longrightarrow \underline{H}^+ + 2\,\underline{e}^- + H_2$	double stripping	[18]	-
3	σ^{0}_{strip}	$\underline{H} + H_2 \longrightarrow \underline{H}^+ + \underline{e}^- H_2$	single stripping	[18]	-
4	σ_{dis}	$\underline{e}^- + H_2 \longrightarrow \underline{e}^- + H + H(n=3)$	dissociative excitation	[20]	-

Table 5.2: Reactions exploited to find the emission rate induced by stripped electrons

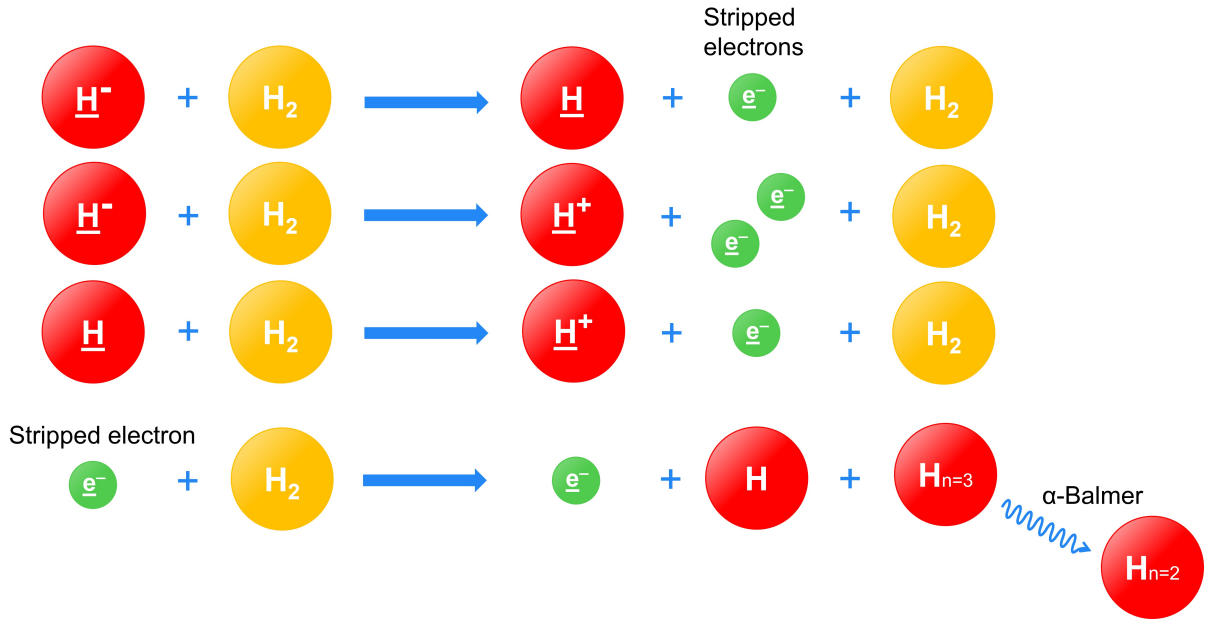

Figure 5.3: Processes leading to the formation of stripped electrons and production of n=3 excited atoms by stripped electron driven dissociative excitation

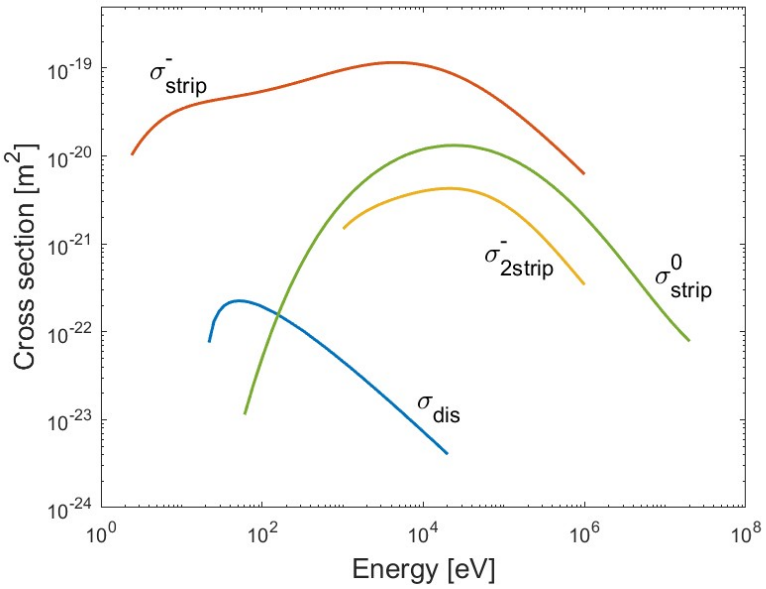

Figure 5.4: Cross sections exploited to find the emission rate induced by stripped electrons

5.3 Excitation of fast beam atoms

The B_α emission rate by fast excited beam atoms can be expressed as a function of the distance r from the beamlet axis in the following way:

$$\left.\frac{dn}{dt}\right|_{beam\,exc}(r) = A\,\exp\left(-\frac{r^2}{2\rho^2}\right) n_{H_2}\,\overline{\sigma}_{exc} \tag{5.8}$$

where the beamlet longitudinal section is approximated as in figure 5.5 with trapezoidal shape where the divergence is determined by the angle $\omega = 10\,\text{mrad}$, the radius at the drift region entrance is $R_{beamlet}$ =7 mm, and $R_{divergence}$ the radius of the diverging beam in the middle of the drift region

$$R_{divergence} = R_{beamlet} + x\sin\omega \sim R_{beamlet} = R_{beamlet} + x\sin\omega \tag{5.9}$$

where, as figure 5.5 shows, x denotes the distance between the entrance of the drift region and the zone in which diagnostics like BES and beam tomography operate. In this simulation x is taken equal to 0.5 m, yet the precise position of the diagnostics will not be crucial in determining the final numerical results. Concerning the density profile, it is assumed to have a gaussian shape centred on the beamlet axis with ρ as standard deviation chosen in such a way that $R_{divergence}$ coincides with 3 times the standard deviation of the gaussian profile:

$$\rho = \frac{R_{divergence}}{3} \tag{5.10}$$

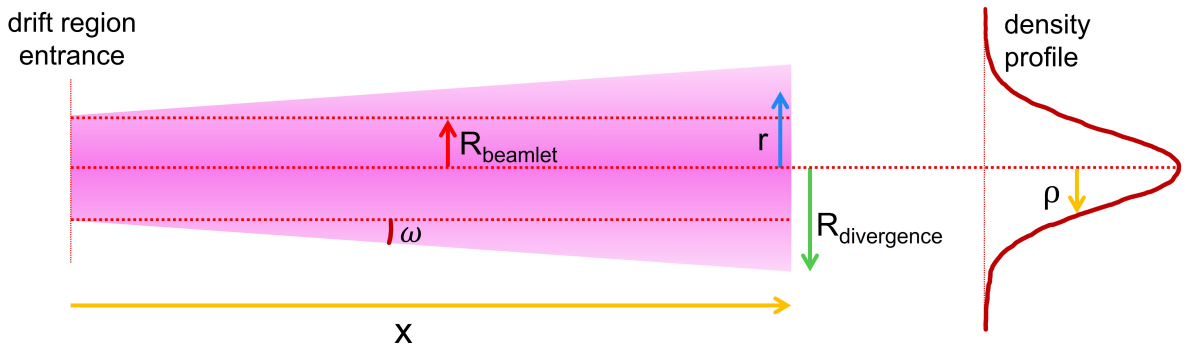

Figure 5.5: Beamlet longitudinal section and gaussian density profile

The constant A in equation 5.8 is found setting the following integral equal to I/e, that is the number of electron per unit time crossing the circular beamlet transverse section of area S at a distance x from the drift region entrance

$$\int_S A\,\exp\left(-\frac{r^2}{2\rho^2}\right) dS = \frac{I}{e} \quad \Longrightarrow \quad \int_0^{R_{beamlet}} A\,\exp\left(-\frac{r^2}{2\rho^2}\right) 2\pi r dr = \frac{I}{e} \tag{5.11}$$

Since the area under the tail of the distribution is very small compared to the total area under the curve, the integral can be approximated taking $R_{beamlet} \to +\infty$ and, by properly replacing A, the emission rate becomes

$$\left.\frac{dn}{dt}\right|_{beam\,exc}(r) = \frac{I}{2\pi\rho^2 e}\,\exp\left(-\frac{r^2}{2\rho^2}\right) n_{H_2}\,\overline{\sigma}_{exc} \tag{5.12}$$

Finally, $\overline{\sigma}_{exc}$ is the effective cross section for the n=3 excitation of beam atoms

$$\overline{\sigma}_{exc} = \frac{\Gamma^{H^-}\,\sigma^-_{exc}(E_b) + \Gamma^{H}\,\sigma^0_{exc}(E_b) + \Gamma^{H^+}\,\sigma^+_{exc}(E_b)}{\Gamma^{H^-} + \Gamma^{H} + \Gamma^{H^+}} =$$

$$= 0.70\,\sigma^-_{exc}(E_b) + 0.25\,\sigma^0_{exc}(E_b) + 0.05\,\sigma^+_{exc}(E_b) \tag{5.13}$$

The reactions bringing to the formation of a fast n=3 excited atoms are reported in table 5.3 and represented in figure 5.6

#	σ	reaction	name	ref.	comment
1	σ^+_{exc}	$\underline{H}^+ + H_2 \longrightarrow \underline{H}(n=3) + H_2^+$	charge exchange	-	a)
2	σ^0_{exc}	$\underline{H} + H_2 \longrightarrow \underline{H}(n=3) + H_2$	excitation	-	b)
3	σ^-_{exc}	$\underline{H}^- + H_2 \longrightarrow \underline{H}(n=3) + \underline{e}^- + H_2$	single stripping	-	c)

Table 5.3: Reactions exploited to find the emission rate by fast excited beam atoms

Comments to table 5.3

a) Since σ^+_{exc} was not found in literature, it was obtained by summing the single cross sections contribution reported in table 3.3 to excite the projectile to the 3s, 3d and 3d level starting from a positive ion as projectile: $\sigma^+_{exc} = \sigma_{10_{3s}} + \sigma_{10_{3p}} + \sigma_{10_{3d}}$;

b) Likewise point a), $\sigma^0_{exc} = \sigma_{0_{1s}0_{3s}} + \sigma_{0_{1s}0_{3p}} + \sigma_{0_{1s}0_{3d}}$;

c) Likewise points a) and b), $\sigma^-_{exc} = \sigma_{-10_{3s}} + \sigma_{-10_{3p}} + \sigma_{-10_{3d}}$.

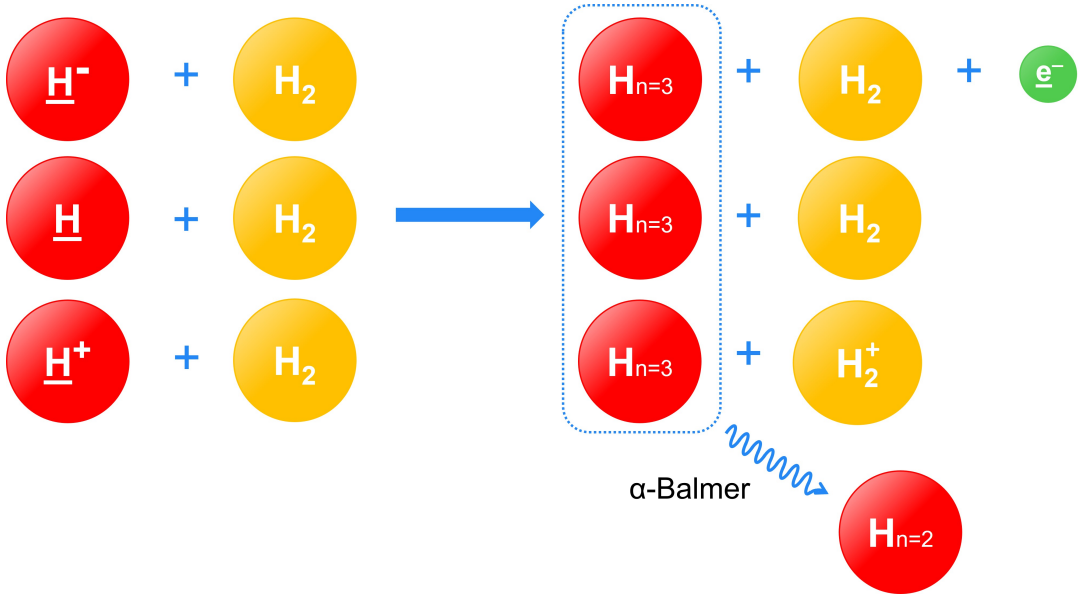

Figure 5.6: Processes leading to the formation of fast n=3 excited atoms

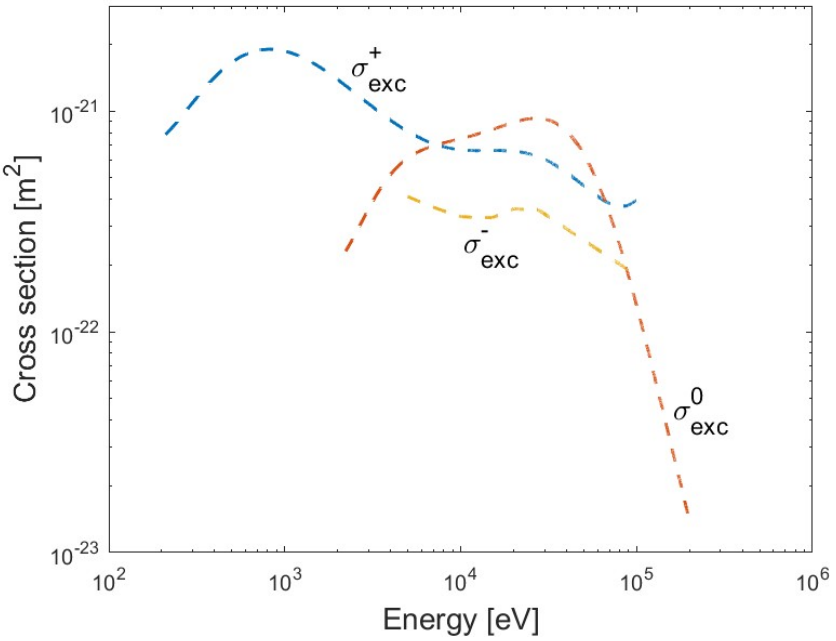

Figure 5.7: Cross sections exploited to find the emission rate by fast excited beam atoms

5.4 H_2 dissociative excitation by fast beam particles

Finally, the B_α emission rate by H_2 dissociative excitation induced by fast beam atoms or ions can be expressed as a function of the distance r from the beamlet axis in the following way:

$$\left.\frac{dn}{dt}\right|_{beam\,disexc}(r) = \frac{I}{2\pi\rho^2 e}\,\exp\left(-\frac{r^2}{2\rho^2}\right) n_{H_2}\,\overline{\sigma}_{dis} \tag{5.14}$$

where the only difference with respect to the previous sections consists in the effective dissociative excitation cross section $\overline{\sigma}_{dis}$ defined as

$$\overline{\sigma}_{dis} = \frac{\Gamma^{H^-}\,\sigma^-_{dis}(E_b) + \Gamma^{H}\,\sigma^0_{dis}(E_b) + \Gamma^{H^+}\,\sigma^+_{dis}(E_b)}{\Gamma^{H^-} + \Gamma^{H} + \Gamma^{H^+}} = \tag{5.15}$$

$$= 0.70\,\sigma^-_{dis}(E_b) + 0.25\,\sigma^0_{dis}(E_b) + 0.05\,\sigma^+_{dis}(E_b)$$

where the exploited reactions are reported in table 5.4 along with their cross sections in figure 5.9

#	σ	reaction	name	ref.	comment
1	σ^0_{dis}	$\underline{H} + H_2 \longrightarrow \underline{H} + H + H(n=3)$	dissociative excitation	[18]	-
2	σ^+_{dis}	$\underline{H}^+ + H_2 \longrightarrow \underline{H}^+ + H + H(n=3)$	dissociative excitation	-	a)
3	σ^-_{dis}	$\underline{H}^- + H_2 \longrightarrow \underline{H}^- + H + H(n=3)$	dissociative excitation	-	a)

Table 5.4: Reactions exploited to find the emission rate by H_2 dissociative excitation induced by fast beam atom or ion impact

Comments to table 5.4:

a) Since $\sigma^{\pm}_{dis}$ were not found in literature, they were arbitrary taken equal to σ^{0}_{dis}, namely $\sigma^{\pm}_{dis} = \sigma^{0}_{dis}$

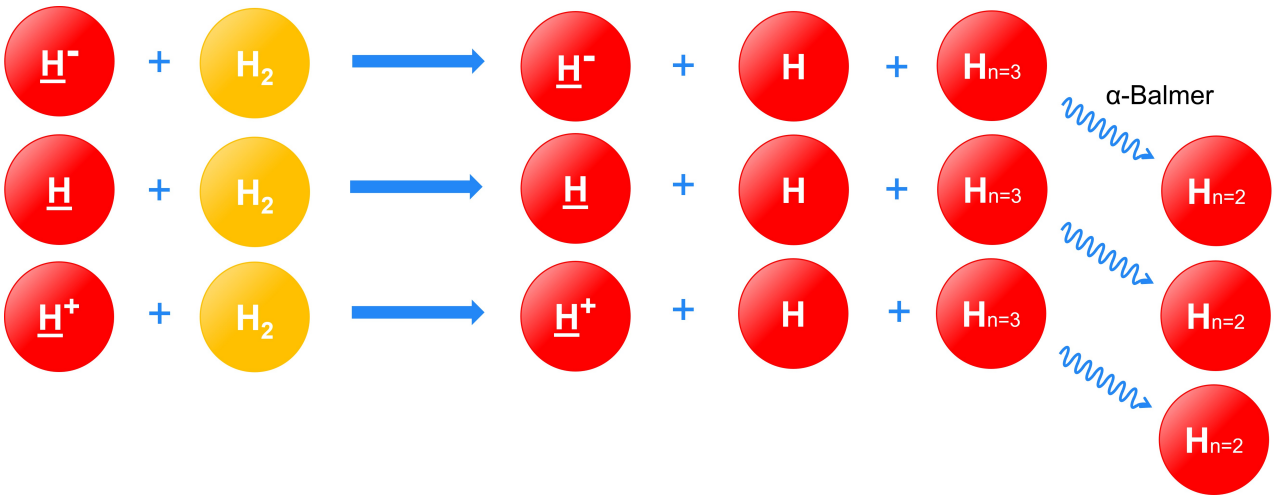

Figure 5.8: Processes leading to the formation of slow n=3 excited atoms

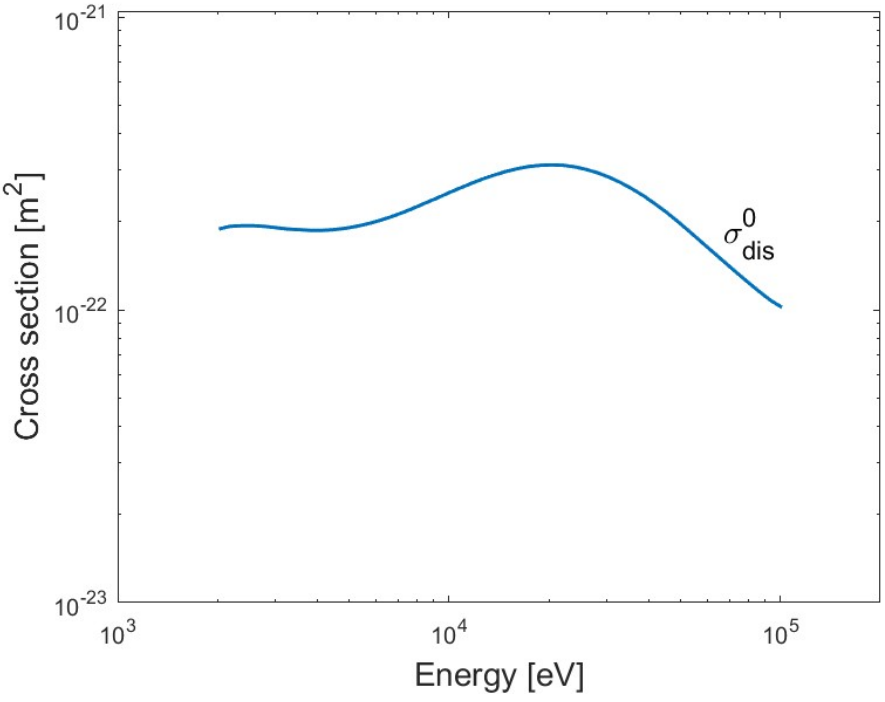

Figure 5.9: Dissociative excitation cross section by atom impact

5.5 Beam tomography simulated spectrum

Once determined all the single contributions starting from the known electron distributions and from the beam composition, the beam tomography spectrum can be reproduced. First of all, all the four emission rate contributions must be summed yielding the total single beamlet emission rate at a distance x from the drift region entrance as a function of the distance r from the beamlet axis:

$$\left.\frac{dn}{dt}\right|_{single\,beamlet}(r) = \left.\frac{dn}{dt}\right|_{strip}(r) + \left.\frac{dn}{dt}\right|_{Rudd}(r) + \left.\frac{dn}{dt}\right|_{beam\,exc}(r) + \left.\frac{dn}{dt}\right|_{beam\,disexc}(r) \qquad (5.16)$$

Yet, this is only the contribution for a single beamlet: other beamlets whose spatial position is represented in figure 5.10 were exploited during the 2021 SPIDER experimental campaign.

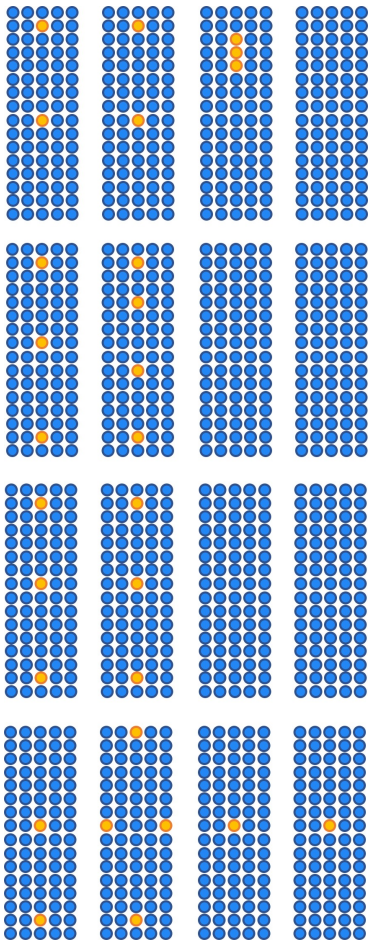

Figure 5.10: SPIDER's plasma grid beamlet pattern during the 2021 experimental campaign. Yellow points represents open beamlets, while blue ones those closed by the plasma grid mask.

To reproduce the beam tomography spectrum, the emission rate for each beamlet must be superimposed and the result must be integrated along many lines of sights as in figure 5.11.

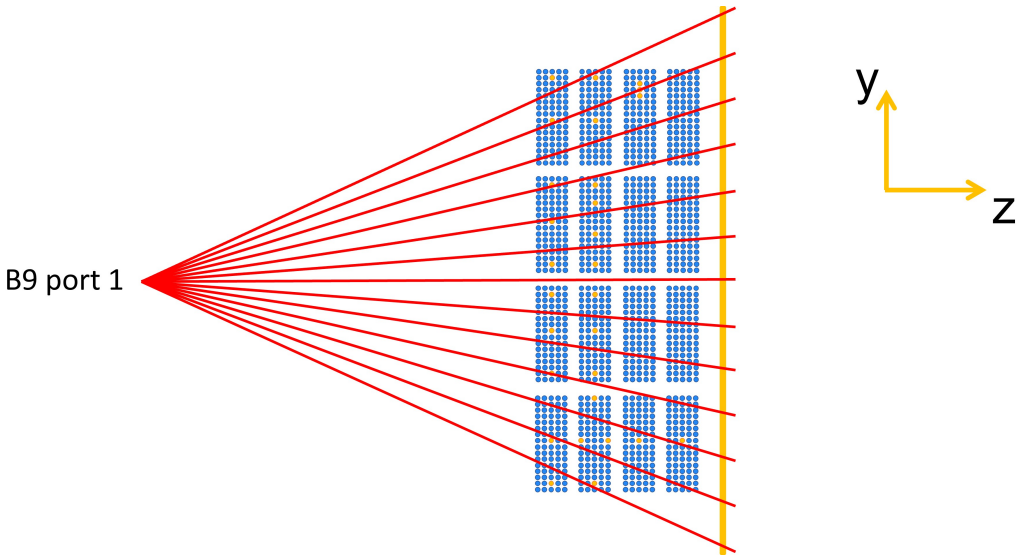

Figure 5.11: Fan of lines of sight (LoS) to reproduce the beam tomography spectrum

To perform the integration along a single line of sight the following integral is exploited

$$\epsilon_{LoS} = \int_{LoS} \left.\frac{dn}{dt}\right|_{total} d\ell = \int_{LoS} \sum_{j=1}^{N'} \left.\frac{dn}{dt}\right|_{j^{th}\ single\ beamlet} d\ell \tag{5.17}$$

where the total emission rate is obtained as a superposition of the emission contributions from all the N' beamlets. Yet, to perform the integration numerically, the line of sight into consideration is discretized in N arbitrary small steps of length $\delta\ell$ represented with green points in figure 5.12; thus the previous integral can be approximated as

$$\epsilon_{LoS} \sim \sum_{i=1}^{N}\sum_{j=1}^{N'} \left.\frac{dn}{dt}\right|_{j^{th}\ single\ beamlet} (r_{ij}) \cdot \delta\ell \tag{5.18}$$

where the emission rate is a function of r_{ij}, namely the distance of the i-th position along the LoS from the j-th beamlet axis.

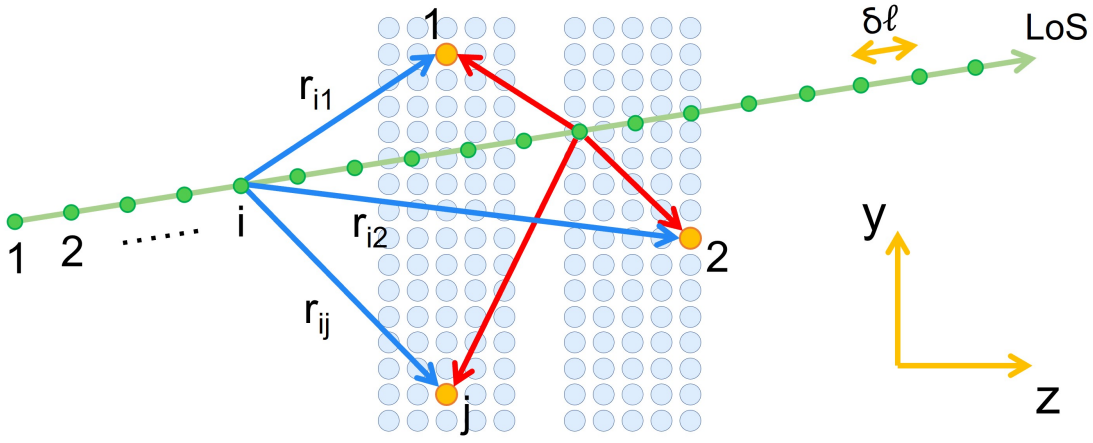

Figure 5.12: Scheme for the integration process along a single line of sight (LoS)

$$\epsilon_{LoS} = \int_{LoS} \left.\frac{dn}{dt}\right|_{total} d\ell \sim \sum_{i=1}^{n}\sum_{j=1}^{N} \left.\frac{dn}{dt}\right|_{single\,beamlet} (r_{ij}) \cdot \delta\ell \tag{5.19}$$

However, to get the full tomography spectrum, this process must be repeated for different lines of sight like in figure 2.5: each point on the horizontal axis of the spectrum represents a single LoS, while the corresponding value on the vertical axis the result of the integration along that specific line of sight.

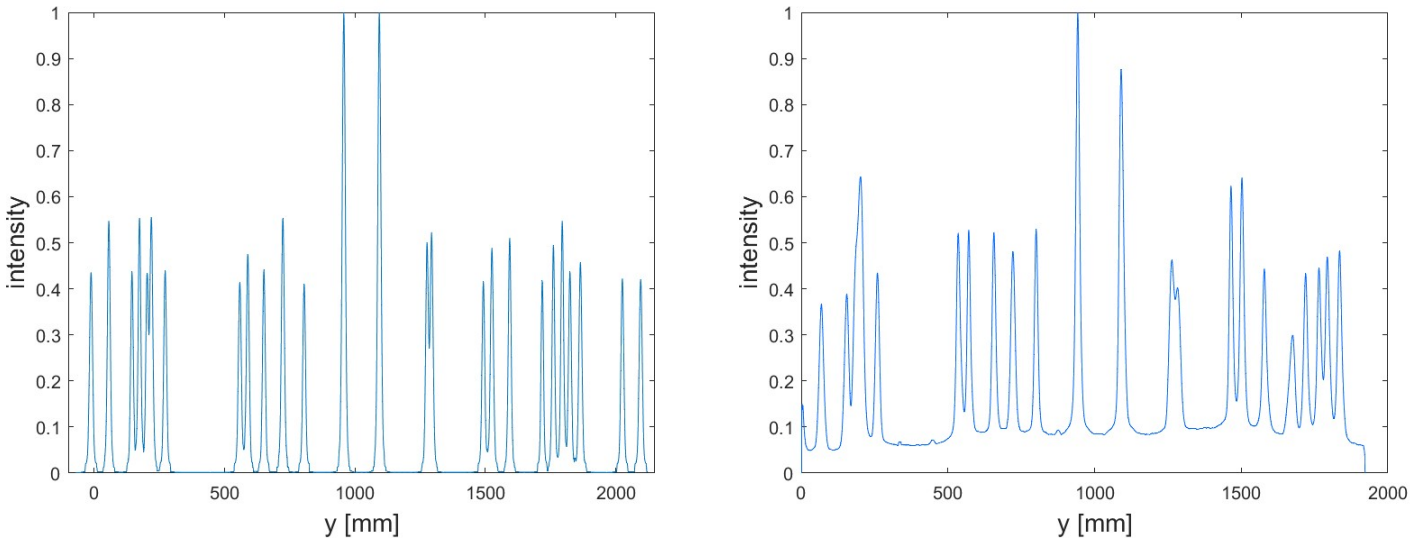

(a) Simulated spectrum

(b) Experimental findings

Figure 5.13: Beam tomography spectrum from camera B9 port 01. The simulated spectrum is represented in the left panel while the experimental findings in blue in the right panel. The red curve in the right panel is the curve fitting the experimental data. Both graphs are normalized to the height of the highest peak.

The two graphs of figure 5.13 show the simulated and the experimental spectra respectively normalized to the height of the highest peak. It can be observed that the position of the peaks in the simulated spectrum matches the experimental findings; however, due to the better resolution achievable numerically, the peaks are much better defined in the reproduced spectrum. Furthermore, the most interesting aspect to notice is the luminous background present between one peak and the others in the experimental but not in the simulated result. To understand the reason of that, the simulated spectrum is split in figure 5.14 in its four contributions: the largest contribution stems from beam excited atoms followed by target dissociative excitation induced by atom or ion impact and target dissociative excitation induced by stripped electron impact. Concerning instead Rudd electrons, their contribution is negligible and this is the reason why a luminous background is not observed in the simulated spectrum.

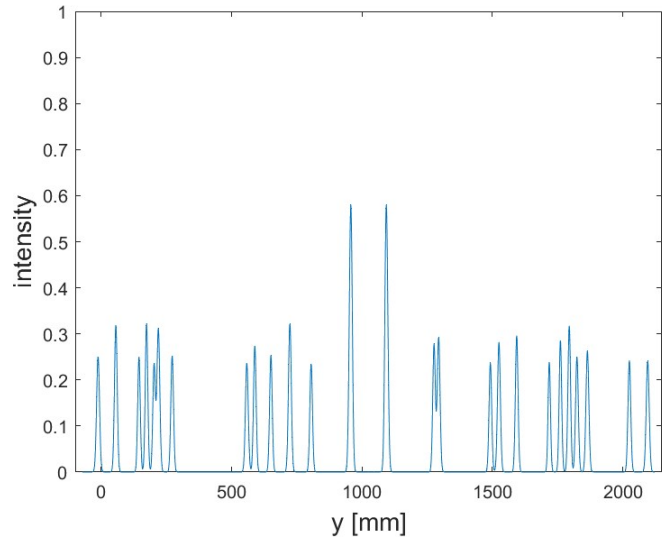

(a) Excitation of fast beam atoms

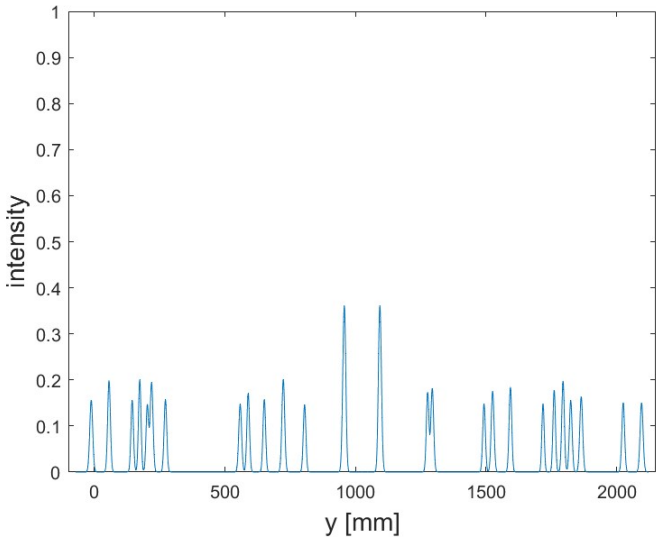

(b) H_2 dissociative excitation by fast beam atom or ion impact

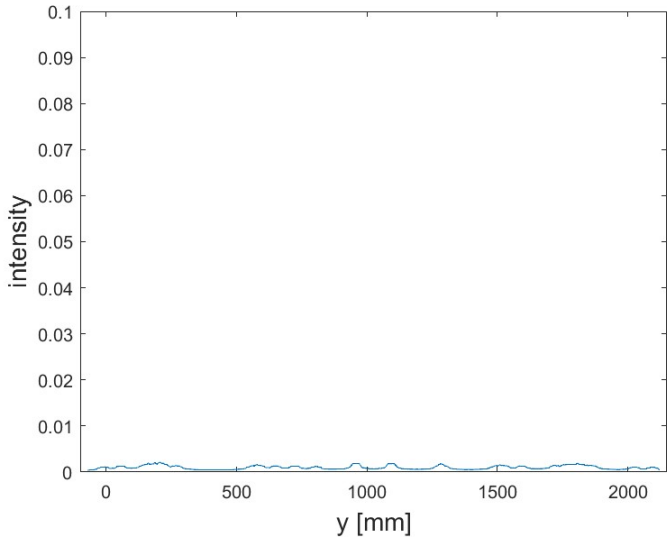

(c) H_2 dissociative excitation by Rudd electron impact

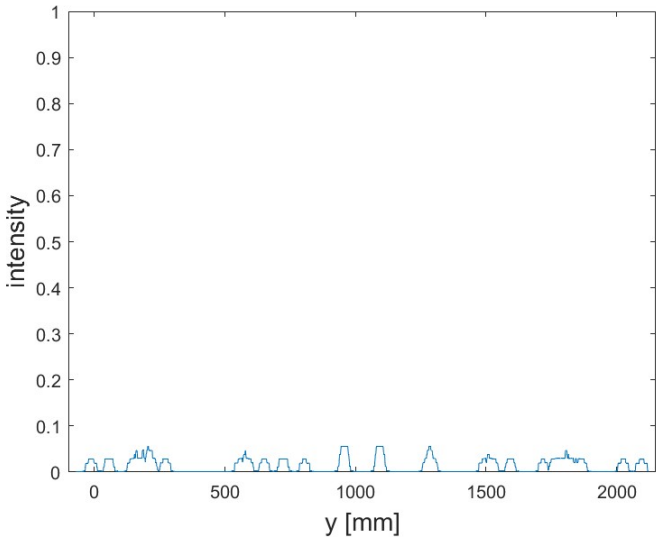

(d) H_2 dissociative excitation by stripped electron impact

Figure 5.14: Different contributions to the tomography spectrum of figure 5.13.

Other examples of reproduced and experimental spectra are reported in figures 5.16 and 5.17. Even in that cases the luminous background is observed in the experimental measurements but not in the simulated spectra. To conclude, this piece of evidence highlights the fact that, according to this model, Rudd electrons are not able to justify the consistent amount of B_α light emitted in the space between one beamlet and the others.

Figure 5.15: Fan of line of sights for camera B8 port 15 and camera B2 port 03

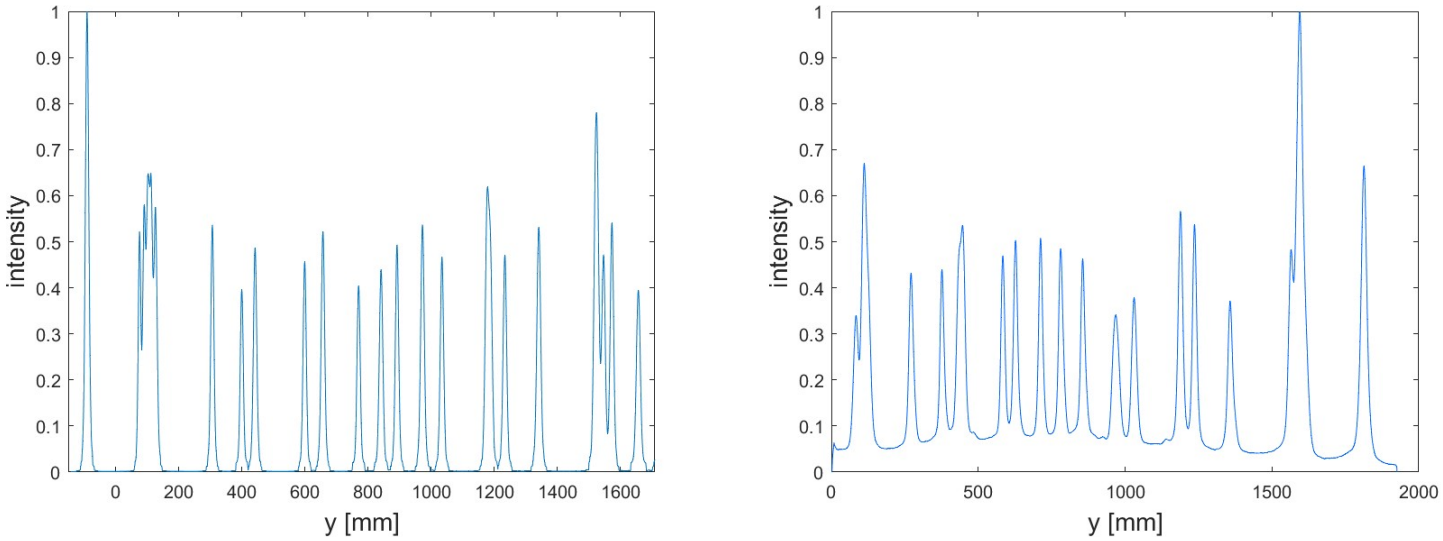

(a) Simulated spectrum

(b) Experimental findings

Figure 5.16: Beam tomography spectrum from camera B8 port 15.

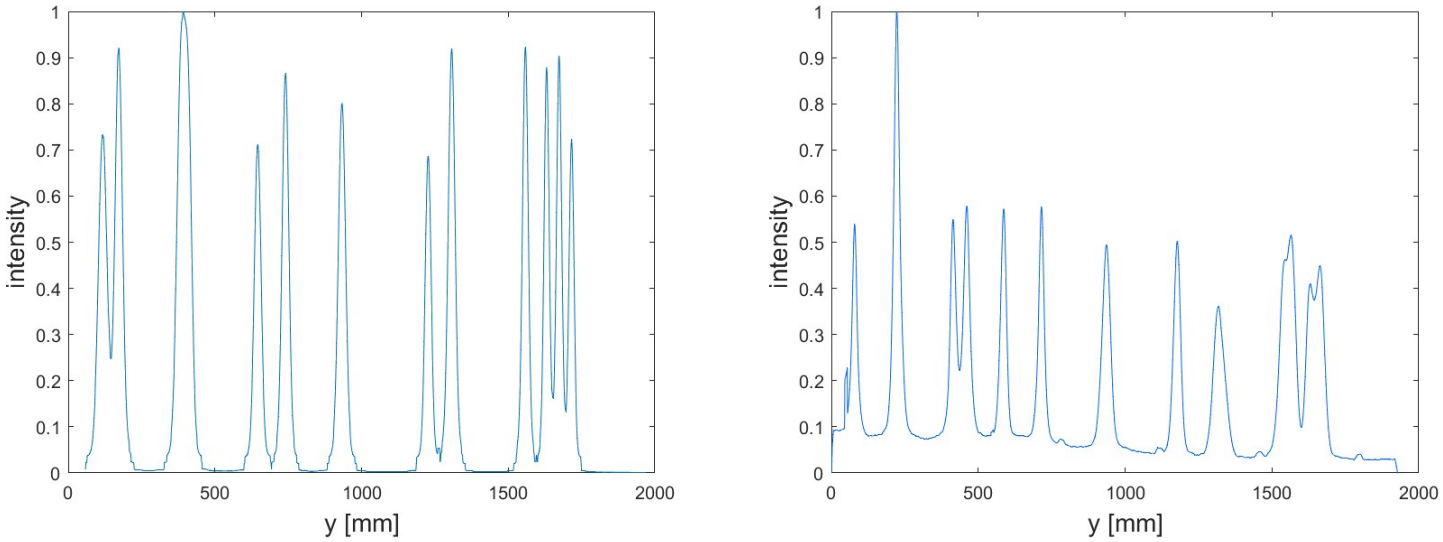

(a) Simulated spectrum

(b) Experimental findings

Figure 5.17: Beam tomography spectrum from camera B2 port 03.

5.6 Conclusion of the chapter

The aim of this chapter was to reproduce the experimental findings from beam tomography spectrum starting from the propagating beam and the knowledge of the angular distribution of Rudd and stripped electrons. Despite the simulation well reproduces the position of the peaks and with a much better resolution, it was not able to justify the luminous background in the experimental data. As a consequence, according to this model, Rudd electrons are not the right answer to justify the inter-beamlet luminosity. Yet, not all the production mechanisms for electrons are included in the model. For example, to include relatively slow electrons from single and double dissociative ionization, it would also be necessary to properly treat their dynamics inside the beam plasma. Moreover, this model does not consider the effects that the electrostatic potential arising from the formation of the beam plasma could have on beam and plasma particles. To these purposes a more accurate approach capable of modelling the particle motion and the formation of the beam plasma will be adopted with a Particle-In-Cell (PIC) code, as described in the next chapter.

Chapter 6

GPPIC

6.1 The Particle-In-Cell (PIC) method

Particle-in-Cell (PIC) simulation represents a powerful tool for plasma studies having a number of advantages like the fully kinetic description of plasmas and the ability to incorporate complicated atomic and plasma-surface interactions [29]. The system is described as a finite collection of charged particles which moving inside a finite simulation domain [7]. However, the number of particles in a real plasma is extremely large and exceeds by orders of magnitude the maximum possible number of particles whose time evolution can be handled by the best supercomputers. To get over the problem it is necessary to reduce the number of degrees of freedom by grouping the large amount of real physical particles in a much smaller number of macroparticles (MPs); in other words, a macroparticle represents a given number of physical particles [29]. The number of particles represented by a single macroparticle is called macroparticle weight (MPW) and can be defined as the ratio between the total number N of real particles and the number N_{MP} of simulated macroparticles [7]

$$MPW = \frac{N}{N_{MP}} = \frac{n\,V}{N_{MP}} \tag{6.1}$$

where n and V are the real system density and volume [7]. The ratio between the MP density n_{MP} and the real particle density n defines the density scaling factor, β

$$\beta = \frac{n_{MP}}{n} \tag{6.2}$$

The time evolution of the chosen system can be achieved by repeating a sequence of operations in an iterative fashion. To comply with this task, the time arrow is discretized in small timesteps dt and the simulation domain meshed in small cells. In a simple electrostatic system, the potential ϕ is given by the Poisson equation

$$\nabla^2\phi = -\frac{\rho}{\epsilon_0} \tag{6.3}$$

from which the electric field E and the force F acting on the macroparticles can be computed as

$$E = -\nabla\phi \qquad \longrightarrow \qquad F = qE = -q\nabla\phi \tag{6.4}$$

The code simulates the motion of each macroparticle by solving the equations of motion:

$$\frac{dv}{dt} = \frac{q}{m}E \qquad \longrightarrow \qquad v(t+dt) = v(t) + \frac{q}{m}E\,dt \tag{6.5}$$

$$\frac{dx}{dt} = v \qquad \longrightarrow \qquad x(t+dt) = x(t) + v\,dt \tag{6.6}$$

where q and m are the charge and the mass of the macroparticle. Since the ratio between charge and mass is the same for both macroparticles and plasma particles, macroparticles follow the same trajectory as the corresponding plasma particles; as a result, a MP is absolutely similar to a real one assuming that all necessary parameters like Debye λ_D length and plasma frequency ω_p are properly re-scaled. Once all the macroparticle positions and velocities are found, the new charge density values ρ can be computed and the loop resumes from the solution of the Poisson equation.
To conclude, the dimensionality of the PIC code is usually given as mDnV, where m and n define the dimensionality in the usual and in the velocity spaces respectively.

6.2 *gppic* simulation

The simulation tool used in this thesis work is a 2D3V electrostatic PIC-MCC code called *gppic*, written in C++/CUDA. As figure 6.1 shows, the simulation domain is chosen to be a 49.5 × 43.5 cm rectangular box divided in 660 × 580 nodes whose position does not change over time. The size of each cell is thus 0.075 cm × 0.075 cm.

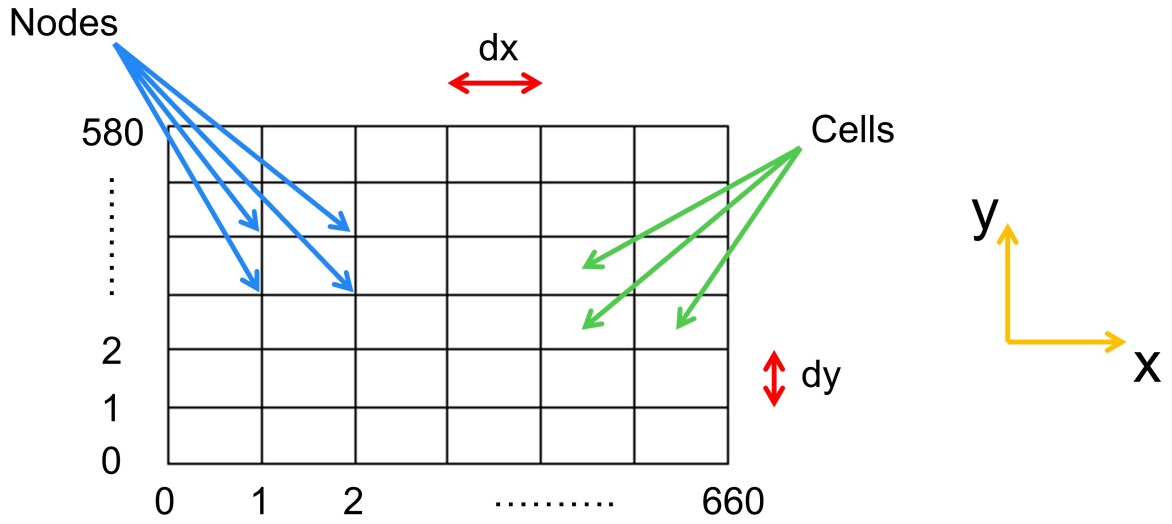

Figure 6.1: PIC domain discretization

Each cell is occupied by a certain number of macroparticles and the values of the physical quantities at each node are obtained by bilinear interpolation [7]. In this way it is possible to obtain 660 × 580 maps showing the values of physical quantities like for example density and velocity at each node for each particle species.

The simulation domain is a two-dimensional plane reproducing a reduced part of the SPIDER drift region. As shown in Figure 6.2 the upper, lower and left boundaries are defined as plain metallic walls (like the SPIDER vessel surfaces) while, apart from a tile placed in the middle that aims at reproducing the STRIKE calorimeter, the right side is left open with no walls. The Grounded Grid (GG) is also included in the domain, placed few millimeters downstream of the left wall and featuring only two apertures with radius 8 mm and inter-axial distance of 7.5 cm apart. The upper and lower walls and the grid are grounded, the STRIKE tile is polarised at +50 V, whereas the left wall potential is set at -1.6 kV to simulate the effects of the potential of the upstream SPIDER grids on the beam. The simulation aims at reproducing two negative ion beamlets propagating from the left boundary, where a certain number N_{H^-} of negative ion macroparticles per timestep are generated with 48 keV beam energy, without including beam divergence. The number of ions is defined as

$$N_{H^-} = \frac{j_b}{q} 2r_b \frac{dt}{\beta \cdot MPW} \tag{6.7}$$

where q is the elementary charge, r_b the beamlet radius, v_b the beam velocity corresponding to the chosen beam energy and j_b the beamlet current density that was assumed to be approximately 120 A/m^2. Concerning instead the composition of the background gas, the beam propagates through molecular hydrogen at a pressure of 30 mPa. The included plasma species are e^-, H^-, H, H^+, H_2^+ and H_3^+.

Physical quantity	Symbol	Value	Physical quantity	Symbol	Value
x-domain size	-	49.5 cm	left wall potential	-	-1.6 kV
y-domain size	-	43.5 cm	tile potential	-	50 V
z-domain size	-	100 cm	-	-	-
Nodes along the x-axis	-	660	upper wall potential	-	0 V
Nodes along the y-axis	-	580	lower wall potential	-	0 V
timestep	dt	0.35 ns	grid potential	-	0 V
x-cell dimension	dx	0.075 cm	beam flux	Γ_b	$5.5 \cdot 10^{20}\, m^{-2} s^{-1}$
y-cell dimension	dy	0.075 cm	beam energy	E_b	48 keV
macroparticle weight	MPW	$1.8 \cdot 10^6$	vessel pressure	p	30 mPa
aperture radius	-	0.8 cm	beamlet radius	r_b	0.6 cm
aperture distance	-	7.5 cm	beamlet current density	j_b	120 A m^{-2}
grid thickness	-	0.6 cm	beamlet divergence	-	0
distance grid/left wall	-	1.5 cm	-	-	-
tile height	-	11.6 cm	-	-	-
density scaling factor	β	1	-	-	-

Table 6.1: *gppic* input parameters

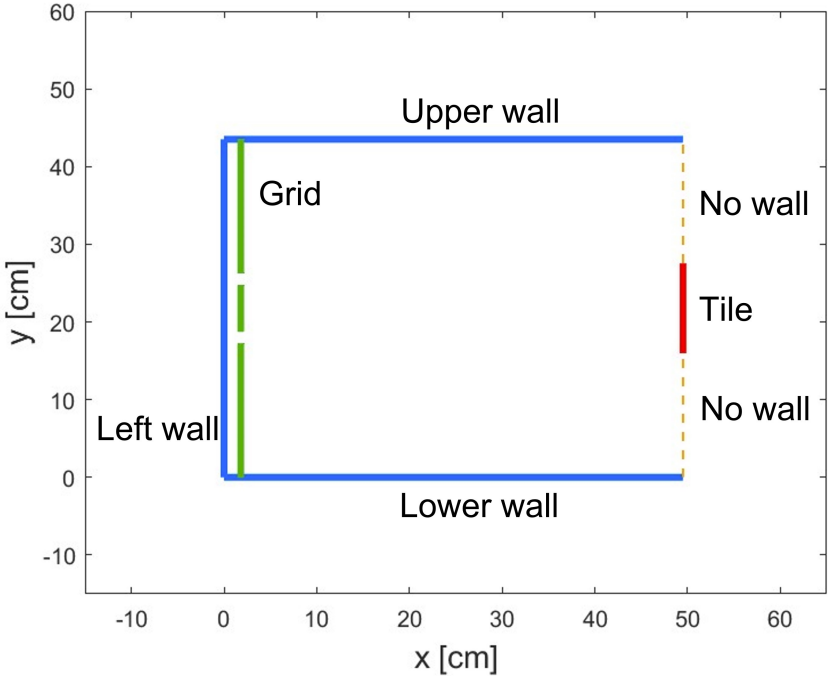

Figure 6.2: Representation of the simulation domain for a 2 beamlet simulation

From the code results it is possible to obtain maps for the physical quantities of interest; density maps for the different species are reported in figure 6.3 as an example.

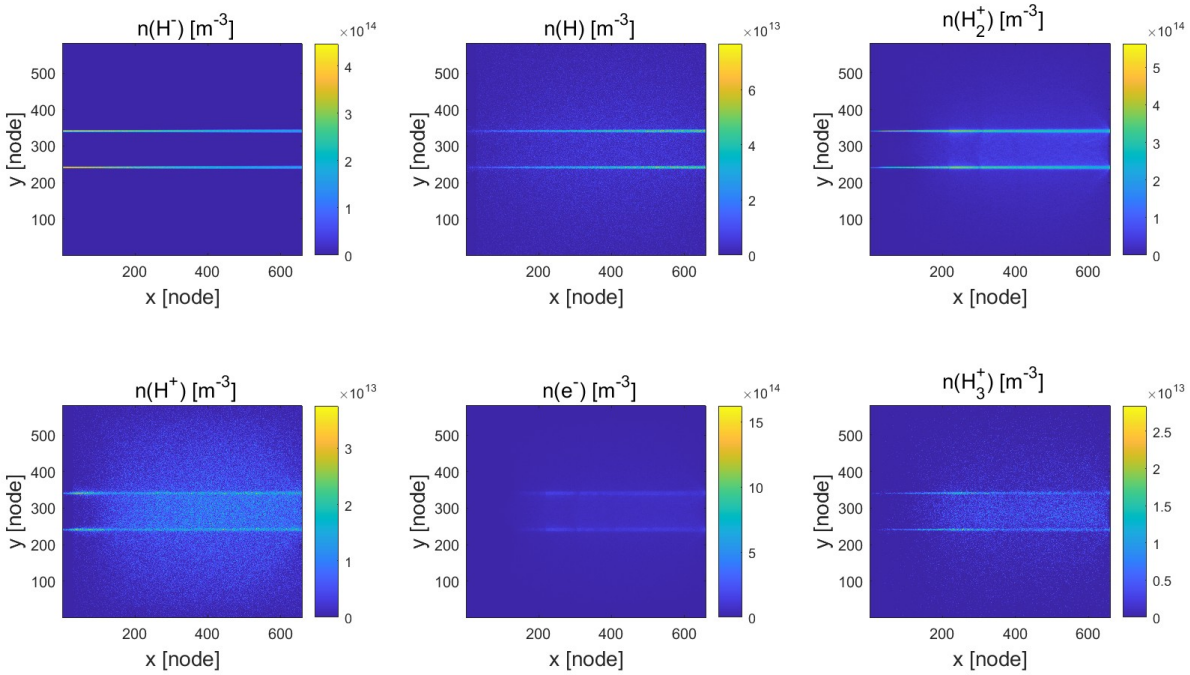

Figure 6.3: Density maps for the different species

From these maps it is possible to observe the presence of a plasma in the regions not occupied by the beamlets. This is also visible in the radial profiles of figure 6.4 and in the potential map of figure 6.5. This is due to plasma diffusion from the beamlets where macroparticles forming the plasma are produced. In particular, the beam plasma density is higher in the region between the two beamlets where the contributions from the two beamlets overlap.

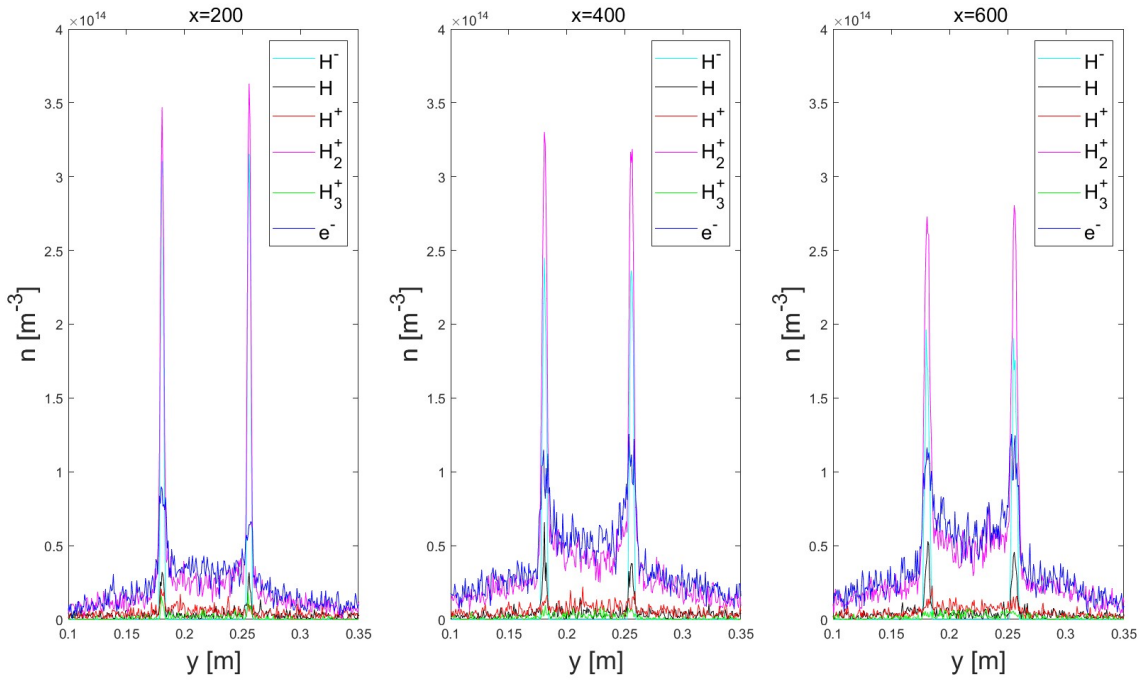

Figure 6.4: Beamlets radial profile at x=200, 400 and 600 nodes respectively

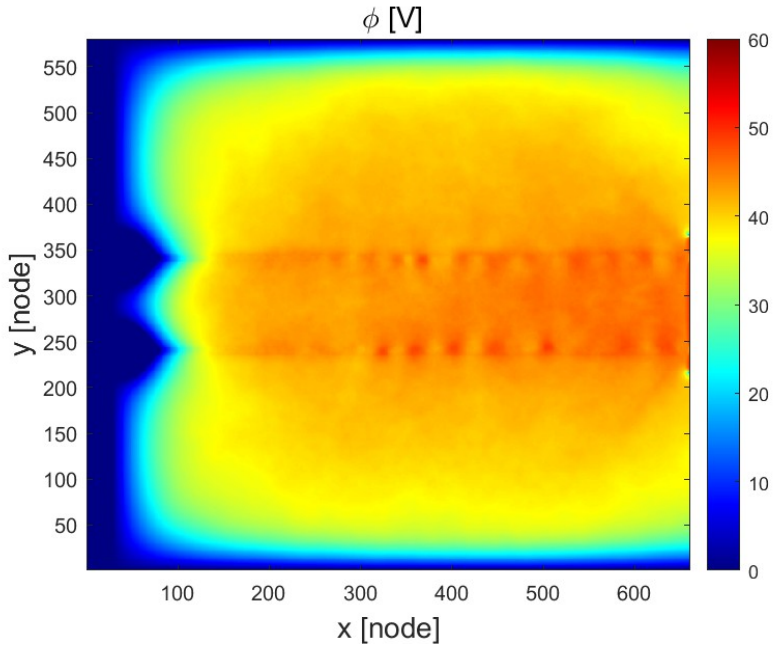

Figure 6.5: Potential map

From the graphs of figure 6.4 it is also possible to observe molecular H_2^+ ions compensating electrons and negative ions. Protons, atoms and H_3^+ ions occupy only a very small fraction of the entire beam composition. Moreover, the farther the profile from the grid, the higher the beam plasma density between the two beamlets.

6.3 B_α emission

Thanks to the PIC results shown in the previous section it is possible to find the maps for the B_α emission rates. To start, the processes in table 6.2 are considered. Since the population of H_3^+ is very low, processes involving H_3^+ dissociation are neglected.

#	σ	reaction	name	ref.	comment
1	σ_1	$\underline{e} + H_2 \longrightarrow \underline{e} + H + H(n=3)$	dissociative excitation	[20]	-
2	σ_2	$e + H_2^+ \longrightarrow H + H(n=3)$	dissociative recombination	[21]	-
3	σ_3	$\underline{e} + H_2^+ \longrightarrow \underline{e} + H^+ + H(n=3)$	dissociative excitation	[20]	-
4	σ_4	$\underline{H} + H_2 \longrightarrow \underline{H} + H + H(n=3)$	dissociative excitation	[18]	-
5	σ_5	$\underline{H} + H_2 \longrightarrow \underline{H}(3s) + H_2$	excitation	[18]	-
6	σ_6	$\underline{H} + H_2 \longrightarrow \underline{H}(3p) + H_2$	excitation	[18]	a)
7	σ_7	$\underline{H} + H_2 \longrightarrow \underline{H}(3d) + H_2$	excitation	[18]	a)
8	σ_8	$\underline{H^+} + H_2 \longrightarrow \underline{H^+} + H + H(n=3)$	dissociative excitation	-	b)
9	σ_9	$\underline{H^+} + H_2 \longrightarrow \underline{H}(3s) + H_2^+$	charge exchange	[18]	-
10	σ_{10}	$\underline{H^+} + H_2 \longrightarrow \underline{H}(3p) + H_2^+$	charge exchange	[18]	-
11	σ_{11}	$\underline{H^+} + H_2 \longrightarrow \underline{H}(3d) + H_2^+$	charge exchange	[18]	-
12	σ_{12}	$\underline{H^-} + H_2 \longrightarrow \underline{H^-} + H + H(n=3)$	dissociative excitation	-	b)
13	σ_{13}	$\underline{H^-} + H_2 \longrightarrow \underline{H}(3s) + e^- + H_2$	stripping	[19]	a)
14	σ_{14}	$\underline{H^-} + H_2 \longrightarrow \underline{H}(3p) + e^- + H_2$	stripping	[19]	a)
15	σ_{15}	$\underline{H^-} + H_2 \longrightarrow \underline{H}(3d) + e^- + H_2$	stripping	[19]	a)

Table 6.2: Reactions exploited to find the B_α emission rate

a) Same comment as table 3.3;
b) Since σ_8 and σ_{12} were not found in literature, they were arbitrarily taken equal to σ_4.

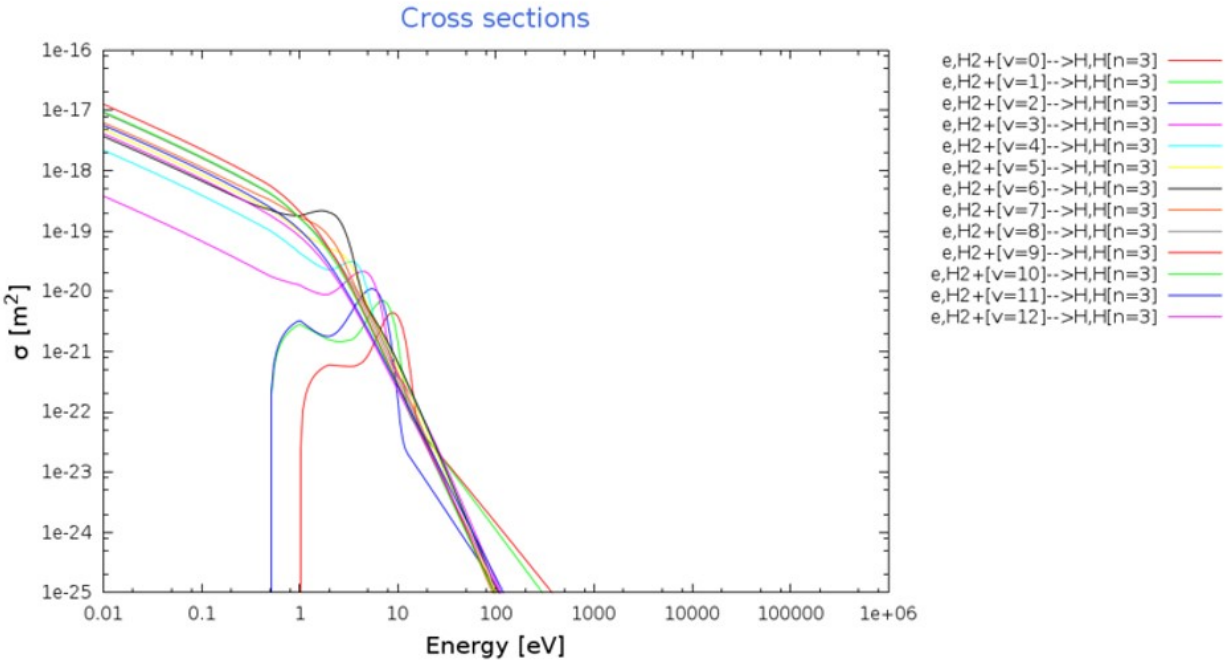

Figure 6.6: Dissociative recombination cross sections exploited to find σ_2. Other cross sections reported in table 6.2 can be found in the previous chapters

The emission rate maps can be found according to the following formulae

$$\frac{dn_e}{dt} = n_{H_2}\, n_e\, \sigma_1\, v_e + n_{H_2^+}\, n_e\, (\sigma_2 + \sigma_3)\, v_e \tag{6.8}$$

$$\frac{dn_H}{dt} = n_{H_2}\, n_H\, (\sigma_4 + \sigma_5 + \sigma_6 + \sigma_7)\, v_H \tag{6.9}$$

$$\frac{dn_{H^+}}{dt} = n_{H_2}\, n_{H^+}\, (\sigma_8 + \sigma_9 + \sigma_{10} + \sigma_{11})\, v_{H^+} \tag{6.10}$$

$$\frac{dn_{H^-}}{dt} = n_{H_2}\, n_{H^-}\, (\sigma_{12} + \sigma_{13} + \sigma_{14} + \sigma_{15})\, v_{H^-} \tag{6.11}$$

where n and v indicate the density and velocity maps for the different species and σ the cross sections of table 6.2. These four equations quantify the production rate of n=3 excited atoms induced by electrons, atoms, positive and negative ions respectively. The total contribution can be found as a sum of all the four contributions:

$$\frac{dn_{tot}}{dt} = \frac{dn_e}{dt} + \frac{dn_H}{dt} + \frac{dn_{H^+}}{dt} + \frac{dn_{H^-}}{dt} \tag{6.12}$$

The resulting maps are shown in figure 6.7 and the total contribution in figure 6.8

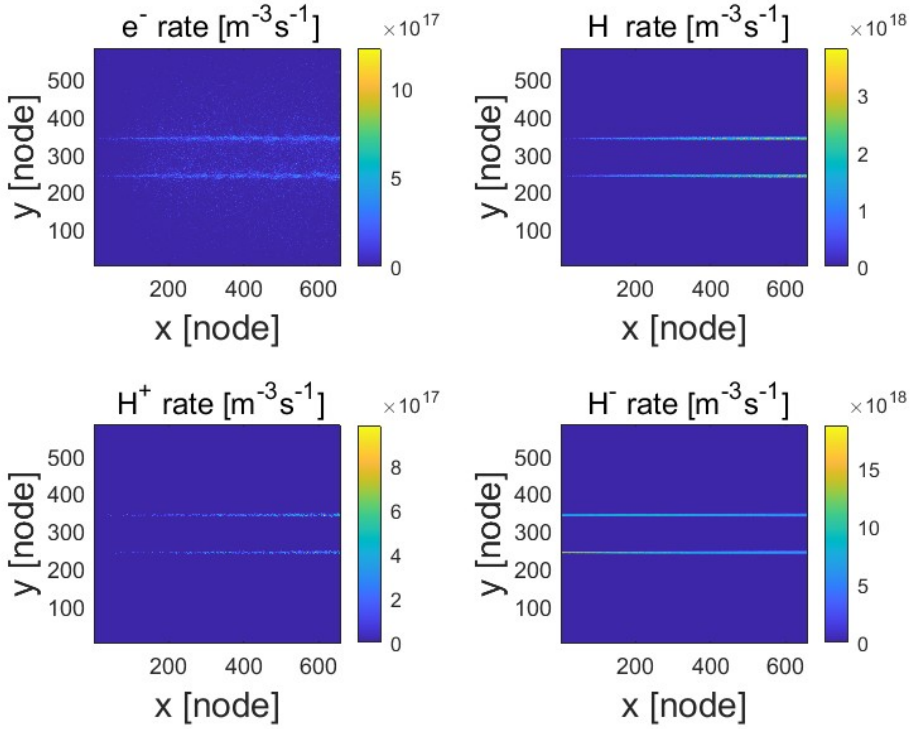

Figure 6.7: B_α emission rate maps.

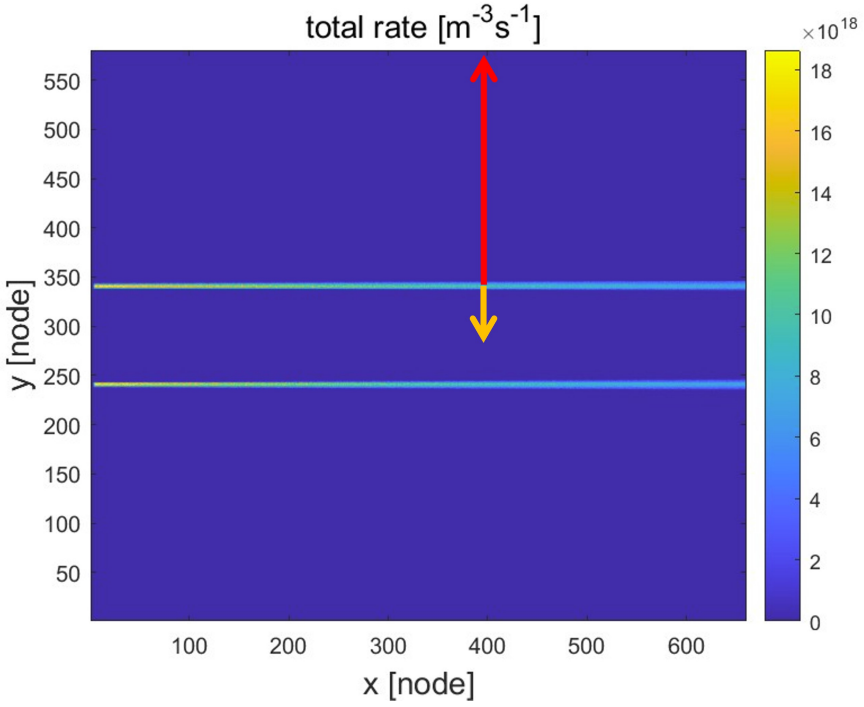

Figure 6.8: B_α total emission rate map. The red and yellow arrows point out how the beamlet radial profiles are obtained.

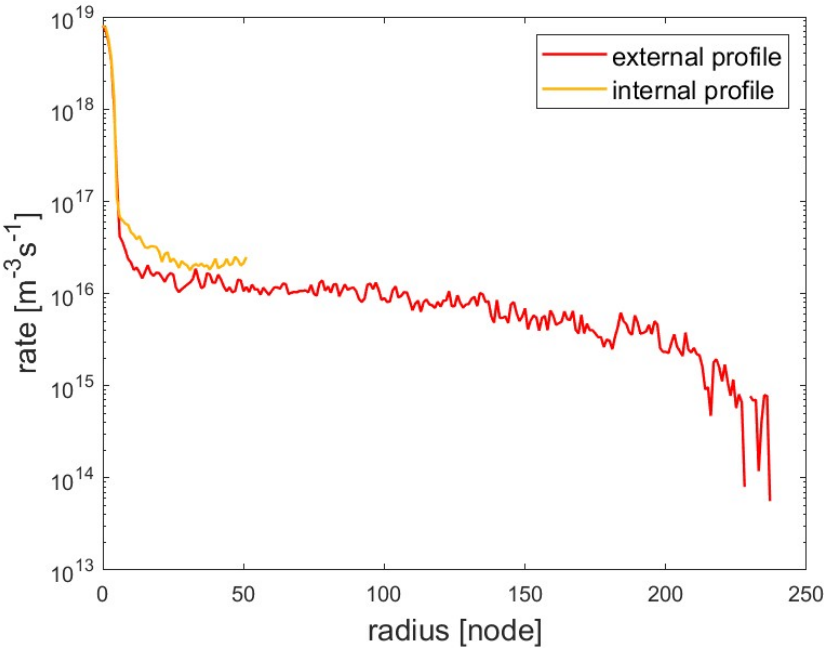

Figure 6.9: Radial profiles obtained from figure 6.8

From the total n=3 rate of figure 6.8 it is possible to find the internal and external radial profiles of figure 6.9: in particular, it can be observed that in the beamlet region the two profiles coincide but in the external region, as expected, the internal profiles turns out to be slightly larger than the external one due to the higher density of the beam plasma in the inter-beamlet region. However, due to the larger radial extension, for the next considerations only the external profile is considered.

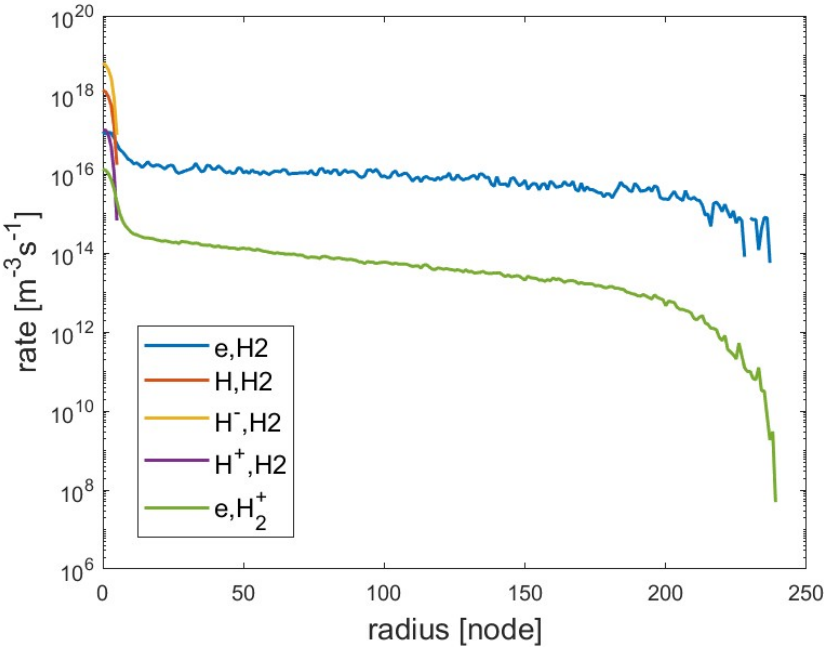

Figure 6.10: External radial profile components

Figure 6.10 shows the single contributions making up the external B_α emission rate profile: the contributions from atoms, positive and negative ions stay focused on the beamlet region, while only electrons impinging on H_2 or H_2^+ are able to produce light in the inter-beamlet region. This may be due to the fact that among slow particles (few eV) only electrons are capable of producing B_α light, according to this model.

6.4 Synthetic beam tomography

Thanks to the radial profile obtained in the previous section, it is possible to get the synthetic beam tomography spectra for the 28 beamlets the same way as section 5.5. The resulting spectra are reported in figures 6.11, 6.12 and 6.13.

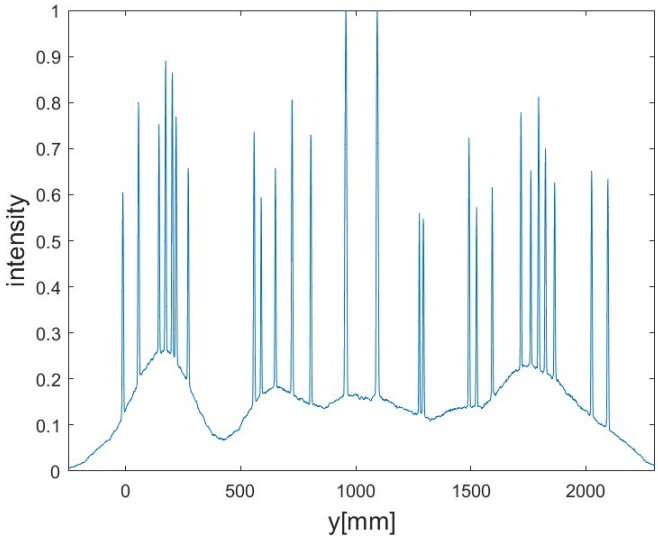

(a) PIC simulated spectrum

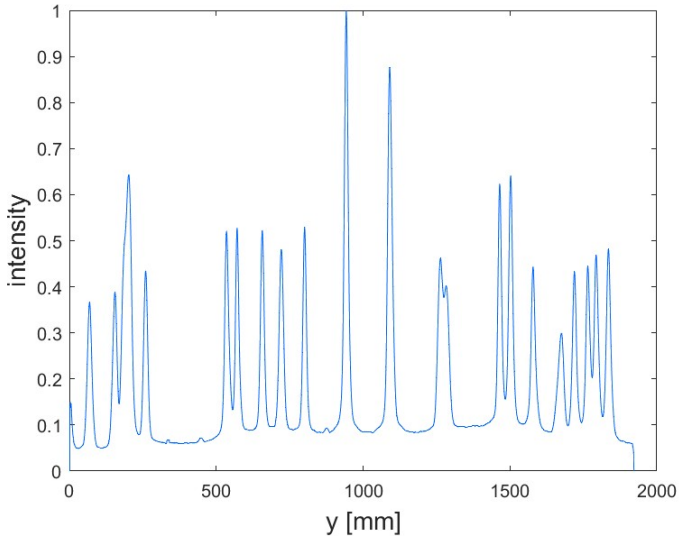

(b) Experimental findings

Figure 6.11: Beam tomography spectrum from camera B9 port 01.

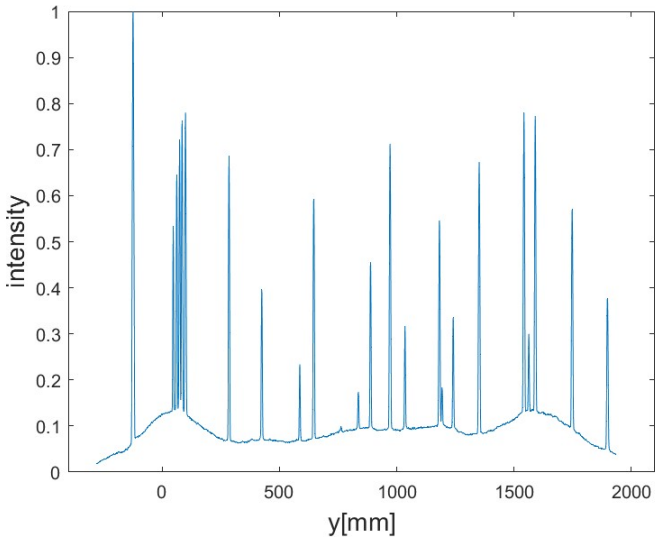

(a) PIC simulated spectrum

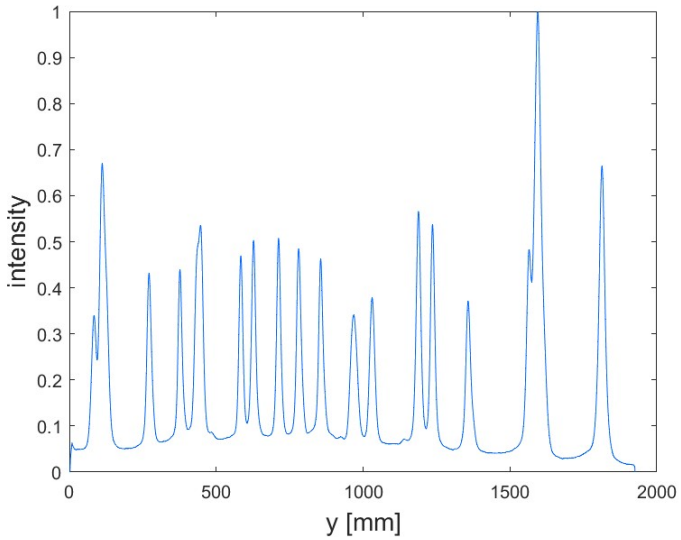

(b) Experimental findings

Figure 6.12: Beam tomography spectrum from camera B8 port 15.

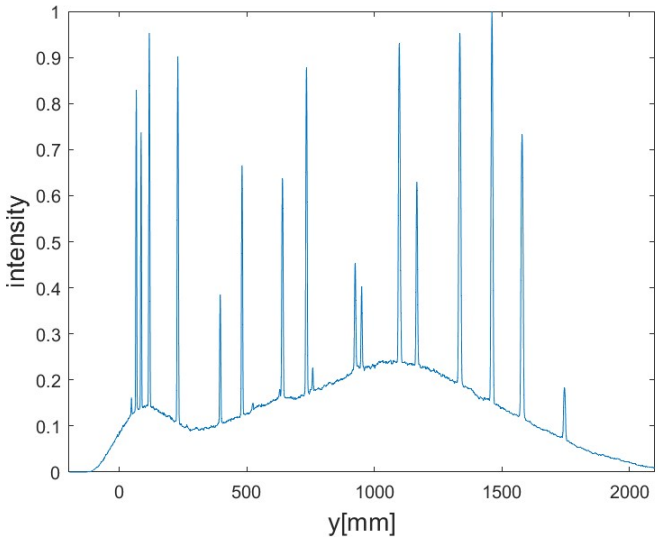

(a) PIC simulated spectrum

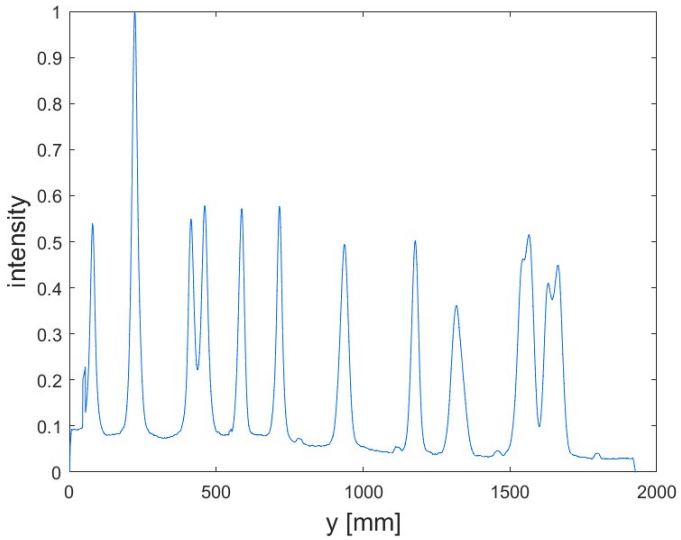

(b) Experimental findings

Figure 6.13: Beam tomography spectrum from camera B2 port 03.

First of all, as already shown in the previous chapter, the position of the peaks in the simulated spectrum matches the position of the experimental peaks; however, the width of the peaks is larger for the experimental findings.
This is in part due to the fact that in the synthetic spectrum the LoSs along which the integration is performed are simple geometric lines with no transversal dimension while, due to the finite size of the pixels on the cameras, even the solid angle covered by the LoSs must be considered. This implies that more photons are collected resulting in a peak enlargement.
However, the most important point on which this thesis work is based is the presence of the luminous background in the experimental spectrum. Unlike the results of the previous chapter, it is now clear the presence of light emitted in the region between the beamlets: only by including the transversal diffusion of the beam plasma it has been possible to explain the experimental evidence. Yet, the background is larger and not as uniform as in the experimental spectra. In particular, the closer the peaks, the higher the background. This may be due to the superposition of the single beamlet profiles arranged as in figure 5.10. Moreover, the radial profile is obtained in the presence of two beamlets only, so, the result is already approximated from the beginning. For example, the presence of more beamlets might increase the beam plasma density and further enlarge the extension of the radial profile. The best results would have been obtained directly with a 3D PIC code; however, due to the limited dimension of the code in use, this was not possible. Nonetheless, in very first quantitative approximation, the results seems to be satisfactory. As figure 6.10 shows, the background seems only due to electrons impinging on H_2 and H_2^+, while the contribution to light emission by neutral atoms, positive or negative ions remains concentrated along the beamlet axis. More specifically, due to the larger density of the H_2 gas, electrons impinging on H_2 provide a larger contribution to B_α than electrons impinging on H_2^+.

6.5 Synthetic BES

From the data obtained with the *gppic* code it is also possible to reproduce the BES spectrum. To accomplish with this task, the production rate maps for fast (beam) and slow (plasma) n=3 excited atoms are found according to the following equations

$$\frac{dn_{plasma}}{dt} = n_{H_2}\, n_e\, \sigma_1\, v_e + n_{H_2^+}\, n_e\, (\sigma_2 + \sigma_3)\, v_e + n_{H_2}\, n_H\, \sigma_4\, v_H + \\ + n_{H_2}\, n_{H^+}\, \sigma_8\, v_{H^+} + n_{H_2}\, n_{H^-}\, \sigma_{12}\, v_{H^-} \tag{6.13}$$

$$\frac{dn_{beam}}{dt} = n_{H_2}\, n_H\, (\sigma_5 + \sigma_6 + \sigma_7)\, v_H + n_{H_2}\, n_{H^+}\, (\sigma_9 + \sigma_{10} + \sigma_{11})\, v_{H^+} + \\ + n_{H_2}\, n_{H^-}\, (\sigma_{13} + \sigma_{14} + \sigma_{15})\, v_{H^-} \tag{6.14}$$

where σ are the cross sections of table 6.2, n and v the atom density and velocity maps. Starting from the velocity maps it is possible to find the maps for the wavelength λ defined as

$$\lambda' = \lambda_0 \frac{1 - \beta \cos\alpha}{\sqrt{1-\beta^2}} = \lambda_0 \frac{1 - \beta\, \boldsymbol{v}\cdot\boldsymbol{k}}{\sqrt{1-\beta^2}} \qquad \beta = \frac{v}{c} \tag{6.15}$$

where c is the speed of light, $\lambda_0 = 656.28\,\text{nm}$ the nominal wavelength for the B_α transition and α the angle between the velocity of the macroparticle represented by the velocity versor $\boldsymbol{v}$ and the versor $\boldsymbol{k}$ indicating the direction of the detected photons.

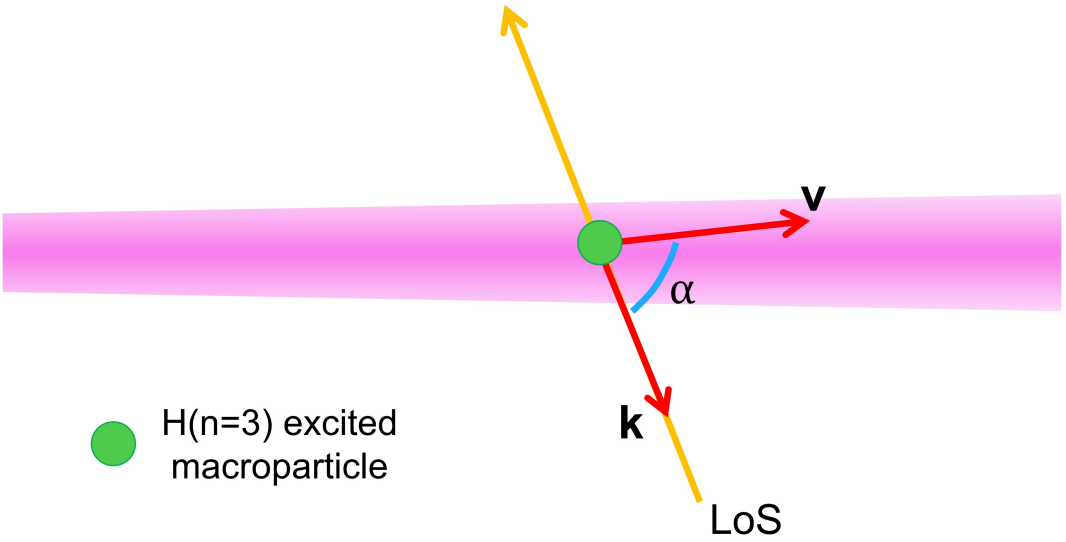

Figure 6.14: BES line of sight

To get the BES spectrum a single line of sight tilted 75° with respect to the horizontal axis is considered and discretized in many arbitrary steps. The LoS passes over the density and the λ maps as represented in figure 6.15.

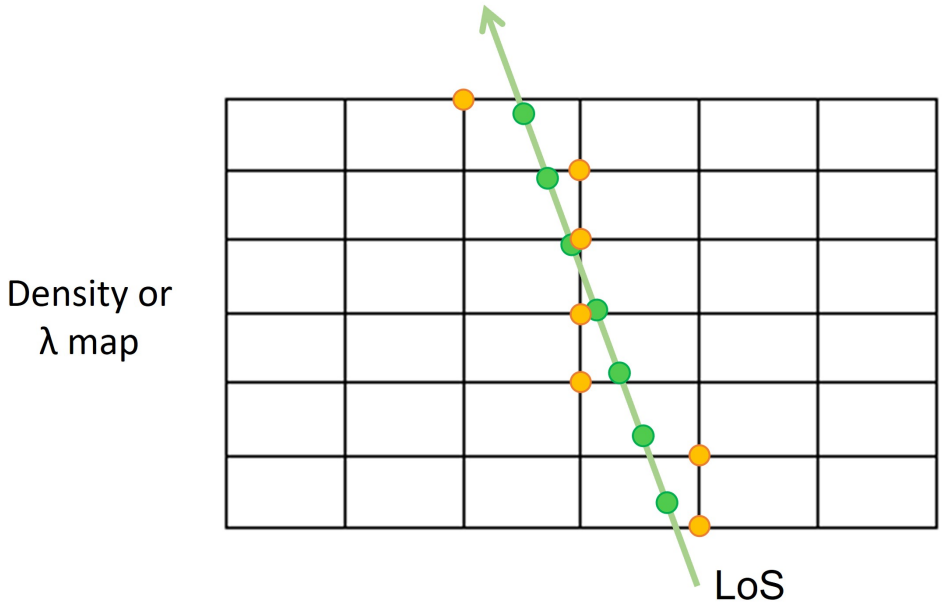

Figure 6.15: LoS discretization on the wavelength and density maps

For each LoS step, couples $(dn/dt,\ \lambda)$ for both beam and plasma n=3 excited atoms are collected according to the value of the rate dn/dt and wavelength λ assumed by the closest node. All the collected couples for both beam and plasma excited atoms are exploited to construct the BES spectrum as a weighted hystogram where the entries are the wavelengths λ and their weight is detemined by the B_α emission rate. The resulting BES spectrum for a 48 keV beam with 30 mPa H_2 pressure is shown in figure 6.16 along with the experimental spectrum.

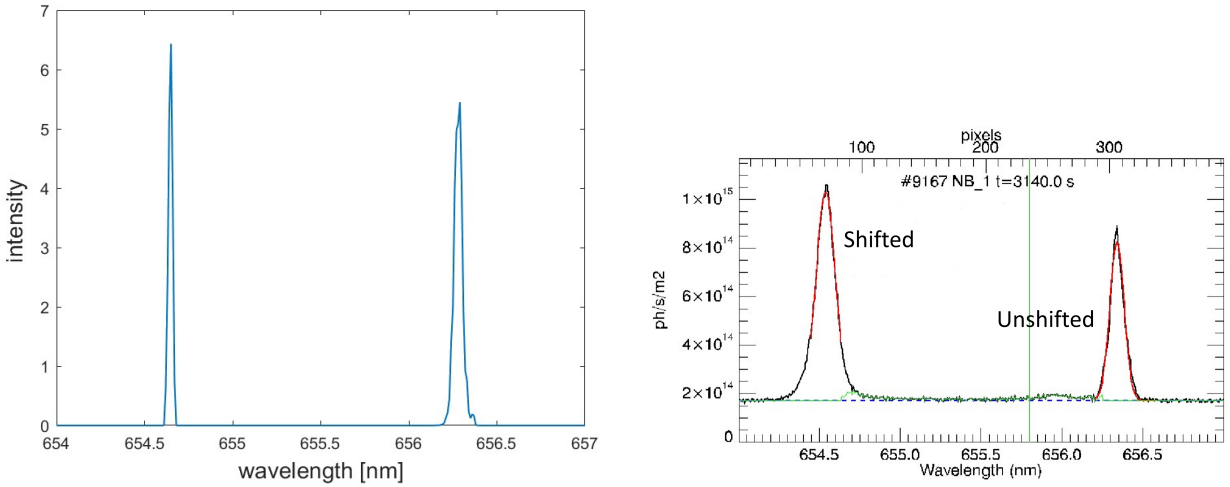

(a) BES simulated spectrum

(b) BES experimental spectrum

Figure 6.16: BES spectrum for a 48 keV beam at 30 mPa

The same procedure is also applied to a 24 keV beam keeping the other parameters un-

changed:

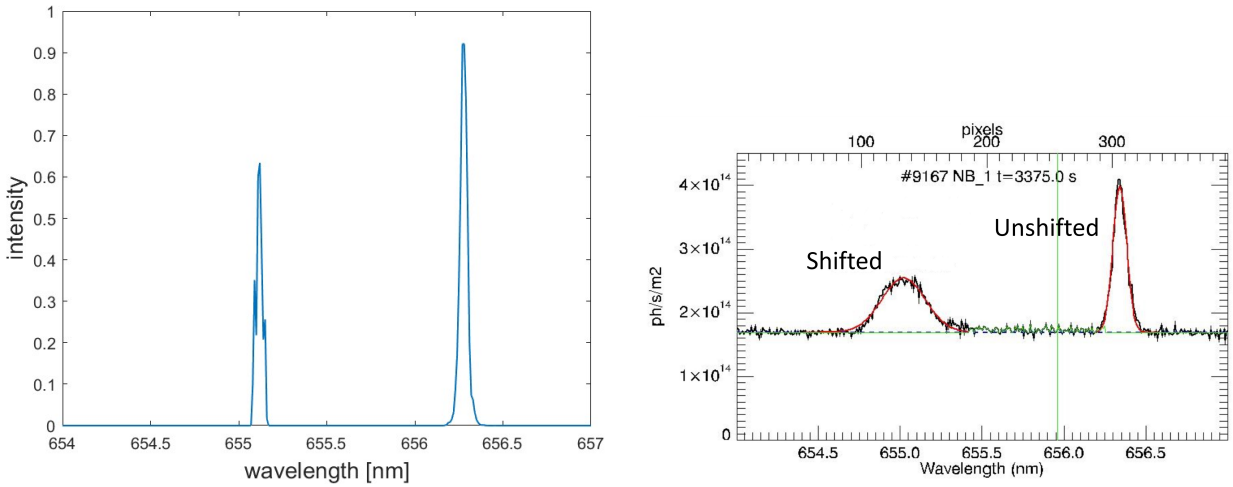

(a) BES simulated spectrum

(b) BES experimental spectrum

Figure 6.17: BES spectrum for a 24 keV beam at 30 mPa

spectrum	shifted peak area	unshifted peak area
48 keV experimental	66%	34%
48 keV simulated	40%	60%
24 keV experimental	54%	46%
24 keV simulated	40%	60%

Table 6.3: Area in % occupied by each beamlet in the experimental and simulated spectra

From the graphs of figures 6.16 and 6.17 it is possible to notice that the simulated spectrum reproduces the correct position of the peaks on the wavelength axis but not their heights and widths: in fact, by looking at table 6.3 showing the area in % occupied by the shifted and unshifted peaks, it can be observed that the areas occupied by the simulated peaks are different from the ones obtained from the corresponding simulated spectra. One of the reason may lie on the fact that the beamlets are generated with no divergence; as a consequence, the simulated peaks result to be thinner than the experimental ones [30] [31].

6.6 Conclusion of the chapter

The purpose of this chapter was to reproduce some of the SPIDER experimental findings measured during the 2021 experimental campaign, in particular from beam tomography and BES. Concerning the former, despite being not as uniform as that observed in the experimental findings, the luminous background was observed even in the simulated spectra

and, according to the model, it is produced mostly by electrons impinging on H_2. However, a more detailed investigation will be the aim of future works. Instead, regarding BES, apart from the peak width, synthetic measurements seem to reproduce the correct position of the peaks in the wavelength axis but not their height and their width. Even in this case, attempts to improve the simulated BES spectra including also peak broadening effects like beam divergence are left to future works.

Chapter 7

Conclusions

The purpose of this thesis work is the investigation of beam transport, in order to provide possible explanations for the unexpected experimental findings concerning the optical emission diagnostics of the SPIDER beam obtained in the last experimental campaign. In particular, the results of beam tomography and beam emission spectroscopy are considered. Both diagnostics measure the Balmer α light spontaneously emitted during the beam propagation because of the interaction of the latter with the background gas. Concerning beam tomography, an almost uniform luminous background was observed also in regions where beamlets are not intercepted by the lines-of-sight, which could not be justified in terms of beam-related processes; regarding Beam Emission Spectroscopy, it was necessary to investigate the reasons behind the features of the two peaks observed in the spectra and particularly their relative intensities.
Due to the exploratory nature of this investigation, several numerical models have been developed and are described in this thesis work to understand which processes are involved in the beam propagation and how much they contribute to light emission: for example it was possible to obtain the spatial variation of the beam composition during its propagation due to the interaction with the H2 background gas, also by analysing the propagation of different kinds of electron populations. Yet, this was not sufficient to justify the significant light emission detected in between the beamlets: in fact, this result could only be explained by using the Particle-In-Cell (PIC) code, which is capable of modelling also the beam plasma formation and the transverse diffusion of positive ions and electrons from the beamlets. In this way, despite being not as uniform as in the experimental results, the luminous background was finally reproduced in the synthetic beam tomography spectrum, and it was found to be mostly due to beam plasma electrons impinging on the H2 gas. Concerning instead the BES spectrum, it was possible to obtain both peaks at the correct wavelengths, although the results in terms of collected light are still not satisfactory.
Possible future investigations regarding the analysis of beam tomography spectra may involve the employment of a cylindrical coordinates in the PIC code to reproduce the beam propagation and to see if the width of the peaks enlarges or if the luminous background assumes a more uniform shape. Alternatively, simpler diffusion models could be developed to deal with both the three-dimensional nature of the problem and the large extension of the domain, which would be rather complex to treat numerically with a PIC code. As for the BES findings, the broadening effects on the peak could be introduced,

as this might improve the matching between the synthetic and experimental spectra.

Appendix A

Effects of dissociated atoms on the propagation

In chapter 3, while dealing with the different space evolution of the different species, it was assumed that the interaction of the beam with atoms originated from the dissociation of the H_2 gas could be neglected. Yet, no evidence to support that assumption was provided. The aim of this section is to quantify the amount of dissociated atoms and whether their contribution can actually be neglected. To prove it, a single beamlet of radius $R_{beamlet} = 7\,mm$ approximated as a perfect cylinder is considered.

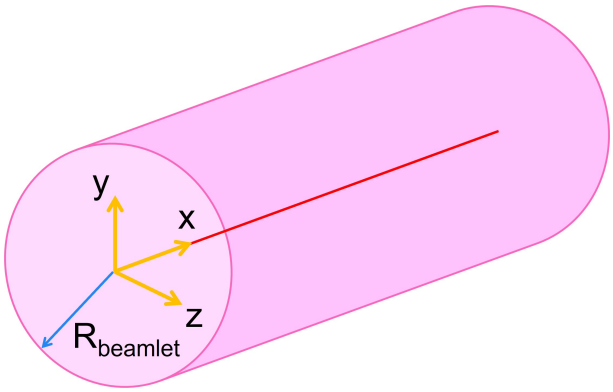

Figure A.1: Cylindrical approximation of a single SPIDER beamlet

Beamlet particles propagate along the drift region filled with molecular hydrogen at a pressure of $p = 0.03\,Pa$. The density n_H of dissociated atoms can either vary in time due to generation of atoms by H_2 dissociation or loss due to atoms leaving the beamlet region by radial spreading

$$\frac{dn_H}{dt} = \left.\frac{dn_H}{dt}\right|_{gain} - \left.\frac{dn_H}{dt}\right|_{loss} = n_{H_2}\,\overline{\sigma}_{dis}\,\Gamma_{beam} - \frac{n_H}{\langle\tau\rangle} \tag{A.1}$$

where n_{H_2} is the background gas density, Γ_{beam} the beam flux, n_H the unknown atom density, $\langle\tau\rangle$ the average time neutral atoms take to leave the beamlet and $\overline{\sigma}_{dis}$ the effective dissociation cross section. At equilibrium, the time derivative term in the left hand side vanishes and n_H can be found accordingly:

$$n_{H_2}\,\overline{\sigma}_{dis}\,\Gamma_{beam} - \frac{n_H}{\langle\tau\rangle} = 0 \qquad \longrightarrow \qquad n_H = n_{H_2}\,\overline{\sigma}_{dis}\,\Gamma_{beam}\,\langle\tau\rangle \tag{A.2}$$

To find the atom density n_H, the drift region is firstly discretized in many arbitrary steps of length dx as done in the previous chapter, so that the atom density at the i-th step along the drift region can be expressed as

$$n_H(i) = n_{H_2}\,\overline{\sigma}_{dis}(i)\,\Gamma_{beam}(i)\,\langle\tau\rangle \tag{A.3}$$

To get to the result, all the four factors in the right hand side of the equation must be computed. To start, n_{H_2} is simply found from the gas pressure $p = 0.03\,\mathrm{Pa}$ along the drift region. Concerning $\overline{\sigma}_{dis}$, it can be defined as

$$\overline{\sigma}_{dis} = \frac{\sigma_-\,\Gamma^{H^-}(i) + \sigma_0\,\Gamma^{H}(i) + \sigma_+\,\Gamma^{H^+}(i) + \sigma_{se}\,\Gamma^{se}(i)}{\Gamma^{H^-}(i) + \Gamma^{H}(i) + \Gamma^{H^+}(i) + \Gamma^{se}(i)} \tag{A.4}$$

with

$$\Gamma_{beam} = \Gamma^{H^-}(i) + \Gamma^{H}(i) + \Gamma^{H^+}(i) + \Gamma^{se}(i) \tag{A.5}$$

where Γ^{H^-}, Γ^{H}, Γ^{H^+} and Γ^{se} are the beam fluxes of figure 3.4, whereas σ_-, σ_0, σ_+ and σ_{se} the dissociation cross sections of figure A.2 corresponding to the reactions of table A.1

#	σ	reaction	name	ref.	comment
1	σ_1	$\underline{e}^- + H_2 \longrightarrow \underline{e}^- + H(1s) + H(1s)$	dissociative excitation	[20]	-
2	σ_2	$\underline{e}^- + H_2 \longrightarrow \underline{e}^- + H(1s) + H(2s)$	dissociative excitation	[20]	-
3	σ_3	$\underline{e}^- + H_2 \longrightarrow \underline{e}^- + H(2p) + H(2s)$	dissociative excitation	[20]	-
4	σ_4	$\underline{e}^- + H_2 \longrightarrow \underline{e}^- + H(1s) + H(n=3)$	dissociative excitation	[20]	-
5	σ_5	$\underline{H}^+ + H_2 \longrightarrow \underline{H}^+ + H + H(2s)$	dissociative excitation	[18]	-
6	σ_6	$\underline{H}^+ + H_2 \longrightarrow \underline{H}^+ + H + H(2p)$	dissociative excitation	[18]	-
7	σ_7	$\underline{H} + H_2 \longrightarrow \underline{H} + H + H(2s)$	dissociative excitation	[18]	a)
8	σ_8	$\underline{H} + H_2 \longrightarrow \underline{H} + H + H(2p)$	dissociative excitation	[18]	a)
9	σ_9	$\underline{H} + H_2 \longrightarrow \underline{H} + H + H(n=3)$	dissociative excitation	[18]	-
10	σ_{se}	$\underline{e}^- + H_2 \longrightarrow \underline{e}^- + H + H$	dissociative excitation	-	b)
11	σ_+	$\underline{H}^+ + H_2 \longrightarrow \underline{H}^+ + H + H$	dissociative excitation	-	c)
12	σ_0	$\underline{H} + H_2 \longrightarrow \underline{H} + H + H$	dissociative excitation	-	d)
13	σ_-	$\underline{H}^- + H_2 \longrightarrow \underline{H}^- + H + H$	dissociative excitation	-	e)

Table A.1: Dissociative excitation reactions

Comments to table A.1:

a) Since σ_7 and σ_8 are not defined for energies higher than 20 keV, the cross section validity is arbitrarily extended up to 100 keV following the same asymptotic behaviour as σ_9, as shown with dashed lines in figure A.2;

b) σ_e is obtained by summing σ_1, σ_2, σ_3 and σ_4, namely $\sigma_e = \sigma_1 + \sigma_2 + \sigma_3 + \sigma_4$;
c) σ_+ is obtained by summing σ_5 and σ_6, namely $\sigma_+ = \sigma_5 + \sigma_6$;
d) σ_0 is obtained by summing σ_7, σ_8 and σ_9, namely $\sigma_0 = \sigma_7 + \sigma_8 + \sigma_9$;
e) Since cross sections values for this specific interaction were not found in literature, it was arbitrarily assumed that σ_- was equal to σ_0, namely $\sigma_- = \sigma_0$

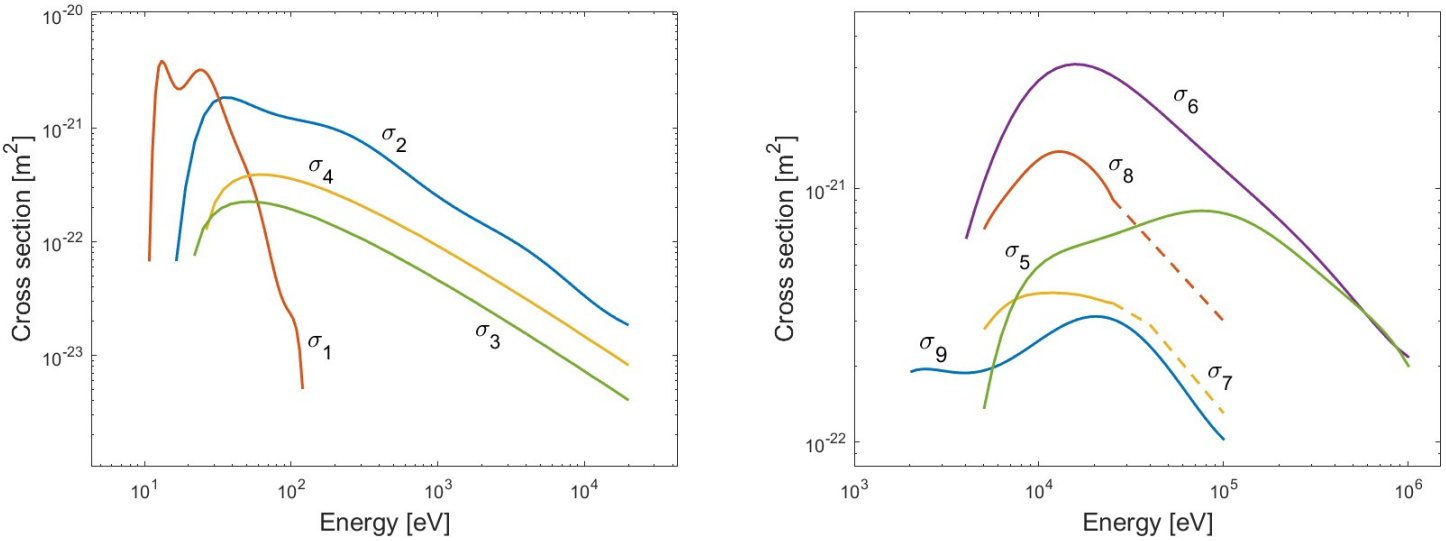

(a) H_2 dissociative excitation by electron impact

(b) H_2 dissociative excitation by atom or ion impact

Figure A.2: Dissociative excitation cross sections

By considering the interaction in table A.1, equation A is modified as follows

$$n_H(i) = n_{H_2}\left[\sigma_-(E_b)\,\Gamma^{H^-}(i) + \sigma_0(E_b)\,\Gamma^{H}(i) + \sigma_+(E_b)\,\Gamma^{H^+}(i) + \sigma_e(E_{se})\,\Gamma^{se}(i)\right]\langle\tau\rangle \quad \text{(A.6)}$$

where the values for σ_+, σ_0, σ_- are found at the beam energy $E_b = 48\,\text{keV}$ while σ_{se} at the stripped electron energy $E_{se} \sim 26\,\text{eV}$.
It only remains to compute the average time $\langle\tau\rangle$ that dissociated atoms take to reach the beamlet edge. To accomplish this task a Montecarlo simulation written in MATLAB will be exploited.
A cylindrical beamlet propagating along the x axis, as the one shown in figure A.1, is considered. Due to the cylindrical symmetry along the x axis, the problem can be reduced from 3D in the xyz space to 2D on the yz plane as in figure A.3 where the transversal section of the beamlet is drawn.

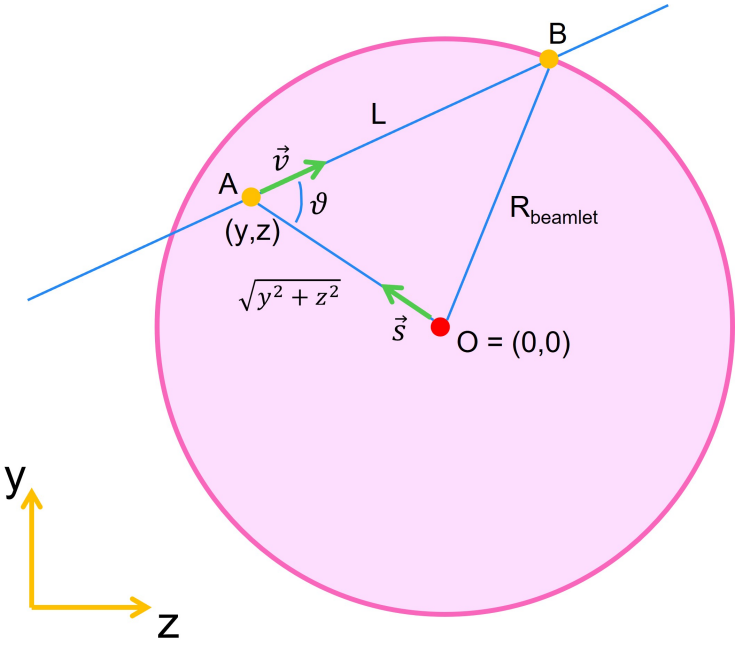

Figure A.3: Beamlet section on the yz plane

A dissociated atom is generated in a given point A= (y, z) inside the circular beamlet section. In particular, the position of A is determined exploiting a bi-dimensional gaussian distribution centred on the beamlet axis O and having a third of the beamlet radius as standard deviation. Concerning their energy, typically dissociated atoms are produced with energies below 10 eV, with value depending on the transition occurring in the Franck-Condon region of the H_2 potential diagram before the molecule is eventually dissociated. Thus, to determine the energy E_H of the dissociated atom in eV, a random number in the interval [0,10] is drawn from a uniform distribution. The magnitude of the velocity vector can be found accordingly as

$$v_H = \sqrt{\frac{2eE_H}{m_H}} \tag{A.7}$$

where $e = 1.6 \cdot 10^{-19}$ C is the elementary charge and $m_H = 1.67 \cdot 10^{-27}$ kg the hydrogen atom mass. Since the energy and angular distributions for dissociated atoms were not found in literature, the dissociated atom energy E_{yz} on the yz plane was for simplicity assumed to be as small as 20% of the entire atom energy E_H:

$$E_{yz} = 0.2 \cdot E_H \qquad \longrightarrow \qquad v_{yz} = \sqrt{\frac{2eE_{yz}}{m_H}} \tag{A.8}$$

this choice is made in such a way as to reproduce the fact that atoms mostly move along the beamlet axis with a small deflection determined by E_{yz}, accounting for the radial spreading of the atoms towards the beamlet edge where they are eventually lost. Finally, the velocity direction indicated by the versor $\hat{v}$ is randomly determined with equal probability in any direction around the generation point A.
To further simplify the model, since the mean free path λ for elastic collision of 0-10 eV

neutral atoms on H_2 is on the order of 1 m, it can be assumed that the dissociated atom, once generated, travels towards the beamlet edge following a straight line trajectory at uniform velocity without any other interaction occurring. The distance travelled by the atom before exiting the beamlet can then be calculated referring to figure A.3 and exploiting the cosine theorem:

$$\overline{OB}^2 = \overline{OA}^2 + \overline{AB}^2 - 2\,\overline{OA}\,\overline{AB}\cos\theta \qquad \text{where} \qquad \cos\theta = \hat{\boldsymbol{v}} \cdot \hat{\boldsymbol{s}} \tag{A.9}$$

where $\hat{\boldsymbol{v}}$ is the versor specifying the trajectory of the moving atom, $\hat{\boldsymbol{s}}$ the versor from the origin O pointing at the position where the atom is generated and, finally, θ the angle between these two versors. Rearranging:

$$\overline{AB}^2 - (2\,\overline{OA}\cos\theta)\,\overline{AB} + (\overline{OA}^2 - \overline{OB}^2) = 0 \tag{A.10}$$

replacing the known quantities and changing name to $\overline{AB}$ as L:

$$L^2 - (2\sqrt{y^2+z^2}\;\hat{\boldsymbol{v}} \cdot \hat{\boldsymbol{s}})\;L + (y^2 + z^2 - R^2_{beamlet}) = 0 \tag{A.11}$$

The distance L travelled to exit the beamlet is found by solving this second order equation and taking the solution corresponding to the positive direction of the atom velocity versor. Once L is found, the time τ the hydrogen atom takes to exit the beamlet can be found as

$$\tau = \frac{L}{v_{yz}} \tag{A.12}$$

By iterating over a large number of atoms, two histograms for L and τ can be obtained.

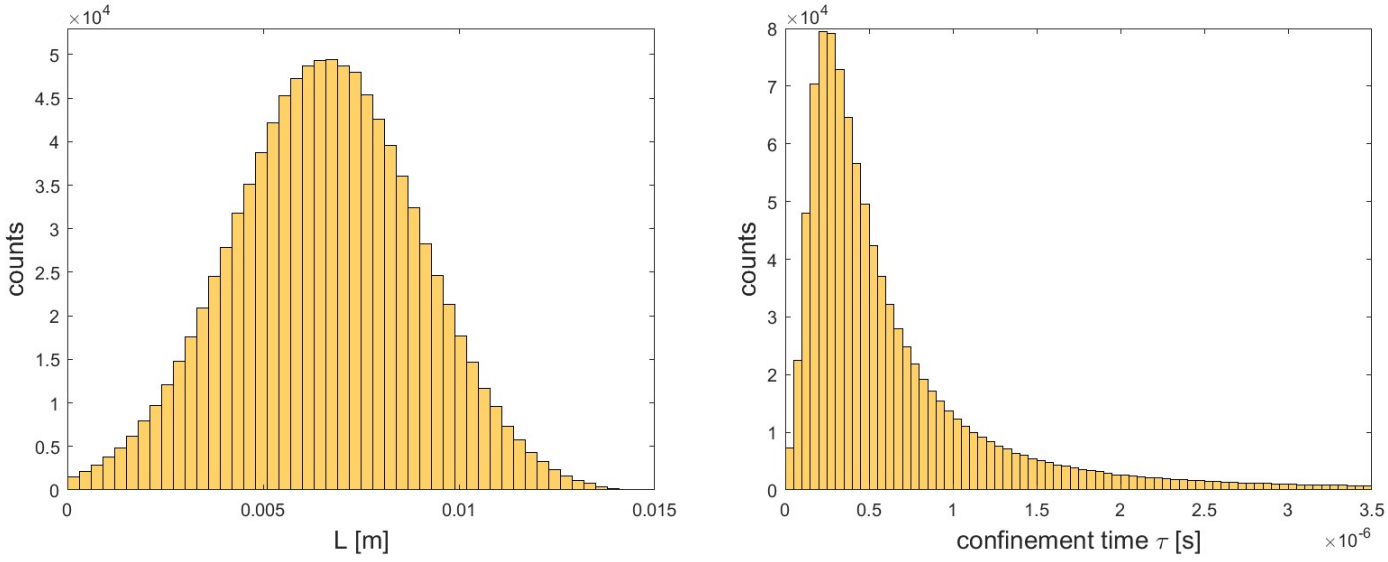

Figure A.4: L and τ distributions

From the two histograms of figure A.4 it is possible to find out both the average length $\langle L \rangle = 6.6\,\text{mm}$ and average time $\langle \tau \rangle = 0.8\,\mu\text{s}$ as a weighted average using the bin height as weight. By replacing $\langle \tau \rangle$ in A, the dissociated atom density profile is obtained:

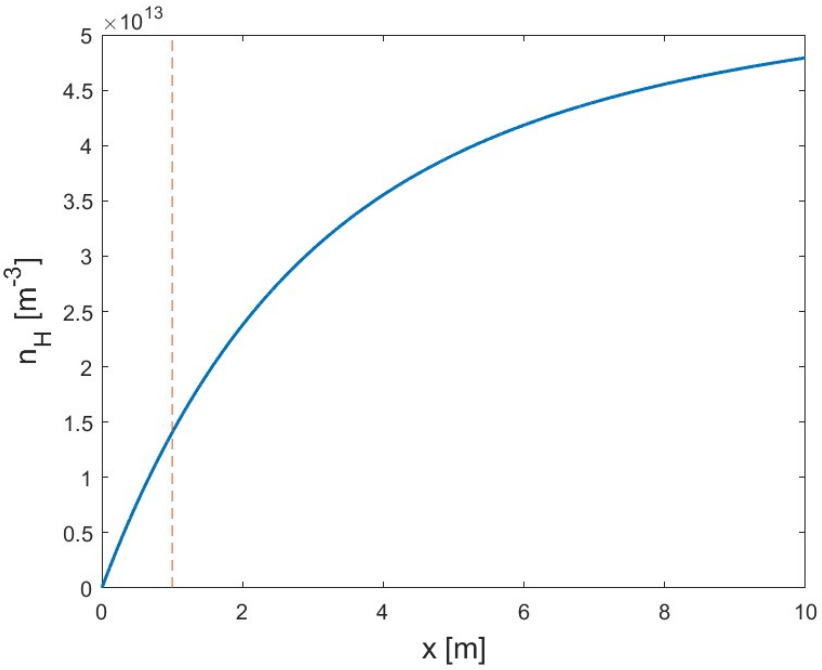

Figure A.5: Background hydrogen atom density profile

More specifically, figure A.5 shows the density n_H of background hydrogen atoms for the single beamlet as a function of the distance x travelled by the beam along the drift region. It can be observed that for $x < 1\,\mathrm{m}$, namely within the SPIDER drift region length, n_H is on the order of $10^{13}\,\mathrm{m}^{-3}$. Moreover, since $n_{H_2} = 7.2 \cdot 10^{18}\,\mathrm{m}^{-3}$, the resulting dissociation fraction for a single beamlet yields

$$f_{single\,beamlet} = \frac{n_H}{n_H + n_{H_2}} \sim 10^{-6} \div 10^{-5} \tag{A.13}$$

Therefore, for a single beamlet, the fraction of dissociated hydrogen atoms is utterly negligible with respect to the H_2 density. Yet, this result holds for a single beamlet: what if, instead, the entire SPIDER beam composed of 1280 beamlets was considered? In this case, atoms exiting the beamlet where they originated enter the surrounding beamlets, thus they are lost only if they exit the full beam section. Since it would be too complicated to model all the 1280 beamlets, a coarse-grained approach will be exploited to compute the fraction f of dissociated atoms, in particular, relying on the beamlet pattern of figure A.6. In that case, the typical length scale of the system is given by $\widetilde{L} \sim 1\,\mathrm{m}$. Considering that the atom energy on the yz plane is on the order of 1 eV, the typical time then yields:

$$\widetilde{\tau} = \frac{\widetilde{L}}{v_{yz}} \sim 10^{-4}\,s \tag{A.14}$$

By replacing it in A, the density of dissociated atoms becomes $n_H \sim 10^{15}\,\mathrm{m}^{-3}$. Hence:

$$f_{entire\,beam} = \frac{n_H}{n_H + n_{H_2}} \sim 10^{-4} \div 10^{-3} \tag{A.15}$$

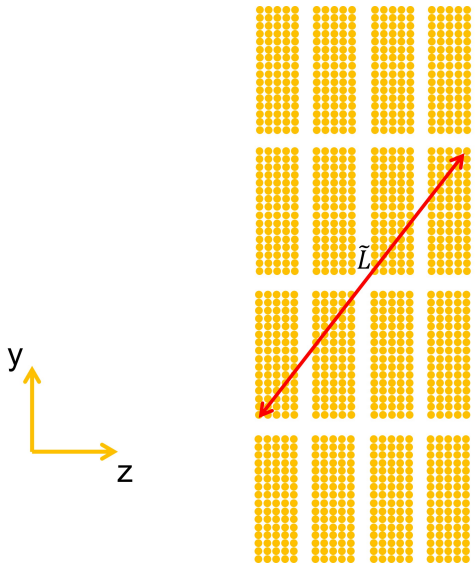

Figure A.6: Accelerator column apertures

The amount of dissociated atoms is still negligible compared to the H_2 density, therefore the initial assumption to neglect the interaction of the beam with the dissociated atoms is well posed in both the single and the multi-beamlet cases.

Bibliography

[1] H. Ritchie, M. Roser, *Electricity mix*, Our World in data, https://ourworldindata.org/electricity-mix

[2] ITER organization, https://www.iter.org/

[3] EUROfusion organization, https://www.euro-fusion.org/

[4] Consorzio RFX, https://www.igi.cnr.it/

[5] Y. Kazakov, D. Van Eester, J. Ongena, *Plasma heating in present-day and future fusion machines* Laboratory for Plasma Physics, LPP-ERM/KMS, EUROfusion Consortium Member, Brussels, Belgium

[6] Giovanni Manfredi, Fabrice Valsaque, *Plasma-wall transition and sheath formation.*, Le Vide, Société française duvide, 2002, 306 (4/4), pp.810-835. hal-03313380

[7] V. Candeloro, *Modelling of plasma expansion and interpretation of measured profiles in a negative ion source*, Master Degree thesis

[8] G. Chitarin, G. Serianni, V. Toigo, et al., *Start of SPIDER operation towards ITER neutral beams* AIP Conference Proceedings 2052, 030001 (2018); https://doi.org/10.1063/1.5083729

[9] P. Sonato et al., *The ITER full size plasma source device design* Fusion Engineering and Design, Volume 84, Issues 2–6, 2009, Pages 269-274, ISSN 0920-3796, https://doi.org/10.1016/j.fusengdes.2008.11.095

[10] R. Pasqualotto, G. Serianni, P. Sonato, et al., *Diagnostics of the ITER neutral beam test facility*, Rev. Sci. Instrum. 83, 02B103 (2012); https://doi.org/10.1063/1.3662017

[11] D. Marcuzzi et al., *Detail design of the beam source for the SPIDER experiment*, Fusion Engineering and Design Volume 85, Issues 10–12, December 2010, Pages 1792-1797

[12] M. Zaupa et al., *SPIDER beam dump as diagnostic of the particle beam*, Rev. Sci. Instrum. 87, 11D415 (2016); https://doi.org/10.1063/1.4958906

[13] M. Ugoletti et al., *First results of SPIDER beam characterization through the visible tomography*, Fusion Engineering and Design 169 (2021) 112667

[14] M. Ugoletti, *Beam physics via tomographic diagnostics*, PhD thesis

[15] N. Fonnesu et al., *Tomographic reconstruction of the beam emissivity profile in the negative ion source NIO1*, 2016 Nucl. Fusion 56 126018

[16] G. Serianni et al., *Neutralisation and transport of negative ion beams: physics and diagnostics*, 2017 New J. Phys. 19 045003

[17] M. Barbisan et al., *Beam emission spectroscopy studies in a H^-/D^- beam injector*, PhD thesis

[18] C.F. Barnett, *Collisions of H, H_2, He and Li atoms and ions with atoms and molecules*, Atomic data for fusion volume 1

[19] J. Geddes et al., *Formation of excited hydrogen atoms in electron detachment collisions by 3-25 keV H^- ions*, 1981 J. Phys. B: Atom. Mol. Phys. 14 4837

[20] R.K. Janev, *Elementary Processes in Hydrogen-Helium Plasmas, Cross Sections and Reaction Rate Coefficients*

[21] R.K. Janev at al. *Collision Processes in Low-Temperature Hydrogen Plasmas*

[22] R. Pasqualotto et al., *Design of a visible tomography diagnostic for negative ion RF source SPIDER*, Fusion Engineering and Design, Volume 169, 2021, 112667, ISSN 0920-3796, https://doi.org/10.1016/j.fusengdes.2021.112667

[23] National Institute of Standards and Technology (NIST), https://physics.nist.gov/

[24] V. Vahedi, M. Surendra, *A Monte Carlo collision model for the particle-in-cell method: applications to argon and oxygen discharges*, Computer Physics Communications 87 (1995) 179-198ù

[25] J-S Yoon et al., *Cross Sections for Electron Collisions with Hydrogen Molecules*, J. Phys. Chem. Ref. Data 37, 913 (2008); https://doi.org/10.1063/1.2838023

[26] M. G. Menendez and M. M. Duncan, *Collisional Electron Detachment of H^-: A Complete Angular Distribution*, Phys. Rev. Lett. 40, 1642

[27] M.E. Rudd et al., *Electron production in proton collisions with atoms and molecules: energy distributions*, Rev. Mod. Phys. 64, 441 - 490 (1992)

[28] M.W. Gealy et al., *Energy and Angular Distributions of Electrons from Ion Impact on Atomic and Molecular Hydrogen. I. 20-114-keV $H^+ + H_2$*, M. Eugene Rudd Publications. 33. https://digitalcommons.unl.edu/physicsrudd/33

[29] D. Tskhakaya et al., *The Particle-In-Cell Method*, Contrib. Plasma Phys. 47, No. 8-9, 563 – 594 (2007) / DOI 10.1002/ctpp.200710072

[30] M. Barbisan et al., *First results from beam emission spectroscopy in SPIDER negative ion source*, M Barbisan et al 2021 Plasma Phys. Control. Fusion 63 125009

[31] B. Zaniol, *Error evaluation in the spectroscopic measurement of high power beam angular divergence*, Journal of Quantitative Spectroscopy & Radiative Transfer 112 (2011) 513–518